Tréhu, A.M., Bohrmann, G., Rack, F.R., Torres, M.E., et al., 2003
*Proceedings of the Ocean Drilling Program, Initial Reports* Volume 204

# 11. SITE 1252[1]

Shipboard Scientific Party[2]

## INTRODUCTION

Site 1252 (proposed Site HR5a) was drilled in ~1040 m of water ~4.5 km northeast of the southern summit of Hydrate Ridge. The site is located on the western flank of a secondary anticline that is located east of the crest of Hydrate Ridge. The sediments in the core of the anticline appear to be continuous with the accretionary complex sediments sampled near the base of Site 1244, ~1.5 km to the west. Although there is an anomalously bright bottom-simulating reflector (BSR) at a depth of ~170 meters below seafloor (mbsf) within the core of the anticline, the BSR disappears abruptly and does not extend beneath Site 1252 (see Fig. **F8,** p. 58, in the "Leg 204 Summary" chapter). Sediments onlapping the anticline from the west can be correlated with sediments sampled at Site 1251.

The principal objectives at Site 1252 were the following:

1. Sample the sediments in the core of the anticline to determine whether they are compositionally and biostratigraphically similar to those at the base of Site 1244.
2. Determine the structure of these sediments in order to constrain the mode of growth of the anticline/diapir.
3. Determine whether hydrates are present ~150 m from a strong BSR but where no BSR is present.
4. Provide age constraints on the geological history recorded by seismic stratigraphy.

This is the only site at which we did not acquire logging-while-drilling (LWD) data. One hole was drilled at Site 1252 (Fig. **F1**), comprising 28 cores to 260 mbsf.

**F1.** Bathymetric map, p. 22.

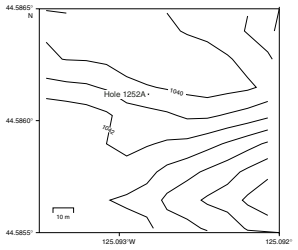


[1]Examples of how to reference the whole or part of this volume. [2]Shipboard Scientific Party addresses.

Ms 204IR-111

# OPERATIONS

Site 1252 is the only site for which no LWD data were obtained. Site 1252 was cored (Table T1) under good weather conditions. Wind speed was 13–11 kt, gusting to 22 kt; seas were 5–6 ft; swell was 7 ft; and the prevailing sea-surface current was from the north at ~0.5 kt.

Hole 1252A was spudded at 0325 hr on 31 August 2002 and cored with the advanced piston corer (APC) to refusal at 125 mbsf, with excellent recovery (Table T1). We continued with extended core barrel (XCB) coring to a total depth (TD) of 259.8 mbsf, where the primary scientific objectives were achieved. The only special downhole tool used at this site was the APC temperature (APCT) tool, which was used to measure in situ temperature in seven runs (Table T9). After coring, wireline logging data were acquired including one run with the triple combination (triple combo) tool string and one run with the Formation MicroScanner (FMS)-sonic tool string (see "Downhole Logging," p. 17). This alternate site was the last site drilled during Leg 204.

## Transit to Victoria, British Columbia, Canada

The rig was secured to get under way at 2100 hr on 1 September. All thrusters and hydrophones were retrieved and secured. The ship prepared to get under way and departed for Victoria at 2400 hr. We picked up the pilot at 0800 hr on 2 September and docked at Berth "B" north at 0900 hr, thus concluding Leg 204.

# LITHOSTRATIGRAPHY

Site 1252 is located on the eastern flank of Hydrate Ridge between Sites 1244 and 1251 (see Figs. F1, p. 51, and F8, p. 58, both in the "Leg 204 Summary" chapter). One hole (Hole 1252A) was drilled at Site 1252, reaching a maximum penetration of 259.8 mbsf. Recovery was very good (97.6%), which provided a nearly complete sedimentary sequence at Site 1252. On the basis of visual core description (VCD) and smear slides (e.g., variations in sedimentary structure and grain size or biogenic and lithologic components) and in correlation with the results from neighboring sites, three main lithostratigraphic units (Units I–III) were distinguished (Fig. F2).

We also compare and correlate our results with the three-dimensional (3-D) multichannel seismic reflection data (see Fig. F8, p. 58, in the "Leg 204 Summary" chapter), downhole wireline logging data (gamma ray, density, and resistivity), as well as physical property measurements (magnetic susceptibility [MS] and gamma ray attenuation [GRA] density) to better constrain the lithostratigraphic units (Fig. F3). Correlation of the lithostratigraphic units defined here with the other Leg 204 sites is summarized in Figure F10, p. 60, in the "Leg 204 Summary" chapter.

## Lithostratigraphic Units

### Lithostratigraphic Unit I

Interval: Core 204-1252A-1H through Section 11H-4
Depth: 0.00–96.40 mbsf
Age: mid-Pleistocene through Holocene

T1. Hole locations, p. 53.

F2. Lithostratigraphic summary, p. 23.

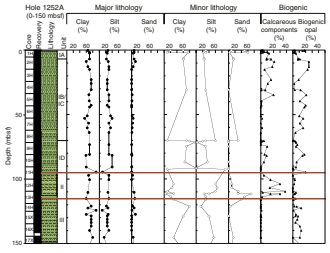


F3. Seismic reflection profile, p. 25.

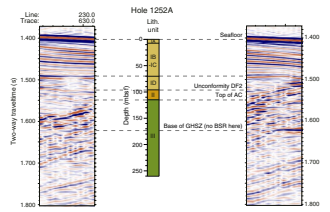

Lithostratigraphic Unit I consists of dark greenish gray (5GY 4/1) diatom-rich to diatom-bearing homogeneous silty clay, locally interbedded with silt to fine sand lenses and including a thick debris flow deposit toward the base of the lithostratigraphic unit (Fig. F2). The lower boundary of lithostratigraphic Unit I coincided with by a regional unconformity (Fig. F3), defined based on in the 3-D seismic reflection data from Site 1251 (see Fig. F8, p. 58, in the "Leg 204 Summary" chapter) and in the cores as an increase in grain size and calcareous biogenic components. Based on the changing abundance of biogenic components, grain size, and correlation with subunits defined at Site 1251, lithostratigraphic Unit I is divided into three subunits (Subunits IA–ID) above the aforementioned seismic unconformity. Lithostratigraphic Subunit IA correlates with lithostratigraphic Subunit IA at Site 1251, and lithostratigraphic Subunit IB-IC is coeval to Subunits IB and IC identified at Site 1251. Lithostratigraphic Subunit IB-IC cannot be distinguished as two separate units at Site 1252, possibly a result of variations in sediment distribution and accommodation to the preexisting topography at the time of deposition but is named in such a way as to be consistent with the unit names at Site 1251. Lithostratigraphic Subunit ID at Site 1252 encompasses a seismically defined debris flow deposit not drilled at Site 1251, which lies above the regional seismic unconformity (see details in "Environment of Deposition," p. 7) (Fig. F3) (see Fig. F8, p. 58, in the "Leg 204 Summary" chapter).

### *Lithostratigraphic Subunit IA*

Lithostratigraphic Subunit IA (Hole 1252A; 0–7 mbsf) consists of diatom- and nannofossil-rich silty clay, locally interbedded with fine to very fine foraminifer-bearing sands. The bases of the sand layers are sharp and the tops are gradational, suggestive of turbidite sequences. These layers are thin (2–4 mm thick), frequent (every 10 to 20 cm), and mostly concentrated in Sections 204-1252A-1H-1 and 1H-2.

Smear slide analyses indicate that the major lithology of lithostratigraphic Subunit IA is composed of sediment with ~70% clay, ~25% silt, and <1% sand (Fig. F2). Sulfides were not observed. The minor lithology is dominated by coarse grains, with an average distribution of 28% silt and 23% sand, locally reaching up to 60% at the top of the subunit (Section 204-1252A-1H-1). Bioturbation is common, especially at the base of minor lithologies. Biogenic content is high throughout the subunit, with an average composition of 7% calcareous components and 9% siliceous components (Fig. F4). Diatoms dominate the top of the lithostratigraphic subunit, reaching up to 15% (e.g., Samples 204-1252A-1H-1, 2 cm, and 1H-1, 22 cm).

Ten distinctive light greenish gray (5GB 7/1), thin (0.5–2 cm thick) clay layers are observed in Section 204-1252A-1H-2 (bases at 33, 37, 44, 49, 61, 67, 81, 82, 94, and 105 cm) at ~2 mbsf (Fig. F5). These layers appear to correlate with similar intervals at Site 1251 that may represent the Holocene–upper Pleistocene transition. The placement of the boundary between lithostratigraphic Subunits IA and IB-IC was based on the last occurrence of sand layers in Section 204-1252A-2H-2 (7 mbsf).

### *Lithostratigraphic Subunit IB-IC*

Lithostratigraphic Subunit IB-IC (Hole 1252A; 7–69.5 mbsf) consists of homogeneous diatom-bearing to diatom-rich silty clay. Iron sulfides, observed as black to dark gray (N3) color precipitates, nodules, and mottles, are common throughout this lithostratigraphic subunit, partic-

F4. Clay, silt, sand, and calcareous and biogenic components, p. 26.

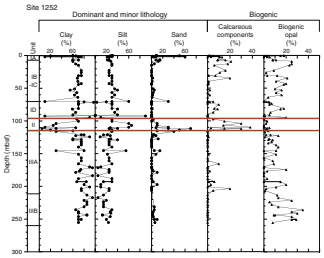


F5. Holocene/Pleistocene boundary, p. 27.

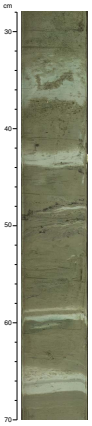

ularly in Cores 204-1252A-4H, 5H, and 7H, and correlate with three peaks recorded in the MS data at ~26, 45, and 58 mbsf (see **"Magnetic Susceptibility,"** p. 15, in "Physical Properties"). Bioturbation is also abundant, often highlighted by the presence of iron sulfides. The lower boundary of this lithostratigraphic subunit is marked by the onset of a debris flow deposit located at 69.5 mbsf (DF2 on Fig. **F3**) and characterized by both a transparent facies in the 3-D seismic profiles (see Fig. **F8,** p. 58, in the "Leg 204 Summary" chapter) and by a large peak in the MS data (see **"Magnetic Susceptibility,"** p. 15, in "Physical Properties").

Smear slide analyses indicate that the major lithology of lithostratigraphic Subunit IB-IC is typically composed of 69% clay, 30% silt, and 1% sand (Fig. **F2**). The major mineral components of the subunit are feldspar, quartz, and clay and opaque minerals. Biogenic components, particularly biogenic opal (mostly diatoms and sponge spicules) are abundant in this subunit, composing 12% of the sediment on average and reaching 25% locally (Samples 204-1252A-2H-3, 96 cm, and 2H-6, 42 cm). Calcareous components, mostly nannofossils, are abundant (up to 12%) in the upper part of this lithostratigraphic subunit (7–34 mbsf) and decrease drastically to <1% from 34 to 71.5 mbsf (Figs. **F2, F4**).

### *Lithostratigraphic Subunit ID*

Lithostratigraphic Subunit ID (Hole 1252A; 69.5–96.5 mbsf) is characterized seismically as a distinct wedge of incoherent reflectors (see Fig. **F8,** p. 58, in the "Leg 204 Summary" chapter) common in sediment lacking bedding (e.g., large debris flow deposits). In the cores, soft-sediment deformation features, convoluted bedding, and clay clasts, which we interpret as evidence of such a debris flow deposit, are found between 69.5 and 71.5 mbsf (see Sections 204-1252A-8H-6 to 8H-CC). Mud clasts, ranging from 1 to 3 cm in diameter, are embedded in a clay-rich convoluted matrix (Fig. **F6**). Below the prominent soft-sediment deformation features and convoluted bedding, lithostratigraphic Subunit ID is composed of a homogeneous sequence of diatom-rich to diatom-bearing silty clay, typically dark greenish gray (5GY 4/1) to very dark gray (5GY 4/1) where sulfide precipitates are present. The lower boundary of this subunit is marked by the regional seismic unconformity and corresponds to an abrupt change in sedimentation rate (see **"Summary,"** p. 10, in "Biostratigraphy").

The clay-size fraction of the major lithology of lithostratigraphic Subunit ID composes, on average, 70% of the sedimentary components. Silt-size grains compose the remaining 30% of the major lithology, with sand-size grains entirely absent from the lithostratigraphic subunit (Fig. **F2**). Quartz is the dominant mineral identified in smear slide analyses, ranging from 10% to 20% of the mineral constituents, with feldspar, opaque minerals, and glauconite composing ~1%–5% of the remaining coarse fraction. The minor lithologies analyzed in smear slides rarely differ greatly from the major lithology, except in Sample 204-1252A-11H-1, 128 cm, taken from an authigenic carbonate-rich cement surrounding the only carbonate nodule in lithostratigraphic Unit I.

Lithostratigraphic Subunit ID is rich in biogenic components. Smear slide analyses of both the major and minor lithologies indicate that calcareous components (calcareous nannofossils and foraminifers) typically compose 3%–7% of the sedimentary components (Fig. **F2**). Siliceous microfossils (diatoms, radiolarians, and siliceous sponge spicules) compose 8%, on average, of the major and minor sedimentary components, with the average siliceous microfossil content of the major lithology ~11%.

**F6.** Debris flow deposit, p. 28.

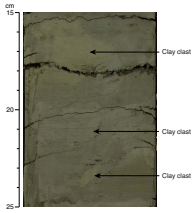

Bioturbation and sulfide precipitates are abundant in lithostratigraphic Subunit ID. Cores 204-1252A-10H and 12H are particularly rich in sulfide. The high sulfide precipitate content of the lithostratigraphic subunit corresponds to a 25-m-thick high in the MS data (see "Magnetic Susceptibility," p. 15, in "Physical Properties"). Correlation between MS highs and sulfide precipitates was seen at several sites during Leg 204, and at this site the best correlation occurred in the zone containing pyrrhotite nodules in Section 204-1252B-10H-CC of lithostratigraphic Subunit ID.

## Lithostratigraphic Unit II

Interval: Core 204-1252A-9H through Section 13H-3.
Depth: 96.40–113.90 mbsf.
Age: early to mid-Pleistocene

The boundary between lithostratigraphic Units I and II is defined by the regional unconformity observed in the 3-D seismic data (Fig. F3), also seen at Site 1251 below Subunit IC (see Fig. F8, p. 58, in the "Leg 204 Summary" chapter). Lithostratigraphic Unit II is primarily composed of foraminifer-rich silty clay that is dark greenish gray (5GY 4/1). This silty clay is interlayered with lighter-colored layers of fine sand and coarse silt, especially at the base of the lithostratigraphic unit. The major sedimentary components of lithostratigraphic Unit II are clay minerals, quartz, and feldspar. The biogenic components consist of mainly calcareous microfossils (foraminifers and calcareous nannofossils) with some siliceous microfossils (sponge spicules, silicoflagellates, and diatoms) (Fig. F4).

High-frequency fining-upward turbidites, the bases of which contain fine to very fine sand that grades to silt and clay, characterize lithostratigraphic Unit II (Figs. F2, F4) and differentiate it from lithostratigraphic Unit I. The sand and silt layers that form the sharp erosional bases of the turbidite sequences are commonly ~1 cm thick, although occasionally they reach 3 cm thick (Fig. F7B). These layers typically contain macroscopic foraminifers (e.g., Cores 204-1252A-11H and 12H) and grade upward into sulfide-rich, bioturbated, homogeneous silty clay and clay (Fig. F7A).

The mineralogy of the major lithology of lithostratigraphic Unit II is similar to that of lithostratigraphic Subunit ID. Quartz is, again, the dominant mineral constituent, composing 10%, on average, of the coarse fraction. Silt- and sand-size grains compose 28% and 5%, respectively, of the sedimentary components, with the remainder composed of clay-size minerals. The primary textural difference between lithostratigraphic Units I and II occurs in the minor lithology. Sand composes as much as 70% of the mineral components in the minor lithologies near the base of lithostratigraphic Unit II (e.g., Sample 204-1252A-13H-2, 67 cm) and typically composes 30% of the minor lithology throughout the rest of the unit (Fig. F2).

Lithostratigraphic Unit II is composed of as much as 18% biogenic components, and Sample 204-1252A-12H-7, 86 cm, contains 38% calcareous components (35% foraminifers and 3% calcareous nannofossils). This sample contains the highest percentage of calcareous microfossils in lithostratigraphic Unit II. However, lithostratigraphic Unit II lacks significant siliceous microfossils. Smear slides indicate <3% of the sediment is composed of siliceous microfossils (Fig. F2).

F7. Sulfide precipitates and graded turbidite, p. 29.

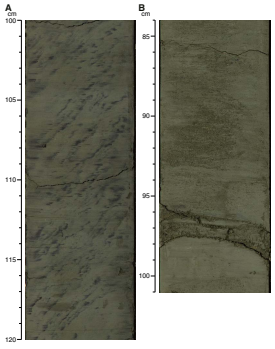

## Lithostratigraphic Unit III

Interval: Section 204-1252A-13H-4 through Core 28H.
Depth: 113.9–259.8 mbsf.
Age: late Pliocene–early Pleistocene

The boundary between lithostratigraphic Units II and III is present at 114 mbsf, where a 5-m-thick series of glauconite-rich sand layers is interbedded with silty clay hemipelagic sediment (Figs. **F8, F9**). This depth corresponds to the depth of the western limb of anticline B on the 3-D seismic data (see Fig. **F8,** p. 58, in the "Leg 204 Summary" chapter) as well as to prominent changes in the well logging and physical property characteristics of the section (see **"Downhole Logging,"** p. 17, and **"Physical Properties,"** p. 14). Lithostratigraphic Unit III is distinguished from lithostratigraphic Unit II by its general lack of sulfide precipitates, bioturbation, and silt layers, as well as its higher state of lithification. Additionally, lithostratigraphic Unit III contains abundant carbonate precipitates in the form of both cements and nodules (Fig. **F10**), mousselike textured sediments (Fig. **F11**) above the base of the gas hydrate stability zone (GHSZ), and debris flow deposits at 125.5 and 197 mbsf. Clay and silty clay composed of <10% biogenic components make up the major lithology of lithostratigraphic Unit III, and the minor lithologies lack the silt and sand turbidites typical of lithostratigraphic Unit II (Fig. **F2**).

Lithostratigraphic Unit III is a sequence of silty clay horizons punctuated at irregular and infrequent intervals by graded sandy silt turbidites. The major lithology of the lithostratigraphic unit comprises 73% clay-, 24% silt-, and 3% sand-size grains. The minor lithologies range in composition from clay, composed of 5% silt and 95% clay, to sand-silt-clay, composed of 40% sand, 30% silt, and 30% clay (Fig. **F2**). Quartz, feldspar, and opaque minerals compose the majority of the minerals in the major lithology, and carbonate is abundant in the minor lithologies. Cores 204-1252A-14H, 19X, and 21X each contain multiple carbonate-cemented layers, identified in the cores by their lighter color (Fig. **F10**) and visible as carbonate precipitates. The precipitates tend to be clustered between 121 and 127 mbsf in Core 204-1252A-14H, just below the glauconite sand layers that define the upper boundary of the lithostratigraphic unit, and deeper in Unit III (between 179 and 192 mbsf). Smear slide analyses of the carbonate cements surrounding the authigenic carbonates between 121 and 127 mbsf indicate that these cements contain similar amounts of authigenic carbonate, typically 60% to 80%, to those cements sampled between 179 and 192 mbsf. Silt composes as much as 30% of the sediments in these cements, although it is typically only 10%–15% of the sample.

The biogenic content of lithostratigraphic Unit III lies in stark contrast to the overlying lithostratigraphic Unit II. Below the glauconite sand layers at 114 mbsf, the calcareous microfossil content of the sediment drops to 0%, though it increases slightly below this depth (Fig. **F2**). Foraminifers are found in trace amounts (1%–2%) in Samples 204-1252A-19X-2, 26 cm; 20X-3, 9 cm; and 21X-1, 22 cm, but are otherwise absent from lithostratigraphic Unit III. Calcareous nannofossils can compose as much as 20% of the major lithology of lithostratigraphic Unit III (Sample 240-1252A-23X-2, 60 cm), although typically, they are absent. The biogenic opal content of lithostratigraphic Unit III is similar to that of the overlying lithostratigraphic units at the top, but increases (up to 35%) with depth (Fig. **F4**).

**F8.** Glauconite distribution, p. 30.

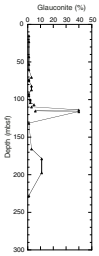


**F9.** Glauconite sand layer, p. 31.

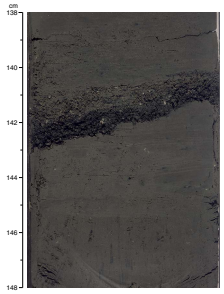


**F10.** Authigenic carbonate precipitates, p. 32.

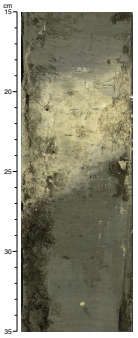


**F11.** Mousselike texture, p. 33.

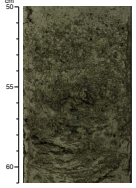

The two most striking features of lithostratigraphic Unit III are the glauconite sand layers (Figs. F8, F9) and the carbonate precipitates immediately below (Fig. F10). Two debris flow deposits are also present within the lithostratigraphic unit but show no major deviations from the dominant lithology in smear slide analyses. Unfortunately, total organic carbon (TOC) and X-ray diffraction analyses to determine the composition of the carbonate samples were not done on board the ship but will be conducted postcruise. However, as a result of the high density of these samples (~2.0 g/cm$^3$) (see "Physical Properties," p. 14), the carbonate precipitates are likely composed of dolomite.

The clay content of the major lithology in lithostratigraphic Unit III slightly increases below 211 mbsf, in conjunction with the increase in biogenic opal content (Fig. F2). Clay composes 78% of the major lithology, silt composes 20%, and sand 3%, on average (Fig. F2). Two glauconite-bearing sands are visible in lithostratigraphic Unit III at 232 and 234 mbsf in Core 204-1252A-26X. The sampled minor lithologies were similar to the major lithology in grain size and mineral composition, although their biogenic components differed from those of the major lithologies (Fig. F2). Calcareous microfossils are entirely absent from smear slide samples taken near the base of lithostratigraphic Unit III (211–259 mbsf). Biogenic opal content, on the other hand, increases in this interval relative to the overlying sediments of lithostratigraphic Unit II. Scaly fabric, caused by the alignment of clay minerals under an oriented stress, was also observed in lithostratigraphic Unit III. However, the orientation of the fabric could not be determined because the core likely rotated within the liner during recovery.

## Sedimentary Evidence of Gas Hydrate

Lithostratigraphic Unit III lies within the sediments of the deeper accretionary complex (sediments known to contain gas hydrate at Ocean Drilling Program Site 892; see Fig. F1, p. 51, in the "Leg 204 Summary" chapter) and contains abundant disrupted sedimentary textures indicative of the dissociation of gas hydrate (particularly in Cores 204-1252A-14H through 18X and 20X) (Fig. F11). These soupy and mousselike textures were encountered between 126 and 179 mbsf at Site 1252; however, the only samples presumed to contain gas hydrate, as identified by cold anomalies with the infrared (IR) camera (see "Infrared Scanner," p. 14, in "Physical Properties"), were taken from ~83 and ~99 mbsf. Initial attempts to correlate the disrupted sedimentary features with the IR images and well logging data were unsuccessful at sea, but additional postcruise examination may reveal some relationships. Additionally, chloride samples were taken from one soupy layer and will be analyzed postcruise. Thus, there is textural sedimentological evidence for the dissociation of gas hydrate in the cores described at Site 1252; however, there is insufficient supporting evidence, at this time, for the presence of gas hydrate in these cores to definitively rule out core-related disturbance as the cause of the disrupted sedimentary fabric.

## Environment of Deposition

Site 1252 is located on the eastern flank of southern Hydrate Ridge between Sites 1244 and 1251. The stratigraphy at this site is best correlated to that at Site 1251 by direct comparison between the recovered sedimentary section and the stratigraphic geometries observed in the 3-

D seismic reflection data (see Figs. F8, p. 58, and F10, p. 60, both in the "Leg 204 Summary" chapter).

Seismic reflection data across Site 1252 indicate that the deeper accretionary complex sediments of lithostratigraphic Unit III are folded and that the sediments of lithostratigraphic Unit II were deposited against the western limb of fold at this site. The contact between lithostratigraphic Units III and II is truncated in the seismic data and, thus, represents a buttress unconformity at ~114 mbsf. Just below the unconformity at Site 1252, the uppermost portion of lithostratigraphic Unit III is composed of clay and silty clay with very few calcareous components. However, above the unconformity, calcareous components and foraminifer-bearing silty turbidites are present and there is an abundance of glauconite from ~114 to 120 mbsf (Fig. F8). Abundant glauconite, which was also detected on the well logging density and gamma data (see "Downhole Logging," p. 17), is present within the silty clay and clay of Unit III. These fine-grained sediments are suggestive of a lower sedimentation rate and perhaps a lower-energy environment conducive to glauconite formation (Leeder, 1999). Below the glauconite-rich zone, there is a zone of abundant authigenic carbonate. Perhaps the unconformity serves as a regional conduit for fluids and, thus, promotes carbonate precipitation.

Lithostratigraphic Unit II, as defined at Site 1252, is correlated with Lithostratigraphic Unit II at Site 1251, although the lithostratigraphic unit is much thinner at Site 1252 than Site 1251. The apparent buttress unconformity that separates the two lithostratigraphic units at Site 1252 is not present on the eastern limb of Anticline B, drilled at Site 1251, although regional mapping in the 3-D seismic data suggests the sediments of Unit II at Sites 1251 and 1252 may have been deposited at the same time (see Fig. F8, p. 58, in the "Leg 204 Summary" chapter).

A regional unconformity is observed at both Sites 1252 and 1251 above Unit II and provides a good tie point for intersite correlation (horizon labeled "U" on Fig. F8, p. 58, in the "Leg 204 Summary" chapter). This unconformity separates lithostratigraphic Unit II from lithostratigraphic Subunit ID at Site 1252 and separates lithostratigraphic Unit II from lithostratigraphic Subunit IC at Site 1251.

Site 1244 lies upslope from Site 1252, and because of stratigraphic pinchouts, only the uppermost stratigraphy correlates between Sites 1244, 1252, and 1251 (see Figs. F5, p. 55, and F10, p. 60, both in the "Leg 204 Summary" chapter). We recovered cores from the eastern slope basin sedimentary section, which contains at least two large and seismically distinct submarine landslides or debris flows (DF1 and DF2) within lithostratigraphic Unit I at both Sites 1252 and 1251 (see Fig. F8, p. 58, in the "Leg 204 Summary" chapter). Because of the good correlation with the younger regional unconformity discussed above, it is possible to correlate all of the stratigraphy of Unit I at Sites 1252 and 1251. The older of the two debris flows (DF2) is present only at Site 1252 (see Fig. F8, p. 58, in the "Leg 204 Summary" chapter), where it is identified as lithostratigraphic Subunit ID.

Lithostratigraphic Subunit ID at Site 1252 is interpreted as a submarine landslide or debris flow deposited on the unconformity surface that serves as the upper boundary for lithostratigraphic Unit II (at both Sites 1251 and 1252). Although lithologic evidence for the landslide only appears as a 2-m-thick zone of clasts inferred as a debris flow capping an ~10-m-thick zone of calcareous- and siliceous-rich clays and silty clays, the seismic signature is distinct, forming a wedge-shaped lens with chaotic reflectivity. This wedge of sedimentation can be

traced regionally on the 3-D seismic data, except in the immediate area of Site 1251, where Subunit IC is deposited directly on the unconformity surface. Continuation of the landslide (see DF2 on Fig. **F8,** p. 58, in the "Leg 204 Summary" chapter) on the unconformity surface east of Site 1251 can be identified in the deeper part of the eastern slope basin, however, suggesting that its absence at Site 1251 resulted from either sediment bypass or erosion associated with emplacement.

The uppermost lithostratigraphic unit preserved at both Sites 1252 and 1251 is lithostratigraphic Subunit IA. Although the youngest Holocene record is preserved at Site 1251, it is absent at Site 1252. The uppermost stratigraphy recovered at Site 1252, however, does contain bands of gray clay (Fig. **F5**) and turbidites, which were also observed at Site 1251. A color change similar to this is regionally identified throughout the central Cascadia margin and typically signifies the transition from Pleistocene to Holocene sedimentation (see **"Environment of Deposition,"** p. 9, in "Lithostratigraphy" in the "Site 1251" chapter).

# BIOSTRATIGRAPHY

Only one hole was drilled at Site 1252. Hole 1252A contains a 259-m-thick upper Pliocene–Quaternary sedimentary sequence. Biostratigraphy determined for Site 1252 was based on examination of all core catcher samples from Hole 1252A.

## Diatoms

Diatoms are few to common in Hole 1252A, except for one sample (Sample 204-1252A-13H-CC [116.65 mbsf]) where diatoms are absent. Preservation of diatoms is generally poor, except in the interval between Samples 1252A-25X-CC and 28X-CC, where diatoms are moderately to well preserved. Diatom assemblages from sediments in Hole 1252A are dominated by species such as *Stephanopyxis* spp., *Neodenticula* spp., and *Thalassionema nitzschioides*. A few warm-water taxa, such as *Hemidiscus cuneiformis, Fragilariopsis doliolus,* and *Thalassiosira oestrupii,* are frequently present.

The interval from the seafloor down to 81.28 mbsf contains *Neodenticula seminae* but lacks *Proboscia curvirostris;* this interval was assigned to North Pacific Diatom Zone (NPD) 12 (*N. seminae* Zone). The LO of *P. curvirostris* was found in Sample 204-1252A-10H-CC (90.8 mbsf), and the next event, the LO of *Actinocyclus oculatus,* was found in Sample 14H-CC (128.72 mbsf). Therefore, the interval between these two levels (90.8–128.72 mbsf) was assigned to the Zone NPD 11 (*P. curvirostris* Zone). The interval between Samples 204-1252A-14H-CC and 27X-CC (128.72–249.34 mbsf) contains *A. oculatus* but lacks *Neodenticula koizumii* and was assigned to the Zone NPD 10 (*A. oculatus* Zone). The FO of *P. curvirostris* was placed in Sample 204-1252A-19X-CC (173.39 mbsf). Sample 204-1252A-28X-CC (258.96 mbsf) contains *N. koizumii* and *N. seminae* but lacks *Neodenticula kamtschatica,* and thus, the level of 258.96 mbsf was determined as the LO of *N. koizumii* and assigned to the upper part of the Zone NPD 9 (*N. koizumii* zone). This indicates an age of ~ 2.0 Ma for the bottom sediments from Hole 1252A.

## Calcareous Nannofossils

Calcareous nannofossils from Hole 1252A were investigated in smear slides from core catcher samples. About 40% of these samples contain rare to common, moderately preserved calcareous nannofossils; these samples are located predominantly in the upper part of the sequence in Hole 1252A, from the seafloor to 116 mbsf. Samples below 116 mbsf do not contain calcareous nannofossils or else yield trace, poorly preserved nannofossils, except for three samples (Samples 204-1252A-17X-CC, 20X-CC, and 23X-CC) that contain rare nannofossils. Dissolution of calcareous nannofossils was observed in sediments at Site 1252, whereby the edge of a coccolith shield was partly dissolved or the major part of the shield was lost by dissolution. Such dissolution of calcareous nannofossils was not observed in sediments at sites located nearby, such as at Sites 1244 and 1251 or at other Leg 204 sites. Therefore, we ruled out the possibility that carbonate dissolution occurred below the calcite compensation depth in this region. The observed dissolution of calcareous nannofossils in the sediments at Site 1252, on the other hand, probably implies the influence of fluid affecting the sediments at this site. However, this assumption needs further study postcruise and comparison with the results from geochemistry studies of pore water samples from this site.

The calcareous nannofossil biostratigraphy determined for Site 1252 during the last phase of the cruise was based on the nannofossil record deduced from the 40% of samples that were relatively good.

A Quaternary calcareous nannofossil assemblage was discovered in the sequence from Hole 1252A. *Emiliania huxleyi* is frequently present from the seafloor down to 71.42 mbsf, assigning this interval to Zone NN21. Abundant *E. huxleyi* was observed in the upper part of Zone NN21, the interval from seafloor to 14.88 mbsf, allowing us to assign the top part of the interval to the *E. huxleyi* Acme Zone. The interval of 81.28–90.80 mbsf lacks *E. huxleyi* and *Pseudoemiliania lacunosa;* this interval was assigned to Zone NN20. The next event, the LO of *P. lacunosa* found in Sample 204-1252A-11H-CC (100.59 mbsf), marks the NN19b/NN20 zonal boundary. Below 116.65 mbsf, samples are barren of calcareous nannofossils poorly preserved in the majority of samples examined and very few small *Gephyrocapsa* species are present infrequently in a few of these samples. Consequently, the mid-Pleistocene small *Gephyrocapsa* spp. Acme Zone (1.0–1.2 Ma) was not determined for Site 1251. Three samples (Samples 204-1252A-17X-CC, 20X-CC, and 23X-CC) in the interval from 153.41 to 179.54 mbsf contain rare, moderately preserved calcareous nannofossils. Rare *Calcidiscus macintyrei* is present in three of these relatively good samples; the LO of *C. macintyrei* (1.59 Ma; the lower part of the Zone NN19) was placed at 153.41 mbsf. Rare *Gephyrocapsa lumina* is also present in these three samples, suggesting an age younger than 1.67 Ma (younger than the FO of *G. lumina*) for sediments at 179.54 mbsf. Samples below 179.54 mbsf (Samples 204-1252A-20X-CC through 28X-CC) do not contain any calcareous nannofossils. As a result, no calcareous nannofossil data were obtained from the lowest part of the sequence in Hole 1252A.

## Summary

Nine microfossil events (four diatom and five nannofossil events) were recognized for Site 1252 (Table T2). An age-depth plot shows that

T2. Bioevents found, p. 54.

biohorizons from the two fossil groups agree well with each other (Fig. F12).

The lack of more detailed events, especially nannofossil events from the lowest part of the sequence from Hole 1252A, makes it impossible to accurately determine the Pleistocene/Pliocene boundary for Site 1252. However, this boundary could be roughly placed between 179.54 and 258.96 mbsf, based on an estimated nannofossil age younger than 1.67 Ma at 179.54 mbsf and a diatom-based estimate of ~2 Ma at 258.96 mbsf (Table T2).

Linear sedimentation rates at Site 1252 have been estimated based on biostratigraphic data (Table T2). The sedimentation rates are estimated to be 28 cm/k.y. for the interval from the top of Hole 1252A to 90 mbsf, 9 cm/k.y. for the interval from 90 to 150 mbsf, 70 cm/k.y. for the interval from 150 to 210 mbsf, and 14 cm/k.y. for the interval from 210 mbsf to the bottom of Hole 1252A (Fig. F12). According to seismic data, an unconformity is located at ~120 mbsf at Site 1252. Considering this unconformity, an alternative sedimentation rate of 6 cm/k.y. is estimated for the interval from 95 to 130 mbsf (Fig. F12), extrapolating the sedimentation rate above and below the unconformity.

F12. Age-depth plot, p. 34.

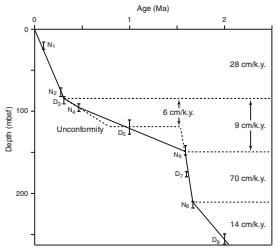


## INTERSTITIAL WATER GEOCHEMISTRY

Only one hole was cored at Site 1252, from which we recovered 54 interstitial water (IW) samples. The main objective of the IW program at this site was to provide geochemical proxies that may aid in defining the nature of the accretionary complex sediments, which have been uplifted at this location to a depth of ~120 mbsf (see "Introduction," p. 1). In addition, pore water chemistry will be used to provide constraints on biogeochemical processes within the upper sediments and the possibility of gas hydrate presence within the gas hydrate stability zone (GHSZ). IW samples were collected at a resolution of one sample per section in the upper 14 mbsf, to provide adequate sampling within the anaerobic methane oxidation (AMO) zone. In the interval from 14 to 180 mbsf, we collected IW samples at a frequency of approximately two whole-round samples per core, followed by a sampling resolution of one whole-round sample per core to the bottom of the borehole. As a result of time constraints, no shipboard measurement of dissolved cation concentrations was performed at this site, but samples were collected for postcruise analyses. The IW geochemistry data are tabulated in Table T3 and are illustrated in Figure F13.

T3. Dissolved species in pore waters, p. 55.

F13. Various dissolved species, p. 35.

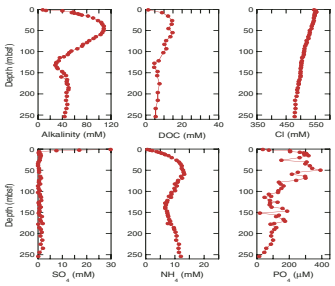


### Chloride Concentration and the Presence of Gas Hydrate

The distribution of dissolved chloride at Site 1252 displays a linear decrease with depth at a rate of ~0.48 mM/m to ~120 mbsf (Fig. F14). Similarly, a decrease in chloride of ~0.46 mM/m was observed at Site 1251, and it is thought to reflect diffusion of chloride ions from present-day seawater values to the low-chloride fluids that characterize the accreted sediments at these sites (see "Interstitial Water Geochemistry," p. 13., in the "Site 1251" chapter). At Site 1244, dissolved chloride also shows a linear decrease from ~70 mbsf to the bottom of the hole, where the chloride concentration is 472 mM (see "Interstitial Water Geochemistry," p. 13, in the "Site 1244" chapter). Consistently, the onset of low-chloride fluids at Sites 1244, 1251, and 1252 all coin-

F14. Chloride concentrations, p. 36.

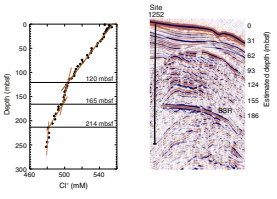

cide with a seismic reflector that is thought to image the top of the accreted sedimentary wedge, which occurs at ~120 mbsf at Site 1252 (see "Introduction," p. 1). Similar pore fluid freshening was observed at other sites on the Cascadia margin and elsewhere and is attributed to clay dehydration deep within the accretionary prism (e.g., Kastner et al., 1995).

In contrast to other sites drilled during this leg, at Site 1252 there are no significant excursions to low chloride values throughout much of the GHSZ. The lack of chloride anomalies does not necessarily mean that no gas hydrate is present. Rather, it indicates that if gas hydrate is present it must be as discrete and narrow intervals, which are not captured with the sampling resolution of two samples per core (i.e., a sample approximately every 4.5 m). This is consistent with the IR temperature data, which show temperature anomalies significantly lower than those measured at other sites, and these anomalies are restricted to very thin intervals (see "Physical Properties," p. 14). Furthermore, whereas at Site 1251 there may be a significant accumulation of gas hydrate at the base of the GHSZ (see "Interstitial Water Geochemistry," p. 13, in the "Site 1251" chapter), such a gas hydrate–bearing interval was not observed at Site 1252.

### Sulfate, Methane, and the Sulfate/Methane Interface

Three data points define the sulfate gradient within the sulfate reduction zone, where the profile is linear (Fig. F15). The sulfate/methane interface (SMI) is located at ~5 mbsf, defined by both sulfate and methane data. Interstitial sulfate first reaches minimum concentrations between data points at 3.85 and 6.25 mbsf, and methane concentrations, as documented by headspace gas data, rise quickly between 4.00 and 6.40 mbsf (see "Hydrocarbon Gases," p. 13, in "Organic Geochemistry").

Following the method of Borowski et al. (1996) outlined at Site 1244 (see "Interstitial Water Geochemistry," p. 13, in the "Site 1244" chapter), the estimated methane flux at Site 1252 is $5.7 \times 10^3$ mM/cm$^2$/yr, based on a sulfate gradient of 9.1 mM/m (equivalent to a slope of 0.11 m/mM) (see Fig. F15), a sulfate diffusion coefficient of $5.8 \times 10^{-6}$ cm$^2$/s at 5°C, and average porosity of 0.70%. For comparison, the estimated methane flux is equivalent to that of Site 1251, about twice that calculated for Site 1244, and about three times larger than that estimated at the Blake Ridge, a large passive-margin gas hydrate terrain (Borowski et al., 1996). These estimates assume methane delivery through diffusion only and assume that the linear portion of the sulfate curve is mainly created by sulfate demand at the SMI. If significant water or methane advection occurs or if sulfate depletion through AMO is of minor importance, then this estimate is invalid.

F15. Sulfate and methane concentrations, p. 37.

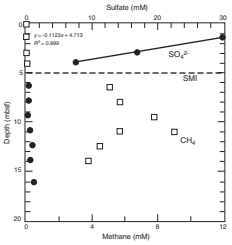


## ORGANIC GEOCHEMISTRY

Site 1252 is located on the flank of an anticline in the basin east of Hydrate Ridge. The objectives at this site are to sample the accretionary complex at shallow depth and to learn when the anticline formed. Site 1252 is located near a prominent BSR. The shipboard organic geochemistry program at Site 1252 included only the analyses of hydrocarbon gases. A description of the methods used for the gas analyses is summa-

rized in **"Organic Geochemistry,"** p. 16, in the "Explanatory Notes" chapter.

## Hydrocarbon Gases

The levels of methane ($C_1$), ethane ($C_2$), ethylene ($C_{2=}$), and propane ($C_3$) remaining in the cores were measured using the headspace technique. The results are reported in Table **T4** and plotted as parts per million by volume (ppmv) of gas component vs. depth in Figure **F16.** Methane content increases rapidly from levels of 2–261 ppmv in the shallowest samples at 0–4 mbsf, to ~10,165 ppmv at a depth of 6.4 mbsf, and then to levels of ~20,000–50,000 ppmv at greater depths. This sharp increase in headspace methane occurs at the approximate depth of the SMI, as seen previously at Sites 1244, 1245, 1247, 1251, and elsewhere. The vial headspace ppmv $C_1$ concentration was recalculated to express the millimolar methane concentrations remaining in the cores. These estimates of absolute gas concentration are meaningful only in shallow zones where sediments are undersaturated or slightly supersaturated at surface conditions with respect to dissolved methane. The calculated dissolved $CH_4$ concentration is shown in Figure **F17,** along with the sulfate depletion profile (see **"Sulfate, Methane, and the Sulfate/Methane Interface,"** p. 12, in "Interstitial Water Geochemistry"). The general pattern of methane increase and sulfate decrease is consistent with an SMI depth of ~5 mbsf.

Ethane content of headspace gas is maintained at low levels (<10 ppmv) in core samples from Site 1252 from the seafloor to ~200 mbsf. Only at the base of the cored sequence from 225 to 254 mbsf do ethane contents increase to values ranging from 24- to 36-ppmv levels. Propane is present in a few samples at 1–3 ppmv. Ethylene and propylene ($C_{3=}$) are also sporadically present in traces (0.6–3.3 ppmv) throughout the depth interval cored (Table **T4;** Fig. **F16**).

The compositions of gas samples collected from voids or expansion gaps in the core liner are listed in Table **T5** and plotted on Figure **F18.** The void gas (vacutainer) samples are relatively pure methane, generally with minor air contamination. The ethane content of void gas shows regular increase with depth at Site 1252, despite the unexplained high ethane content in the sample from a depth of 16.28 mbsf. Propane is present in only a few samples and shows no variation in concentration with depth. Other heavier hydrocarbons ($C_4$–$C_6$) are absent.

Gas composition expressed as the $C_1/C_2$ ratio of headspace and void gas is plotted vs. depth in Figure **F19.** The $C_1/C_2$ ratios for both headspace and void gas show systematic decrease with increasing depth and temperature. There are some slight offsets in the $C_1/C_2$ ratio resulting from an increase in ethane content in sediments, especially in the depth interval from ~100 to 130 mbsf. Similar deviations from the general trend were observed at other sites (Sites 1244, 1245, and 1247), where gas hydrate recovery or other evidence for the presence of hydrate was noted. However, there is no shift to lower $C_1/C_2$ ratios at the approximate depth of the base of the methane hydrate stability zone (170 mbsf), unlike what was observed at Site 1251. Although a prominent BSR is present east of Site 1252, there is no strong evidence for the presence of gas hydrate in the headspace or void gas compositions, nor did we observe a BSR directly beneath Site 1252.



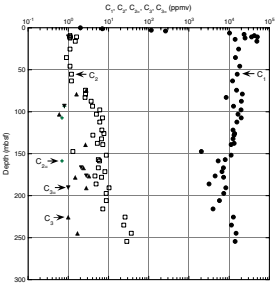



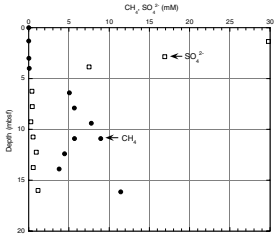



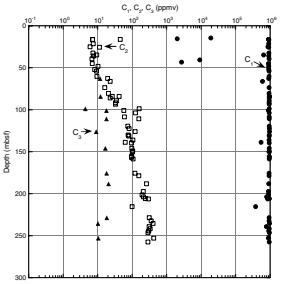



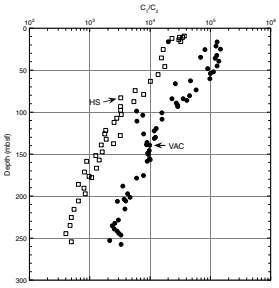

### Other Analyses

Additional analyses of sediments will be done as part of shore-based research, along with the stable isotopic characterization of the gases.

## PHYSICAL PROPERTIES

At Site 1252, one hole was drilled and used for complete physical property analyses. Because of pervasive gas expansion, no compressional (*P*)-wave velocity ($V_P$) and shear strength measurements were conducted. The physical properties (especially bulk density) measured at Site 1252 typically match the lithostratigraphic units.

IR imaging was carried out on all cores recovered prior to and after sectioning and curating. This site has very good core recovery and allowed detailed imaging of the entire sediment column. Only two samples thought to contain gas hydrate were recovered at Site 1252.

### Infrared Scanner

IR imaging was used to identify the location of hydrate in cores on the catwalk. The track-mounted IR camera was used twice, both prior to and after sectioning the core liner. The second scan could be directly correlated postcruise to the VCDs, particularly the presence of mousse-like texture that is indicative of the location of hydrate.

Data from the first IR scan were used to generate a downhole temperature profile at Hole 1252A (Fig. **F20A**). The temperatures in the upper 130 mbsf show an overall linear trend of increasing temperature with depth common to many APC cored holes. The gradient is much less than in situ temperature gradients and apparently reflects a combination of increasing in situ temperature, cooling of the cores during retrieval, and gas expansions or exsolution.

Definite negative $\Delta T$ anomalies first appear at a depth of 43 mbsf (Fig. **F21;** Table **T6**) and continue to a depth of 133 mbsf. A single cold anomaly is present at 183 mbsf. Given that this anomaly is present by itself and near a core top, it was probably caused either by drilling fluid incursion during core retrieval or gas expansion/gas exsolution. The depth of the base of GHSZ at Site 1252 is estimated to be at ~170 mbsf, derived by projecting a prominent BSR westward a few hundred meters to the hole location. The lowest definite thermal anomalies are present at 133 mbsf, indicating that negative $\Delta T$s are present within the stability zone for gas hydrate. The lack of thermal anomalies between 133 and 170 mbsf suggests that while pressure-temperature conditions are appropriate for gas hydrate stability in this zone, the chemical composition is not (e.g., lack of methane or water to create sufficient hydrate to cause a thermal anomaly in core samples).

The downcore temperature pattern for Cores 204-1252A-13H and 14H (Fig. **F20B**) suggests a significant lithologic or gas content change at the bottom of Core 13H and top of Core 14H (118.9 mbsf). At that point, the downcore temperature becomes more irregular as a result of an increase in the number of voids greater than ~2 cm in width. At this depth, the accretionary complex sediments were first encountered, overlain by glauconite sand layers (see **"Lithostratigraphy,"** p. 2). Core 204-1252A-13H exploded on the catwalk just after IR scanning was completed. Both cores contain small amounts of hydrate based on anomaly frequency, thickness, and $\Delta T$ magnitude. The difference be-

**F20.** Downcore temperature profiles, p. 42.

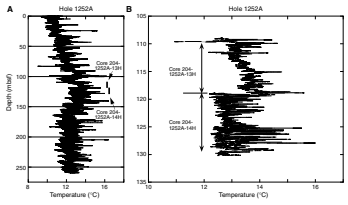


**F21.** IR temperature anomalies, p. 43,

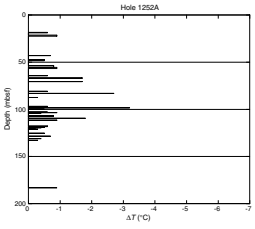


**T6.** Gas hydrate, p. 58.

tween the exploding core (Core 204-1252A-13H) and the highly fractured core (Core 14H) is probably a reflection of their respective mechanical properties. Core 204-1252A-14H coincides with the presence of indurated carbonate nodules and layers that may be more brittle than other parts of the core (e.g., Core 13H). Further analysis of the wireline logs and acoustic logs is expected to provide additional insight into the gas content and mechanical properties of this part of the hole (see "Downhole Logging," p. 17).

## Sediment Density from Multisensor Track and Moisture and Density

Sediment density shows a different downhole trend compared to that observed at other Leg 204 Sites (Fig. F22; Table T7). The density profile shows several distinct breaks where density drops sharply to lower values. These breaks correspond in part to the boundaries of the lithostratigraphic units (see "Lithostratigraphy," p. 2) and can be correlated to seismic data (Fig. F23). Five breaks were identified, located at 7, 28, 115, 180, and 210 mbsf, respectively. Each of these breaks is associated with large variations in the MS (see next section), with one exception at 180 mbsf.

The GRA density shows higher densities at the seafloor, with density values around 1.6 g/cm³ for the upper 8 m. Values drop below this depth to ~1.5 g/cm³, then increase with depth to ~28 mbsf, where a second decrease in density occurs. This second break in the density profile is less pronounced and accounts for a decrease in density of ~0.05 g/cm³. The interval between 28 and 115 mbsf is characterized by a normal density increase with depth. Density values are ~1.75 g/cm³ at 115 mbsf and decrease to 1.5 g/cm³ over an interval of 25 m before they start to increase again to a depth of 180 mbsf. Between 180 and 220 mbsf, density increases again, then remains at around 1.65 g/cm³ for the remaining depth range.

Porosity decreases relatively uniformly from values of ~70% at the seafloor to 55% at the boundary between lithostratigraphic Units II and III (114 mbsf). The top of lithostratigraphic Subunit III is characterized by very low densities and high porosities as well as slightly lower than average grain densities.

At a depth of 183 mbsf, several carbonate layers are present (see "Lithostratigraphy," p. 2). Samples taken from one of these layers (Samples 204-1252A-21X-1, 47–49 cm; 21X-1, 52–54 cm; and 21X-1, 64–66 cm) show high bulk densities of >1.8 g/cm³, with a maximum of 2.17 g/cm³ in the center of the carbonate layer.

## Magnetic Susceptibility

The MS profile is marked by several distinct intervals of high values (see Fig. F22). Most of these intervals of elevated values correspond to breaks in the density profile as described above, with the boundary defined at the top of the interval that shows high MS values (not the peak itself). This is particularly evident for the top of lithostratigraphic Units II and III at 71.5 and 114 mbsf, respectively. There is no clear change in MS values associated with the boundary between lithostratigraphic Subunits IA and IB.

F22. Physical properties, p. 44.

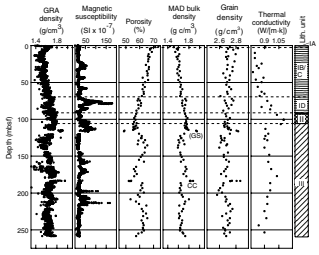


T7. MAD, p. 59.

F23. Physical properties with 3-D seismic data, p. 45.

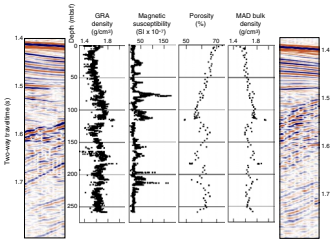

### Compressional Wave Velocity from Multisensor Track and Hamilton Frame

As a result of pervasive gas expansion, no $V_P$ was measured either using the MST or the Hamilton Frame.

### Thermal Conductivity

Thermal conductivity was measured regularly on the whole-round cores (see "Physical Properties," p. 22, in the "Explanatory Notes" chapter). The values vary between 0.78 and 1.1 W/(m·K), with an average value of 0.915 W/(m·K) (Table T8). The measurements are affected by the pervasive gas-expansion cracks, but the locations for individual measurements were chosen to minimize distortion. There is significant scatter in the data, but thermal conductivity values follow the same downhole trend as the bulk density, indicating that thermal conductivity is correlated with moisture content of the sediments (see "Physical Properties," p. 19, in the "Site 1251" chapter).

T8. Thermal conductivity, p. 60.

### Shear Strength

As a result of pervasive gas expansion, no shear strength measurements were made.

### Summary and Discussion

Physical properties measured at Site 1252 correlate well with lithostratigraphic boundaries and the results from wireline logging. The GRA density and MS profiles provide the strongest basis for the correlation. Moisture and density (MAD) properties are biased by low sampling frequency and thus provide only general trends. The distinctive sedimentological feature at Site 1252 is the abundance of carbonate layers, either as solid concretions or as disseminated layers. These carbonate layers show high bulk density, low porosity, and high grain density values.

Site 1252 has very low hydrate abundance overall based on IR imaging and the low abundance of mousselike texture as defined from VCDs. Several cold-spot anomalies were observed but make up a relatively small volume of the core and never exceed a $\Delta T$ of –3°C.

## DOWNHOLE TOOLS AND PRESSURE CORING

### Downhole Temperature Measurements

One mudline measurement plus six runs within the sediments to determine in situ temperatures were made in Hole 1252A using the APCT tool (Table T9; Fig. F24). Data were modeled using the software program TFIT (as described in "Downhole Tools and Pressure Coring," p. 34, in the "Explanatory Notes"), using measured thermal conductivities (see "Physical Properties," p. 14). Uncertainty in the extrapolated value of in situ temperature resulting from a subjective analyst picking of $t_p$, $t_i$, and $t_f$ is <0.02°C for these high-quality records. Uncertainty resulting from possible errors in measured values of thermal conductivity is also estimated to be ~0.02°C. Additional uncertainty results from un-

T9. Temperature measurements, p. 61.

F24. APCT tool temperature-time series, p. 46.

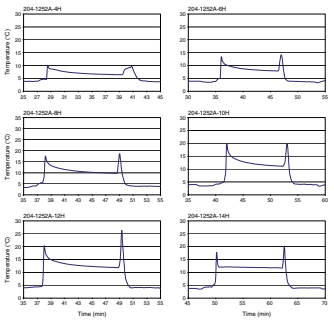

certainty in instrument calibration (see "Downhole Tools and Pressure Coring," p. 29, in the "Site 1244" chapter).

The resulting temperature estimates are shown in Figure F25. The slope and the seafloor intercept are relatively insensitive to whether or not the mudline temperature is included; both equations predict BSR depths to be within 5 m of the projected depth of the BSR, which is well within the uncertainty. However, if one considers that APCT 11 was used for all of these measurements and that the ice bath calibration of APCT 11 suggests that +0.513°C should be added to temperatures recorded by this instrument (see "Downhole Tools and Pressure Coring," p. 14, in the "Site 1246" chapter), then this is the only site drilled during Leg 204 where the measured in situ temperatures are higher than those predicted for the pure methane stability/seawater stability boundary. Whether this observation is significant has yet to be determined.

F25. Estimated temperature as a function of depth, p. 47

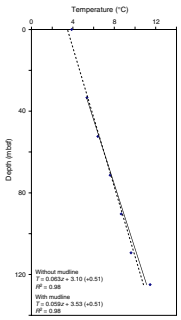


## In Situ Pressure Measurements

No in situ pressure measurements were made at this site.

## Pressure Core Sampler

No pressure core sampler cores were taken at this site.

## HYACINTH Pressure Core Sampling

No HYACINTH pressure cores were taken at this site.

# DOWNHOLE LOGGING

## Wireline Logs

### Operations

In the Leg 204 *Scientific Prospectus,* Hole 1252A was designated as an alternate site (proposed site Site HR5a), which was selected to examine the nature of the accretionary complex in the area of Hydrate Ridge. With only 4 days remaining until the end of Leg 204, Hole 1252A was spudded at 1130 hr Universal Time Coordinated on 30 August 2002 at a water depth of 1051.0 meters below rig floor (mbrf). Hole 1252A was APC and XCB cored to a depth of 259.8 mbsf (drillers depth). Rig-up for conventional wireline logging (CWL) operations began at 1150 hr on 31 August, and final rig down for the CWL operations was completed by 0030 hr on 1 September. See Table T10 for detailed information on the Hole 1252A CWL program.

T10. CWL operations summary, p. 62.

CWL operations in Hole 1252A began with the deployment of the triple combination (triple combo) tool string (Temperature/Acceleration/Pressure [TAP] tool/Dual Induction Tool [DIT]/Hostile Environment Litho-Density Tool [HLDT]/Accelerator Porosity Sonde [APS]/Hostile Environment Gamma Ray Sonde [HNGS]/Inline Checkshot Tool [QSST]) (Table T10). The triple combo tool string initially reached the TD of the hole at 262 mbsf, which is 2.2 m deeper than the drillers determined TD for the hole. Excellent quality data were acquired during the main uphole pass (see below), and the tool was run back into the hole for a second logging pass. The second upward pass of the triple

combo tool string started at a depth of 184 mbsf, and excellent quality data were recorded on the second ascent. The TAP temperature data and associated depth data were recorded without problems during both lowerings of the triple combo tool string. The triple combo logging run ended with the rig-down of the tool string being completed at 1810 hr on 31 August.

For the second CWL run in Hole 1252A, the FMS-sonic (FMS/Dipole Sonic Imager [DSI]/Scintillation Gamma Ray Tool [SGT]) tool string was deployed. The FMS-sonic string reached a maximum depth of 262 mbsf on two consecutive passes. The two FMS-sonic runs confirmed the excellent condition of the hole. The FMS images and sonic waveforms recorded from the two passes were of very high quality. During the first pass, the DSI tool was set at a low-frequency mode for the lower dipole, standard frequency for the upper dipole, and low frequency for the monopole. During the second pass, the monopole and the upper dipole were set at their standard frequencies, and the lower dipole was set at a low frequency. The recorded sonic waveforms from both lowerings of the DSI are of very high quality, particularly the dipole recordings, but the very low velocity of this formation made it difficult for the automatic slowness/time coherence (STC) picking program to pick accurate $V_P$. Some adjustment of the STC parameters allowed for improved *P*-wave picks, but further reprocessing is required. The quality of the recorded shear wave data was very high, but it will also require additional processing.

## Logging Quality

All logging data in Hole 1252A are of very high quality (Figs. **F26, F27, F28**). The hole conditions were extremely good, with hole diameters seldom exceeding 12.5 in. Comparison of logs from successive passes shows good repeatability of the data. The two passes of the FMS calipers also showed that the hole was nearly cylindrical, consistent with the HLDT log caliper recorded on the triple combo runs. The anomalous data from the top of each log (70–78 mbsf) in Figures **F26** and **F27** were obtained through the drill pipe, which was set at a depth of 75 mbsf during the CWL logging program.

The absolute depths, relative to seafloor, for all of the CWL logs were fixed by identifying the gamma ray signal associated with the seafloor and depth shifting the logging data appropriately. The gamma ray pick for the seafloor in Hole 1252A was 1051 mbrf for all of the CWL runs.

## Interpretation of Wireline Logging

Seismic data reveal a relatively complex geologic setting for this site (see Figs. **F5,** p. 55, **F8,** p. 58, in the "Leg 204 Summary" chapter). Analysis of log data from Hole 1252A shows that the contact between the folded accretionary complex and overlying sedimentary section is marked by an ~7-m-thick zone at ~114–121 mbsf that is characterized by anomalous gamma ray, density, and resistivity log values. Our initial interpretation is that this anomalous zone contains a mixture of mostly glauconite and possibly authigenic carbonate, which was probably deposited on top of the underlying accretionary complex as the anticline was developing. The integration of available core data and downhole logs also reveals the presence of at least one significant carbonate horizon near the crest of the anticline.

**F26.** Summary of CWL data, p. 48.

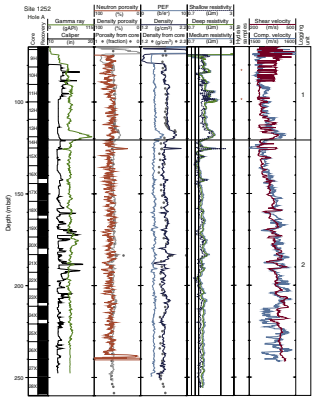

**F27.** CWL gamma ray logging data, p. 49.

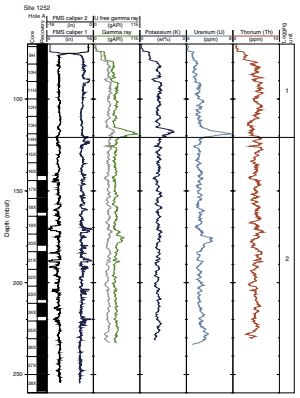

**F28.** CWL acoustic logging data, p. 50.

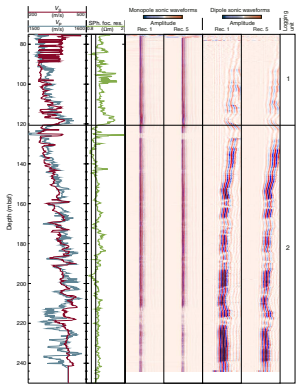

## Logging Units

The logged section in Hole 1252A is divided into two "logging units" on the basis of obvious changes in the CWL gamma ray, bulk density, electrical resistivity, and acoustic transit-time measurements (Figs. F26, F27, F28). For comparison to other sites cored during Leg 204, the specific logging units defined in Hole 1252A are unique to this site. However, as described below, the boundary between logging Units 1 and 2 marks the contact between the sediments of the accretionary complex and relatively undeformed overlying sediments. This same boundary at other sites has been identified as the contact between logging Units 3 and 4.

Logging Unit 1 (75–121 mbsf) (base of pipe was set at 75 mbsf) is characterized by variable gamma ray, density, and resistivity log values. The most distinct interval is an ~7-m-thick zone (114–121 mbsf) near the base of logging Unit 1, in which the gamma ray log exceeds 110 American Petroleum Institute gamma ray units (gAPI), the density log measurements average ~1.9 g/cm³, and the deep reading resistivity log exceeds 1.6 Ωm. Further analysis of the spectral gamma ray logging data from Hole 1252A (Fig. F27) shows that this anomalous gamma ray zone also contains relatively high concentrations of uranium and potassium. The high gamma ray (potassium) and density of this anomalous section suggest the presence of glauconite, which was confirmed by the shipboard sedimentologists (see "Lithostratigraphy," p. 2). Based on the comparison of the available CWL data from Hole 1252 with the regional seismic data (see "Introduction," p. 1), it appears that this glauconite-rich section was deposited on an unconformity marking the top of the accretionary complex. We have placed the boundary between logging Units 1 and 2 at the base of the anomalous gamma ray interval at 121 mbsf. Logging Unit 1 also contains several conspicuous high-resistivity intervals from 94 to 100 mbsf that may contain gas hydrate.

Logging Unit 2 (121–260 mbsf; TD of Hole 1252A), reflecting the upper portion of the deformed sediments of the accretionary complex, is characterized by almost constant gamma ray, neutron porosity, density, and resistivity log measurements with depth, which are not consistent with a normal compaction profile. Caliper logs (Figs. F26, F27) from Hole 1252A also show that, in comparison, logging Unit 2 exhibits more irregular borehole diameters, with the appearance of more numerous, relatively large washouts. Near the top of logging Unit 2 there is a relatively thin 1-m-thick interval (125–126 mbsf) characterized by distinct high resistivities (>2.0 Ωm), high densities (>2.0 g/cm³), low neutron porosities (<30%), and low gamma ray values (<40 gAPI). This anomalous log interval appears to correlate with a distinct carbonate unit at 125 mbsf (see "Lithostratigraphy," p. 2). The base of the GHSZ at Site 1252, as interpreted from the regional seismic data, is at a depth of ~170 mbsf.

## Formation MicroScanner Images

FMS tools produce high-resolution images of the electrical resistivity characteristics of the borehole wall that can be used for detailed sedimentological and structural interpretations. In Figure F29, we show an FMS image from near the boundary between logging Units 1 and 2 in Hole 1255A. This FMS image includes both the anomalously high gamma ray zone in logging Unit 1 (114–121 mbsf) and the apparent carbonate unit from near

F29. FMS image showing glauconite and carbonate horizons, p. 51.

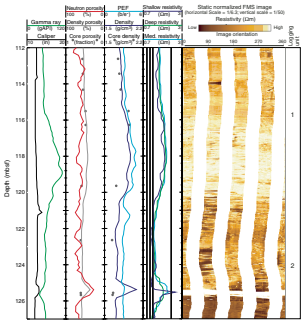

the top of logging Unit 2 (125–126 mbsf). The anomalously high gamma ray zone in logging Unit 1 appears to contain distinct nodules and layers of resistive material, probably glauconite with some carbonate, which would contribute to the high-density logging measurements within this interval. The carbonate near the top of logging Unit 2 appears as a single bright resistive layer with irregular upper and lower contacts.

## Logging Porosities

Sediment porosities can be determined from analyses of recovered cores and from numerous borehole measurements (see "Physical Properties," p. 22, and "Downhole Logging," p. 43, both in the "Explanatory Notes" chapter). Formation density and neutron data from the HLDT and the APS were used to assess the sediment porosities for Hole 1252A. Core-derived physical property data were used to both calibrate and evaluate the log-derived sediment porosities from Site 1252 (see "Physical Properties," p. 14).

The HLDT density log data (Fig. F26) reveal several prominent high-density intervals within Hole 1252A, which yield relatively low density and neutron log-derived sediment porosities. The density log-derived porosities in Hole 1252A range from ~60% to ~70%, whereas neutron log porosities range from an average value at the top of the logged section of ~70% to ~65% in logging Unit 2. Comparison of core- and log-derived porosities in Figure F26 reveals that the density log-derived porosities are generally similar to the core porosities. However, the neutron porosities are generally higher than the core-derived porosities throughout most of the hole.

## Gas Hydrate

IR anomalies were observed in Hole 1252A at 82.75 and 98.60 mbsf, and samples were preserved as possible gas hydrate specimens. At the depth of these two samples, the downhole resistivity logs are characterized by distinct stepwise increases in both electrical resistivities and acoustic velocities. At all of the other Leg 204 core sites on Hydrate Ridge, we have used the LWD resistivity log data to quantify the amount of gas hydrate. We have also shown that the vertical resolution of the LWD and CWL resistivity logs differs greatly. The complete analysis and comparison of the LWD and CWL resistivity-derived gas hydrate concentrations on Hydrate Ridge, including gas hydrate quantification at Site 1252, will be completed postcruise.

## Temperature Data

The TAP tool was deployed on the triple combo tool string in Hole 1252A (Fig. F30). During the process of coring and drilling, cold seawater is circulated in the hole, cooling the formation surrounding the borehole. Once drilling ceases, the temperature of the fluids in the borehole gradually rebounds to the in situ equilibrium formation temperatures. Thus, the temperature data from the TAP tool cannot be easily used to assess the nature of the in situ equilibrium temperatures. However, the plot of the first pass downgoing temperature profile in Figure F30 reveals several gradient changes that were caused by borehole temperature anomalies. The temperature anomaly at ~90 mbsf is the base of the drill pipe during the initial descent of the triple combo tool string. The break in the slope of the first pass downgoing temperature log at a depth ~170 mbsf is near the depth of the BSR near this site.

F30. TAP tool temperatures, p. 52.

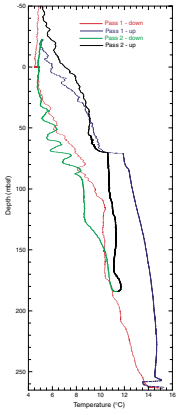

# REFERENCES

Borowski, W.S., Paull, C.K., and Ussler, W., III, 1996. Marine pore-water sulfate profiles indicate in situ methane flux from underlying gas hydrate. *Geology,* 24:655–658.

Clague, D., Maher, N., and Paull, C.K., 2001. High-resolution multibeam survey of Hydrate Ridge, offshore Oregon. *In* Paull, C.K., and Dillon, W.P. (Eds.), *Natural Gas Hydrates: Occurrence, Distribution, and Detection.* Am. Geophys. Union, Geophys. Monogr. Ser., 124:297–306.

Kastner, M., Kvenvolden, K.A., Whiticar, M.J., Camerlenghi, A., and Lorenson, T.D., 1995. Relation between pore fluid chemistry and gas hydrates associated with bottom-simulating reflectors at the Cascadia margin, Sites 889 and 892. *In* Carson, B., Westbrook, G.K., Musgrave, R.J., and Suess, E. (Eds.), *Proc. ODP, Sci. Results,* 146 (Pt 1): College Station, TX (Ocean Drilling Program), 175–187.

Leeder, M.R., 1999. *Sedimentology and Sedimentary Basins: from Turbulence to Tectonics:* Oxford (Blackwell Science).

**Figure F1.** Bathymetric map showing locations of holes drilled at Site 1252. Bathymetry from EM300 data acquired by Monterey Bay Aquarium Research Institute (MBARI) (Clague et al., 2001).

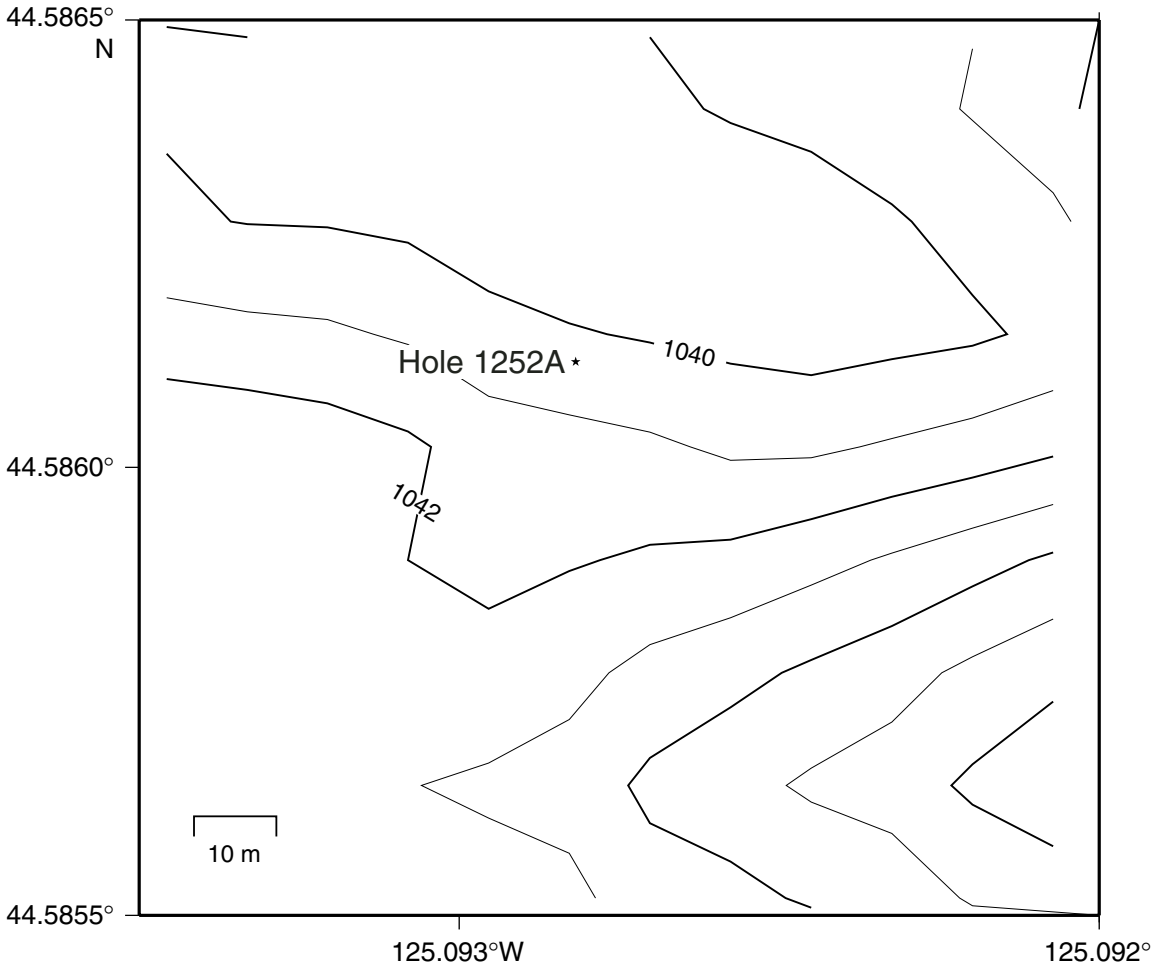

**Figure F2.** Lithostratigraphic summary for Site 1252. (Continued on next page.)

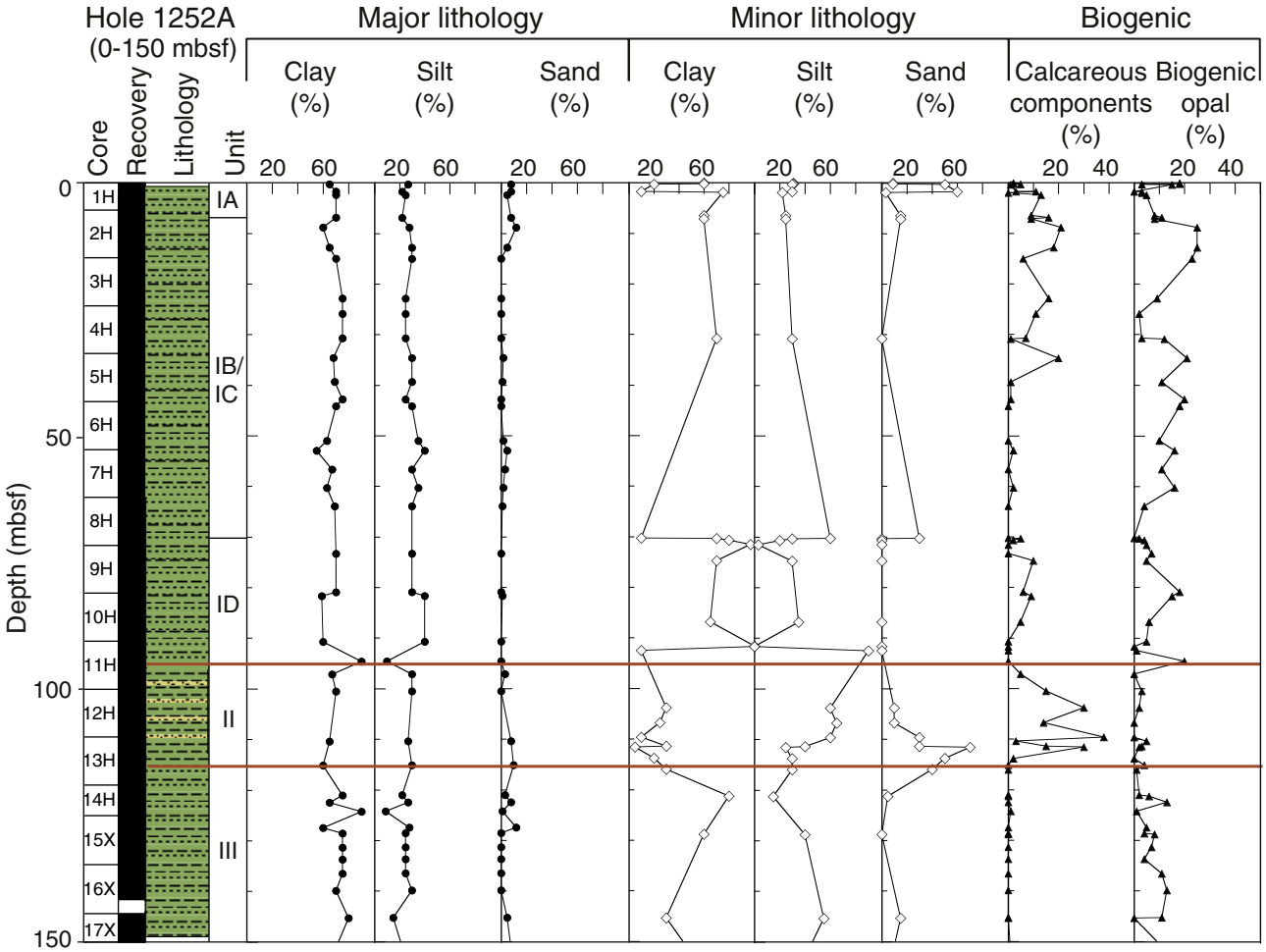

**Figure F2 (continued).**

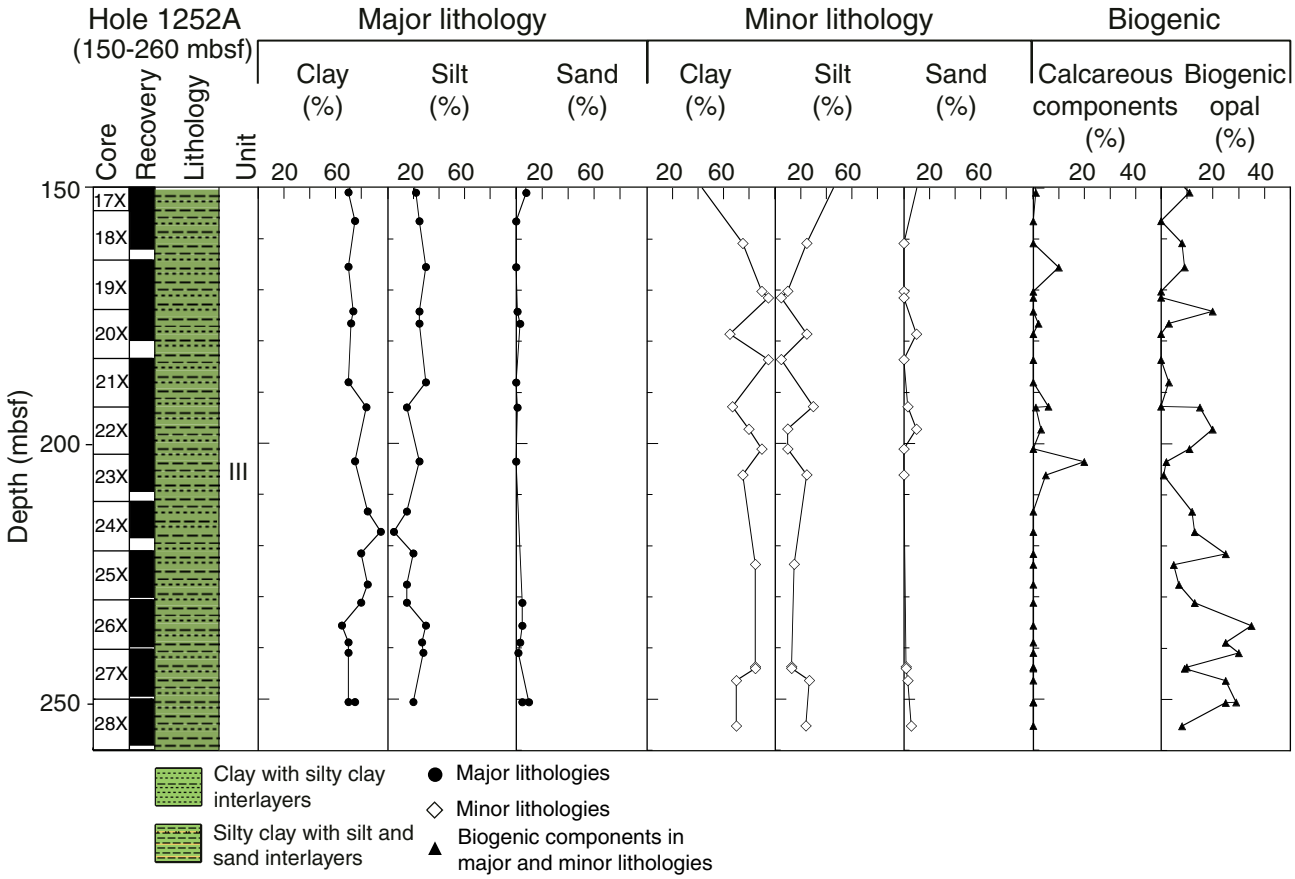

**Figure F3.** Seismic reflection profile from west (left) to east (right) across Site 1252. Lithostratigraphic Units and Subunits are shown as well as the location of Site 1252. GHSZ = gas hydrate stability zone, BSR = bottom simulating reflector, DF2 = debris flow 2 (see Fig. **F8,** p. 58, in the "Leg 204 Summary" chapter).

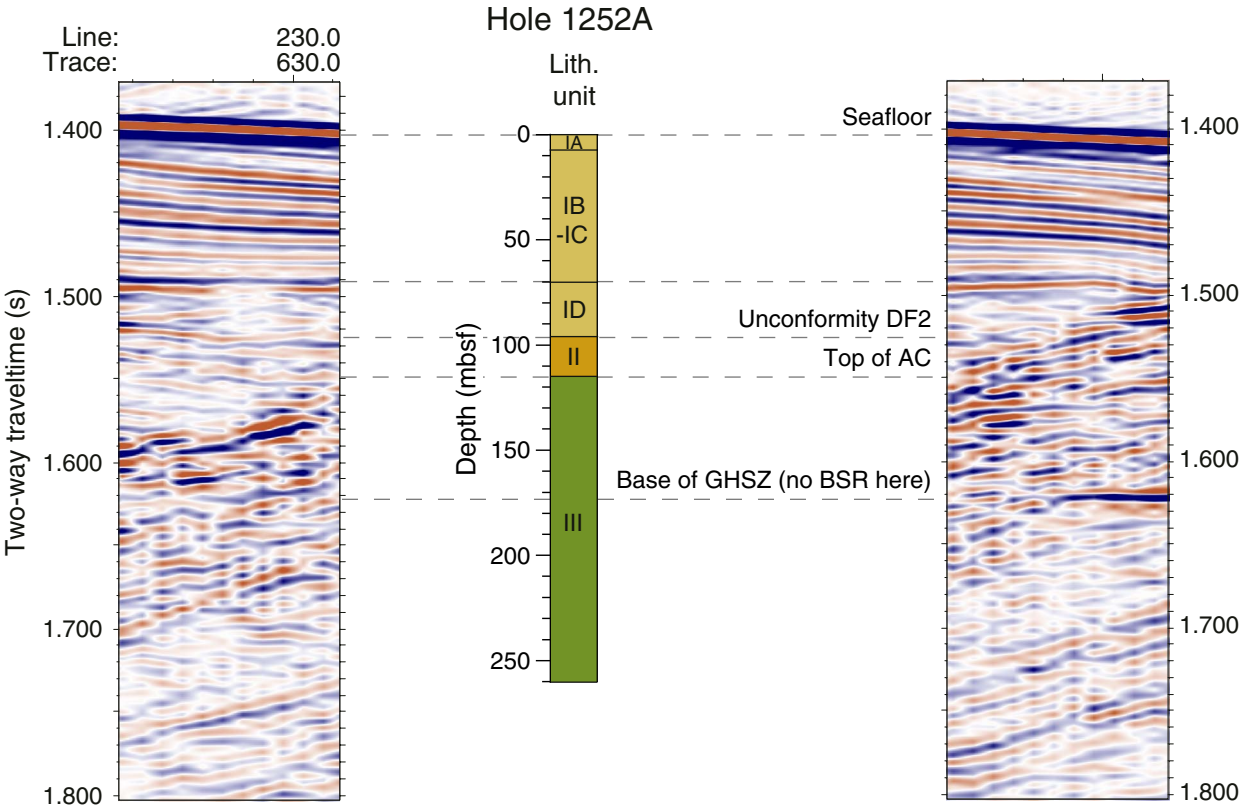

**Figure F4.** Abundance of clay, silt, sand, calcareous components, and biogenic opal in Hole 1252A (major and minor lithologies) based on smear slide descriptions.

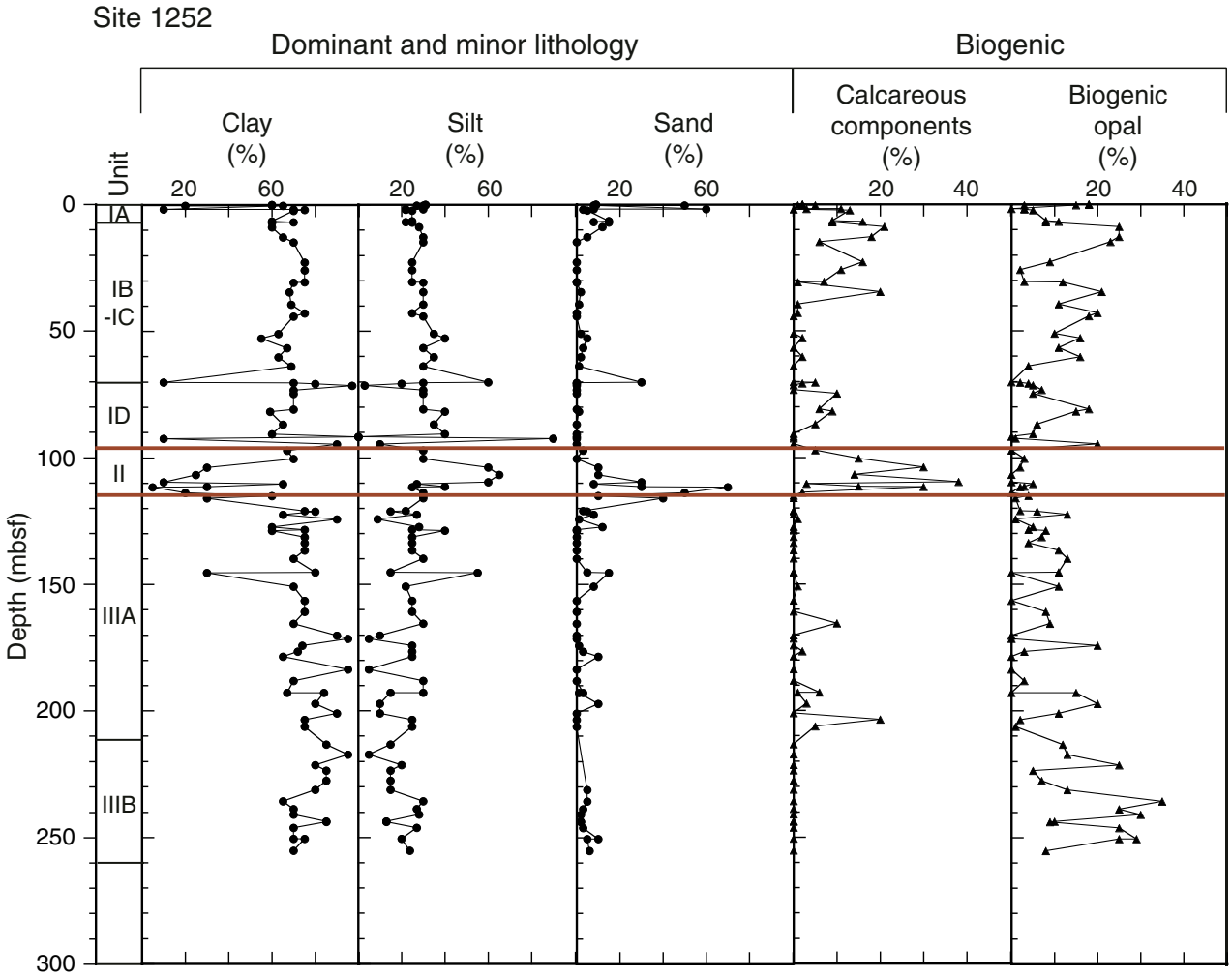

**Figure F5.** Close-up photograph of light gray clay layers, perhaps representing the Holocene/Pleistocene boundary in lithostratigraphic Subunit IA (interval 204-1252A-1H-2, 28–70 cm).

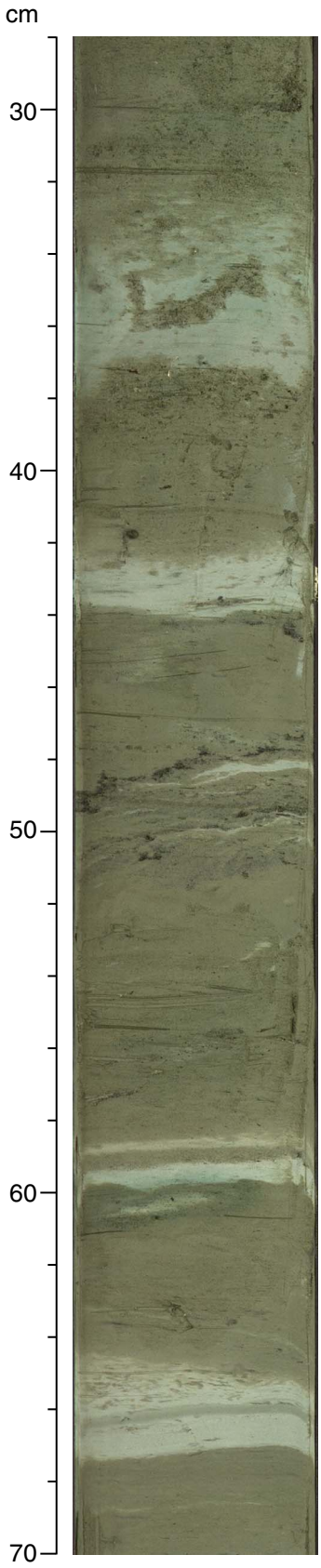

**Figure F6.** Close-up photograph of the clasts within the debris flow deposit in lithostratigraphic Subunit ID (interval 204-1252A-8H-7, 15–25 cm).

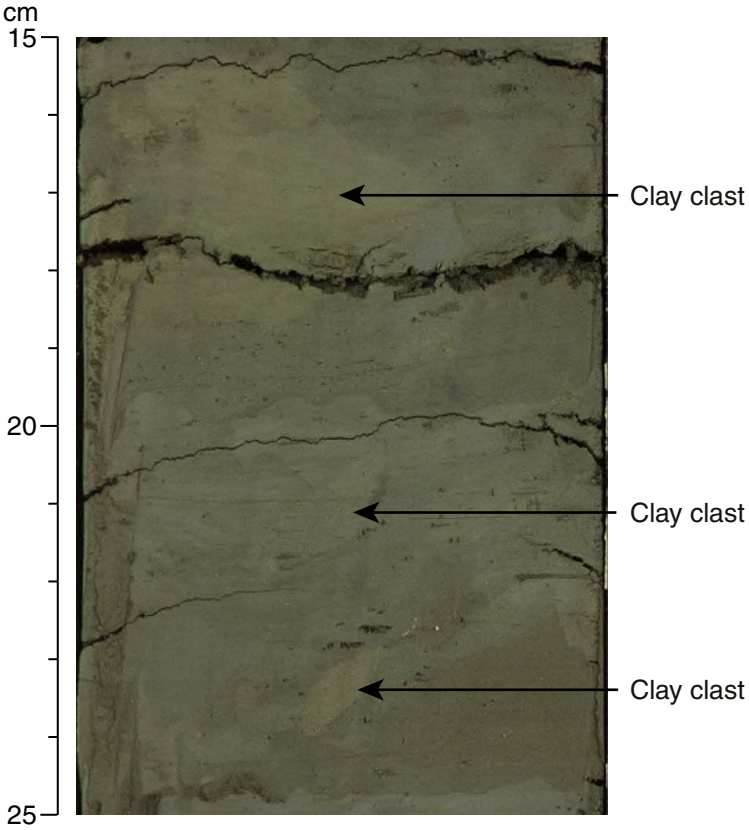

**Figure F7. A.** Close-up photograph of abundant sulfide precipitates in the silty clay of lithostratigraphic Unit II (interval 204-1252A-12H-4, 100–120 cm). **B.** Graded turbidite from lithostratigraphic Unit II (interval 204-1252A-12H-5, 84–101 cm).

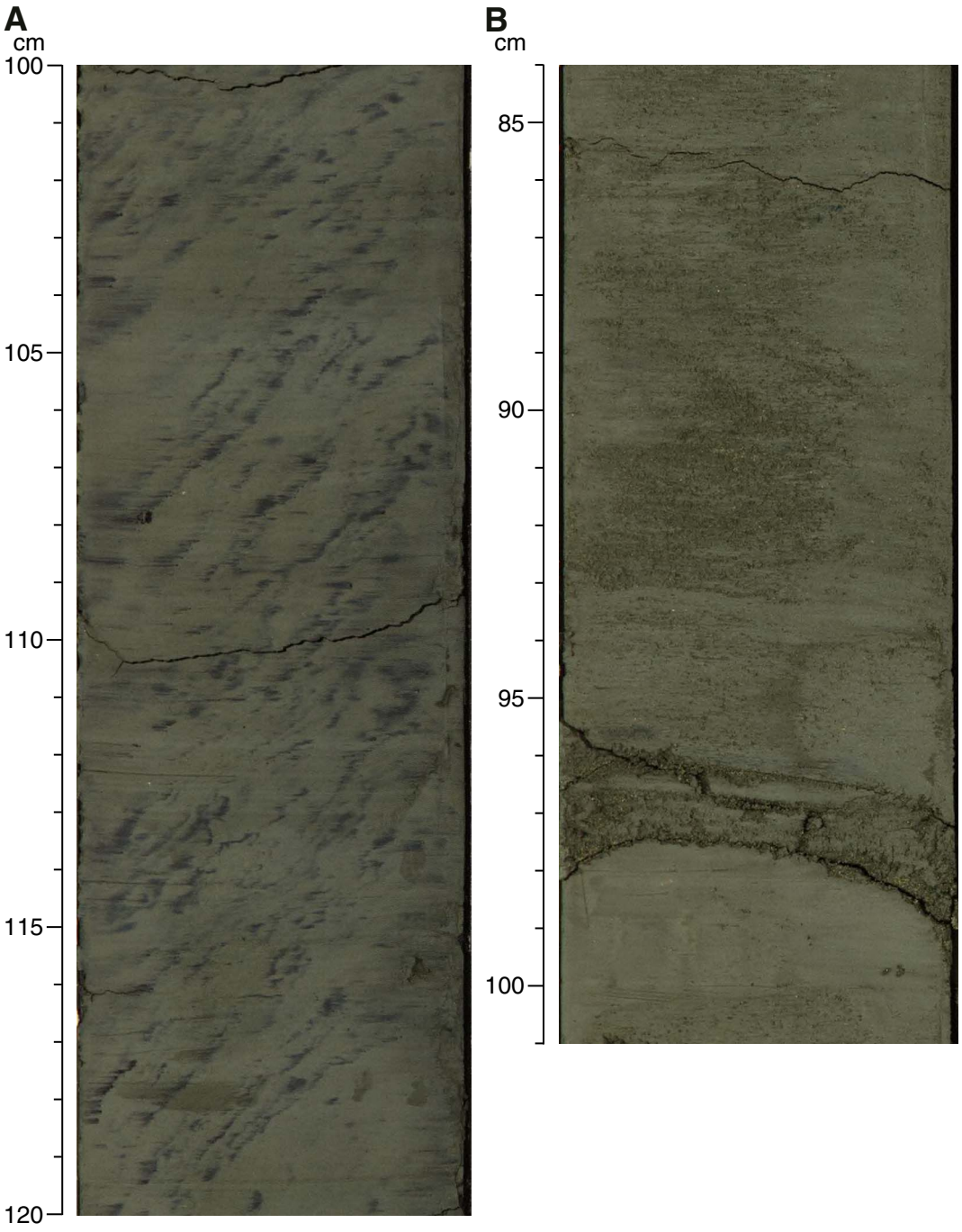

**Figure F8.** Glauconite distribution with depth based on smear slide analysis from Hole 1252A.

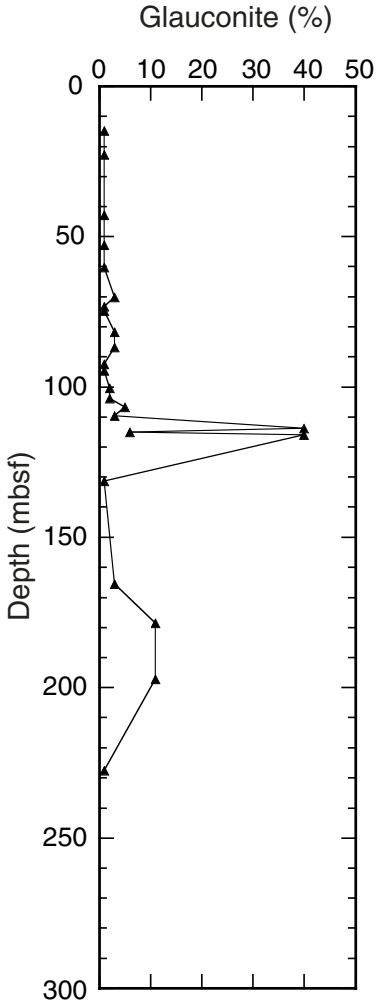

**Figure F9.** Close-up photograph of a glauconite sand layer in lithostratigraphic Unit III (interval 204-1252A-13H-3, 138–148 cm).

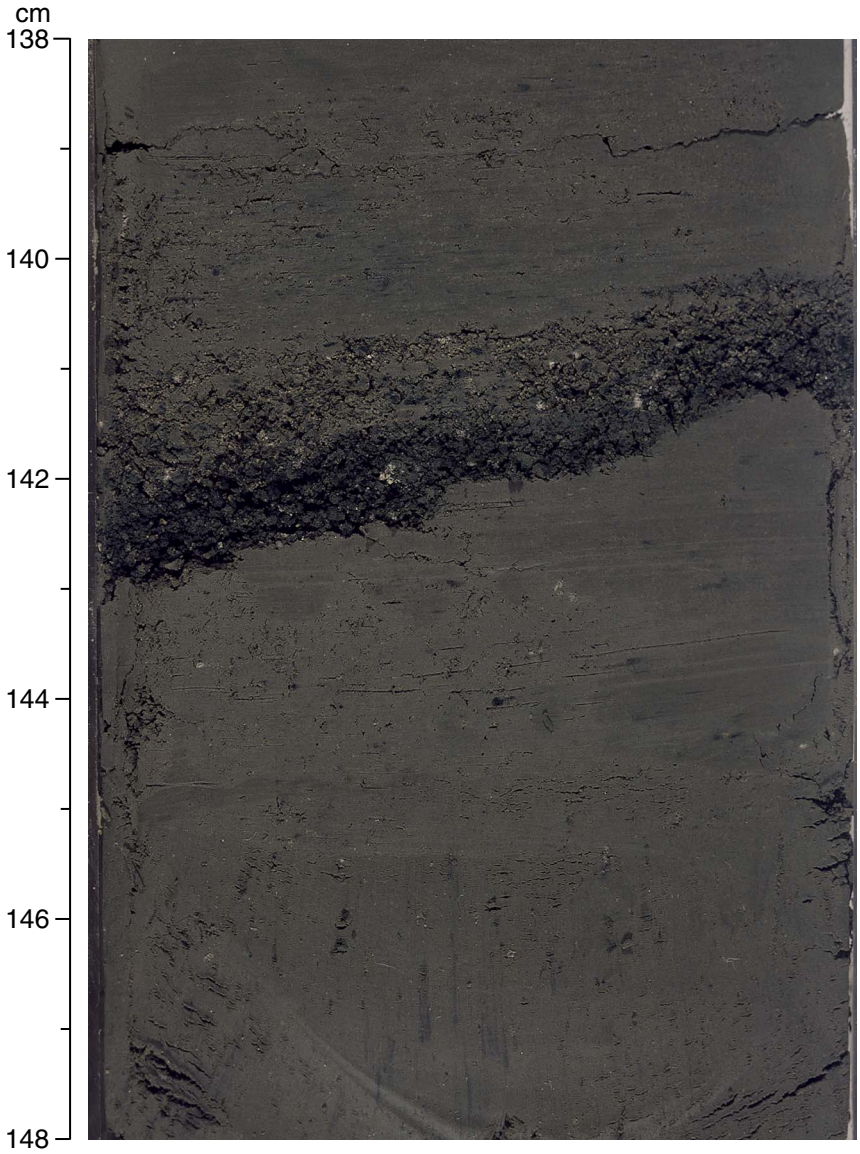

**Figure F10.** Close-up photograph of authigenic carbonate cements in lithostratigraphic Unit III (interval 204-1252A-19H-6, 15–35 cm).

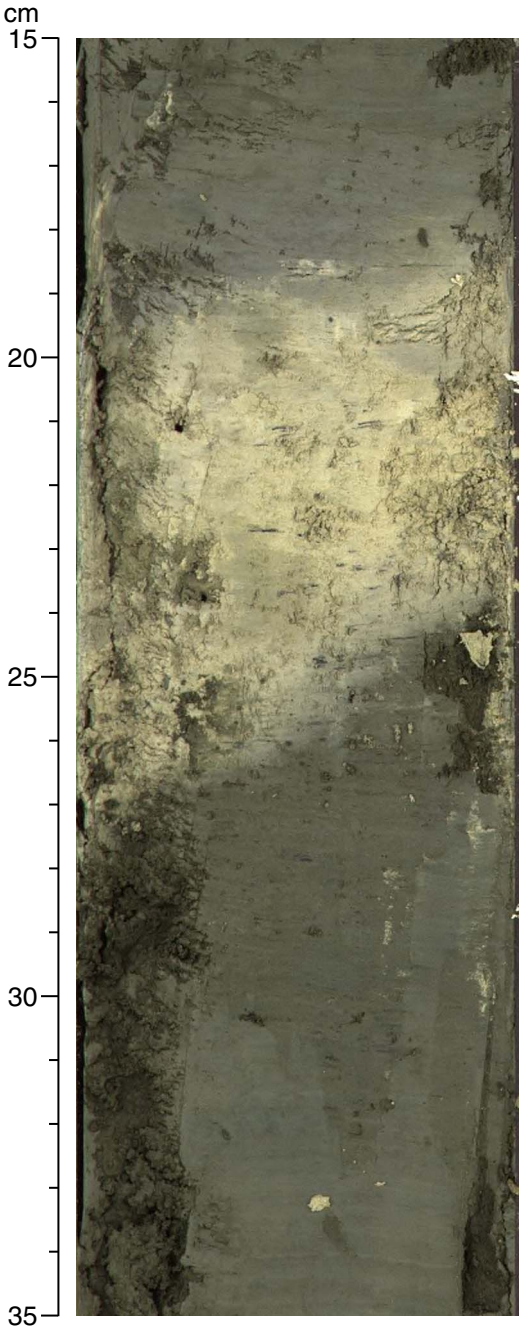

**Figure F11.** Close-up photograph of mousselike texture in lithostratigraphic Unit III (interval 204-1252A-15H-4, 50–61 cm).

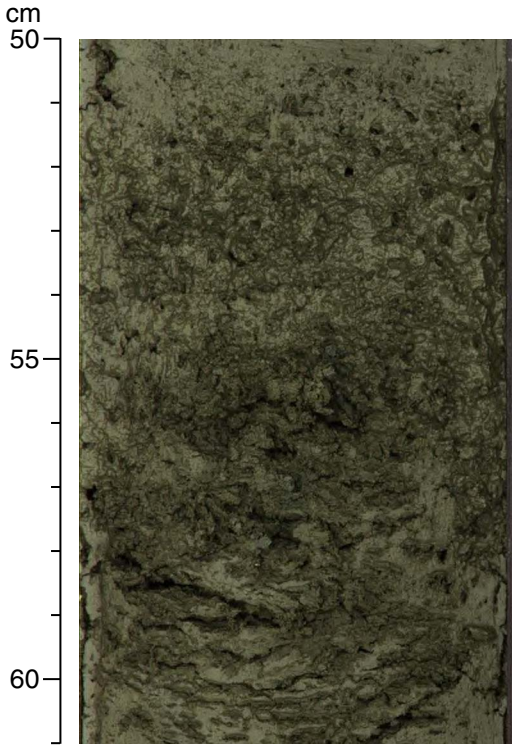

**Figure F12.** Age-depth plot based on diatom and calcareous nannofossil bioevents for Hole 1252A. The detailed age and depth of control points are shown in Table T2, p. 54, (1–10). D = diatom event, N = nannofossil event.

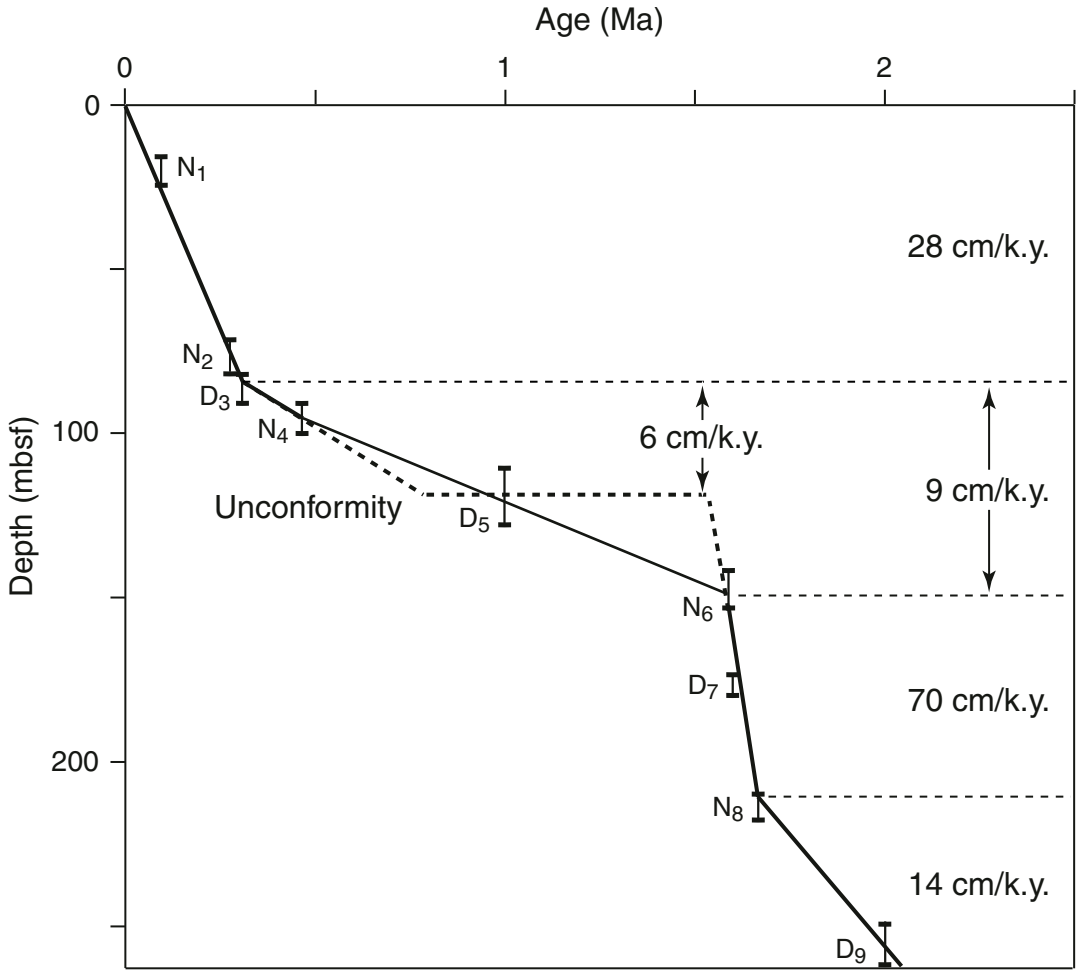

**Figure F13.** Concentration profiles of various dissolved species in pore waters at Site 1252.

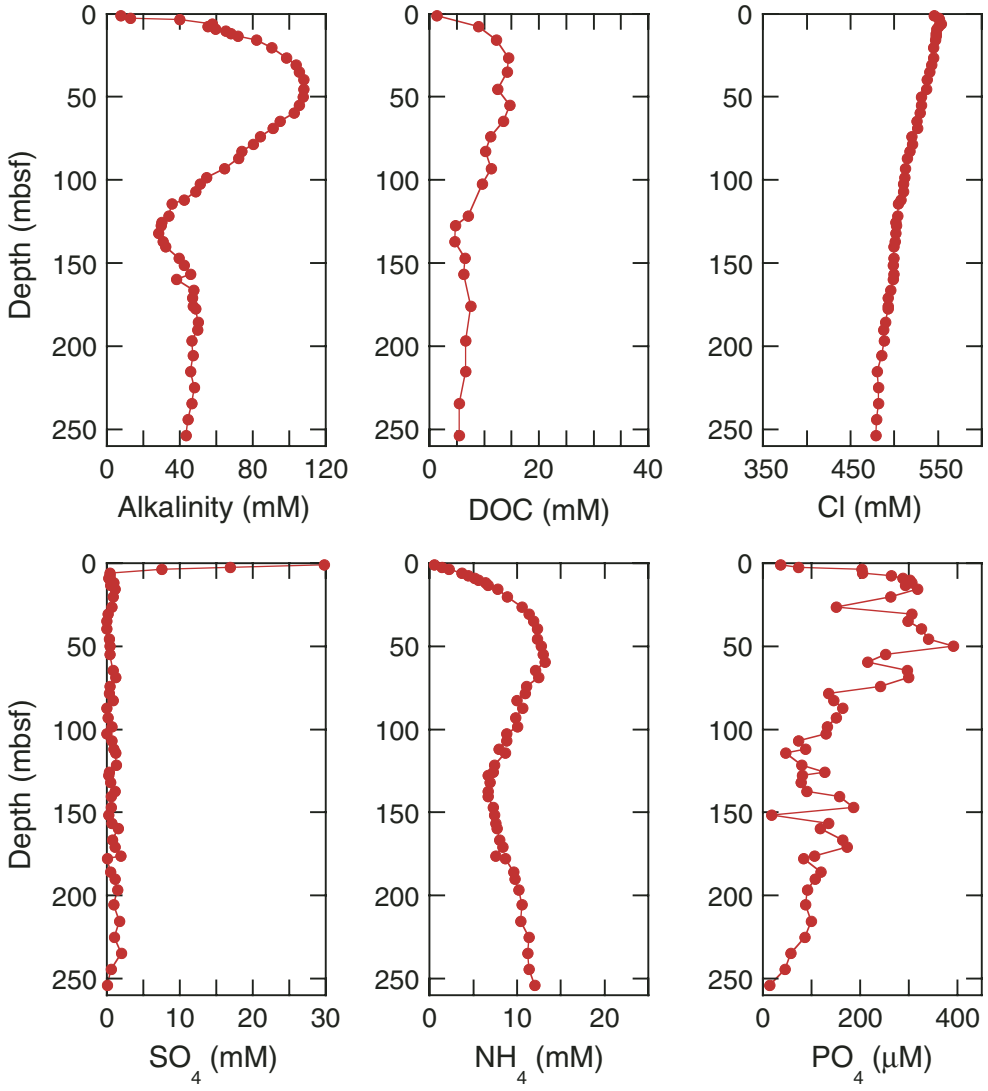

**Figure F14.** Chloride ($Cl^-$) concentration profile showing its relationship to the position of the reflectors in the multichannel seismic data at Site 1252. A major change in the chloride gradient occurs at the top of the accreted sediments at ~120 mbsf. Other slope changes occur at 165 mbsf, which might correspond to the bottom of the GHSZ, and at 214 mbsf.

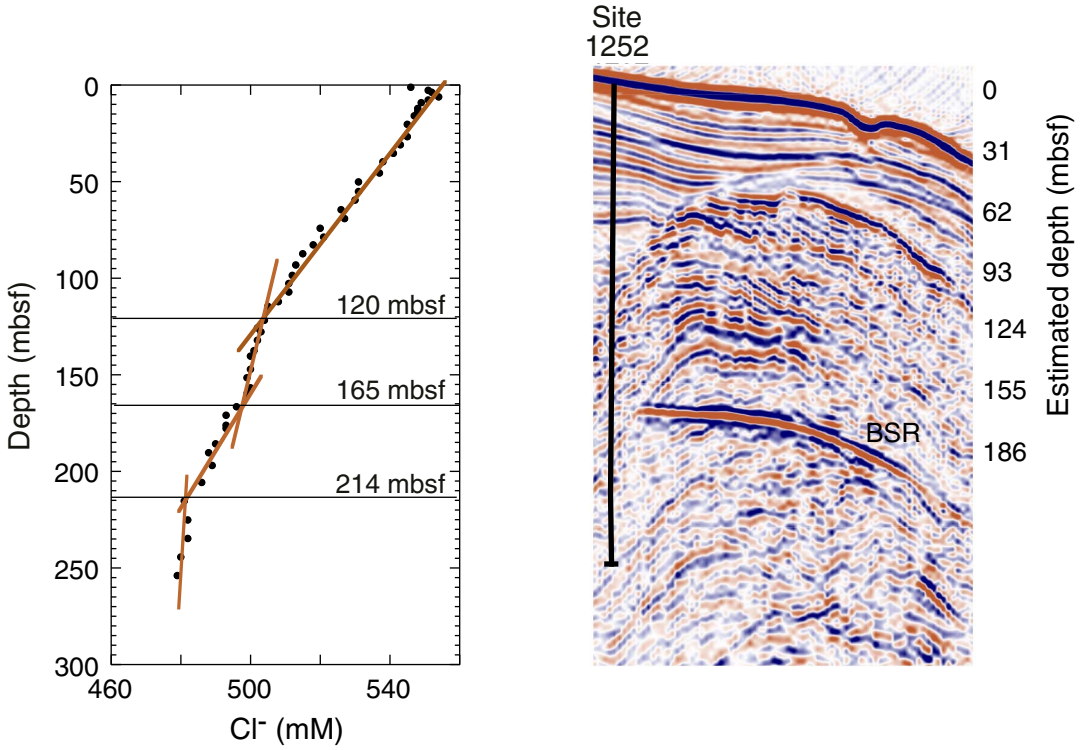

**Figure F15.** Sulfate ($SO_4^{2-}$) and methane ($CH_4$) concentration profiles in the upper 20 mbsf at Site 1252. Interstitial methane concentrations are from headspace data (see **"Organic Geochemistry,"** p. 12). The linear portion of the curve through the sulfate reduction zone was used to calculate upward methane flux at Site 1252, based on the shown linear regression. The sulfate/methane interface (SMI) is also shown.

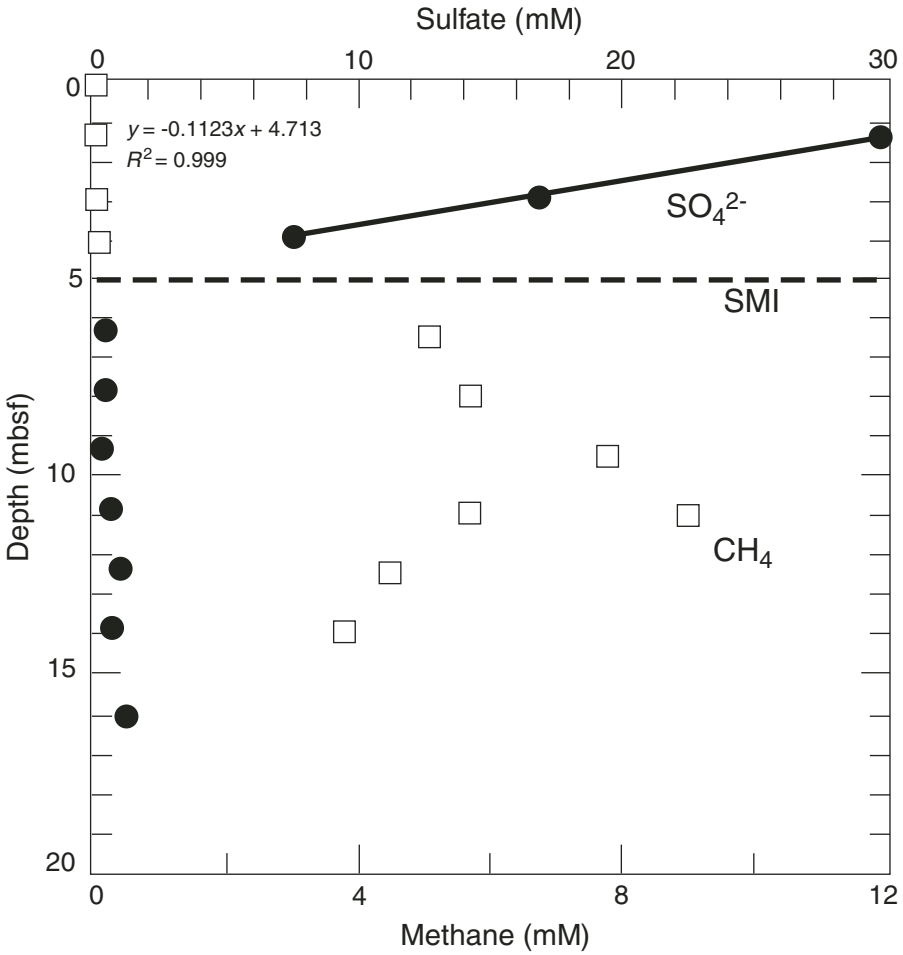

**Figure F16.** Headspace gas concentrations of $C_1$, $C_2$, $C_{2=}$, $C_3$, and $C_{3=}$ vs. depth at Site 1252.

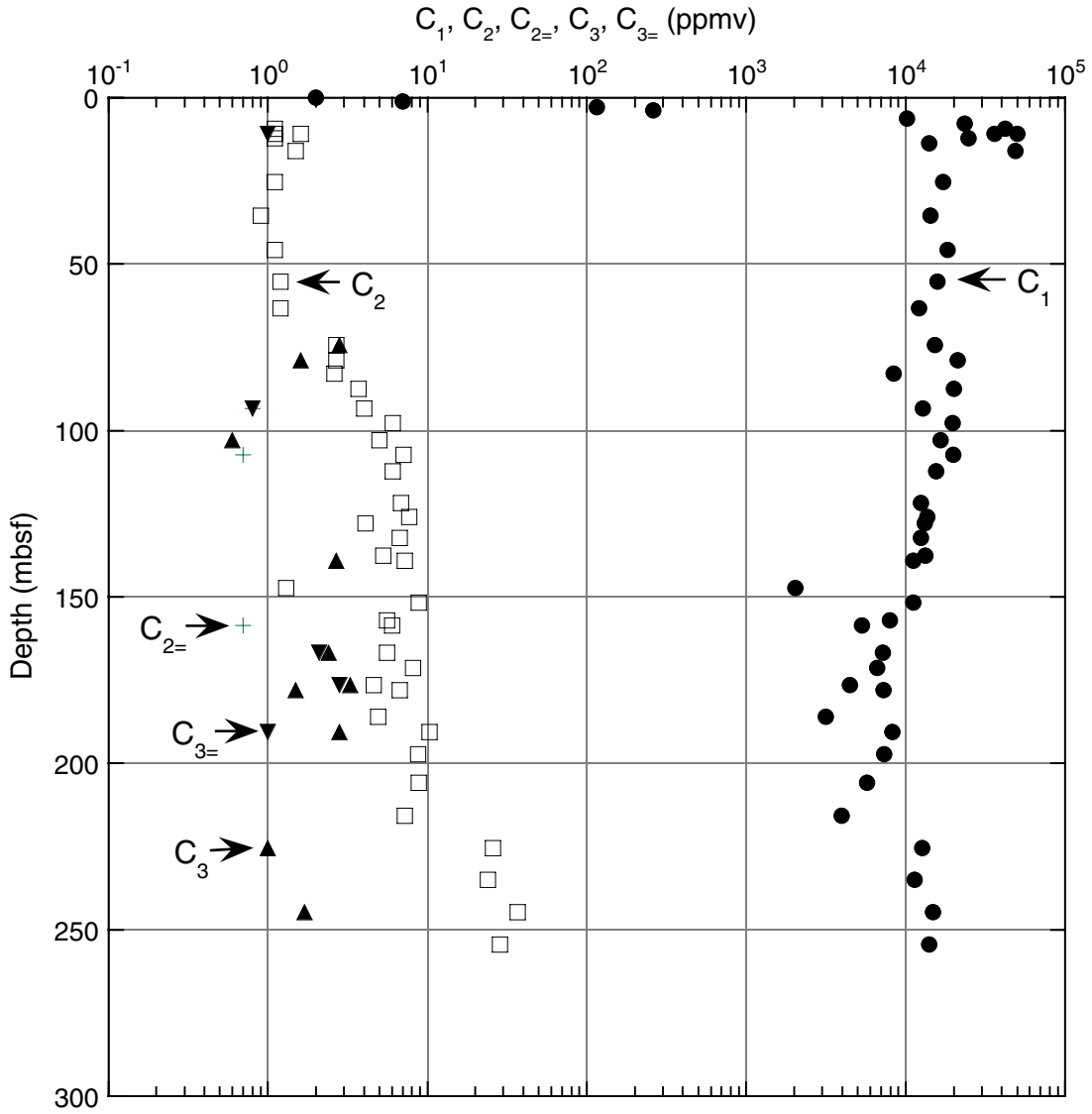

**Figure F17.** Dissolved residual methane ($CH_4$) and sulfate ($SO_4^{2-}$) in pore water. Methane concentration increases at the depth where sulfate concentration is depleted.

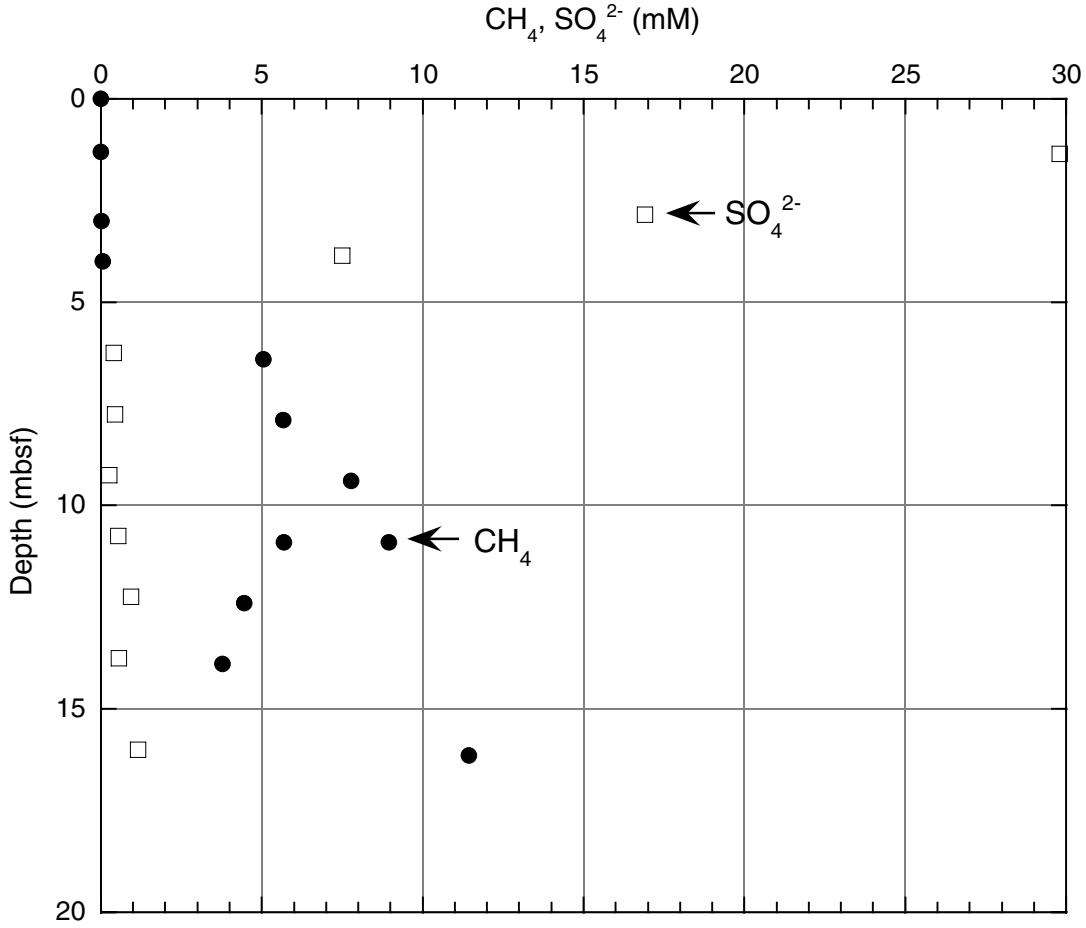

**Figure F18.** Concentrations of $C_1$, $C_2$, and $C_3$ in core void gas vs. depth at Site 1252.

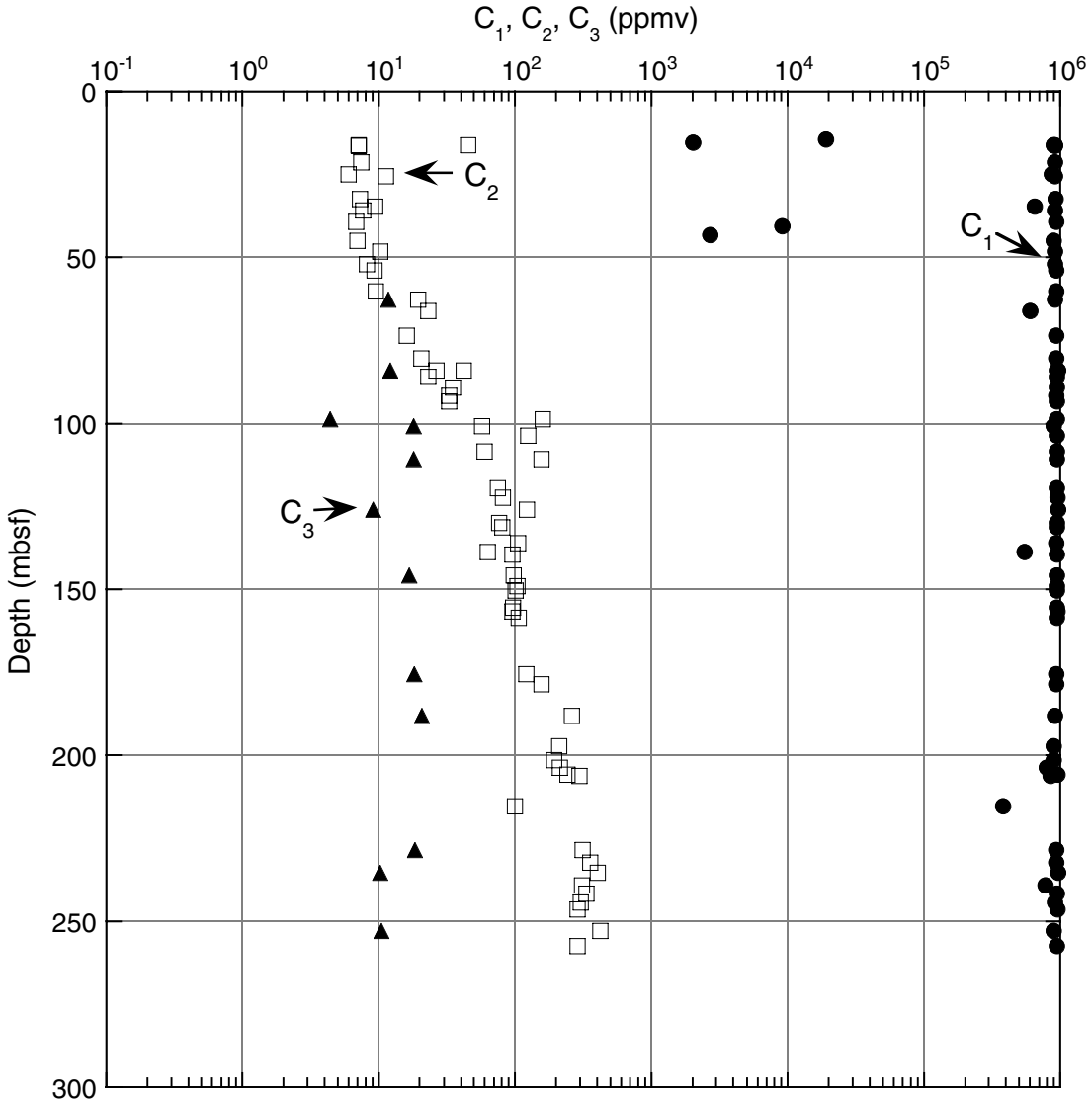

**Figure F19.** $C_1/C_2$ ratio vs. depth for Site 1252. HS = headspace gas, VAC = vacutainer.

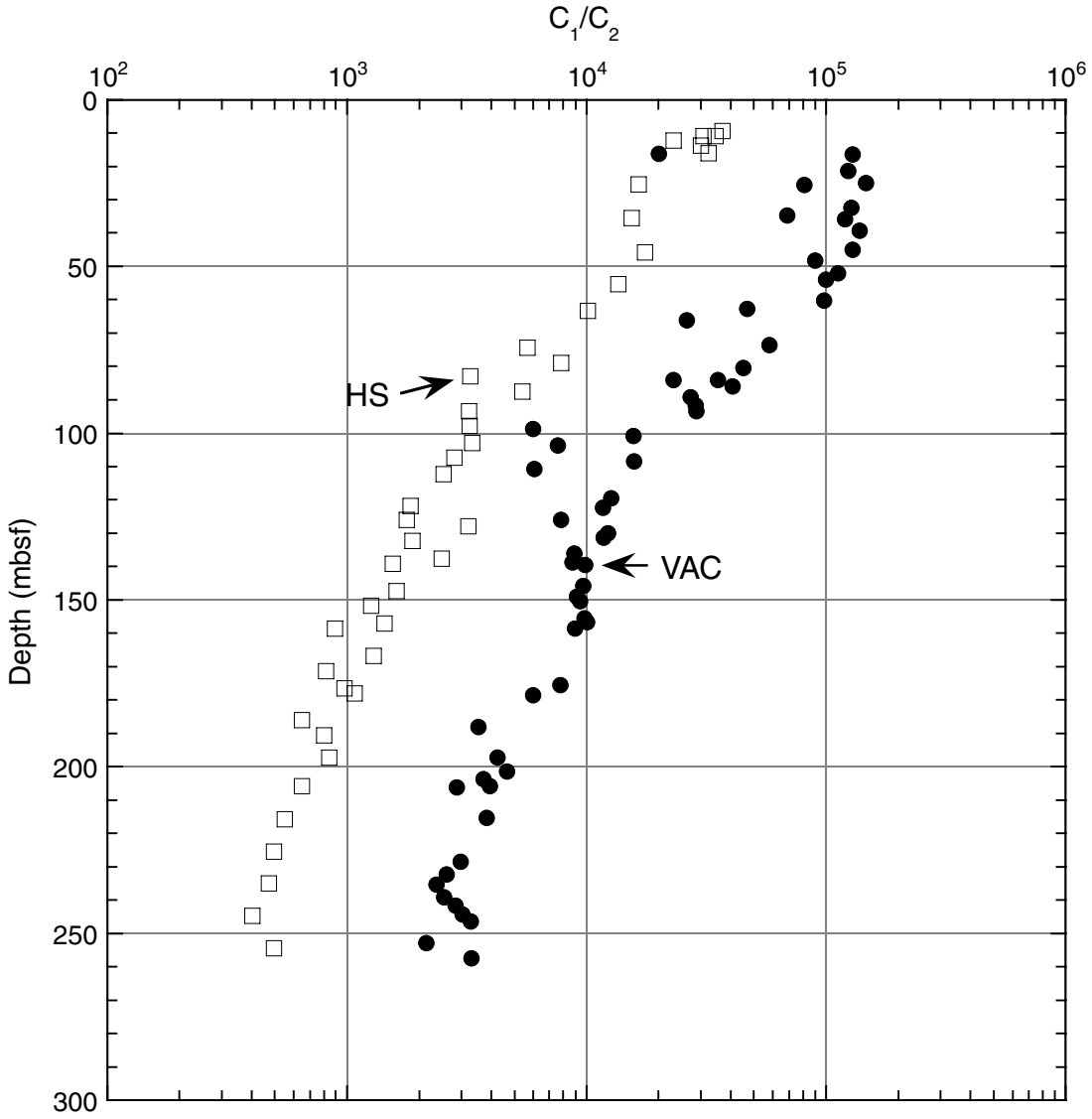

**Figure F20. A.** Downcore IR temperature profiles from Hole 1252. **B.** Downcore temperature profile for Cores 204-1252A-13H and 14H.

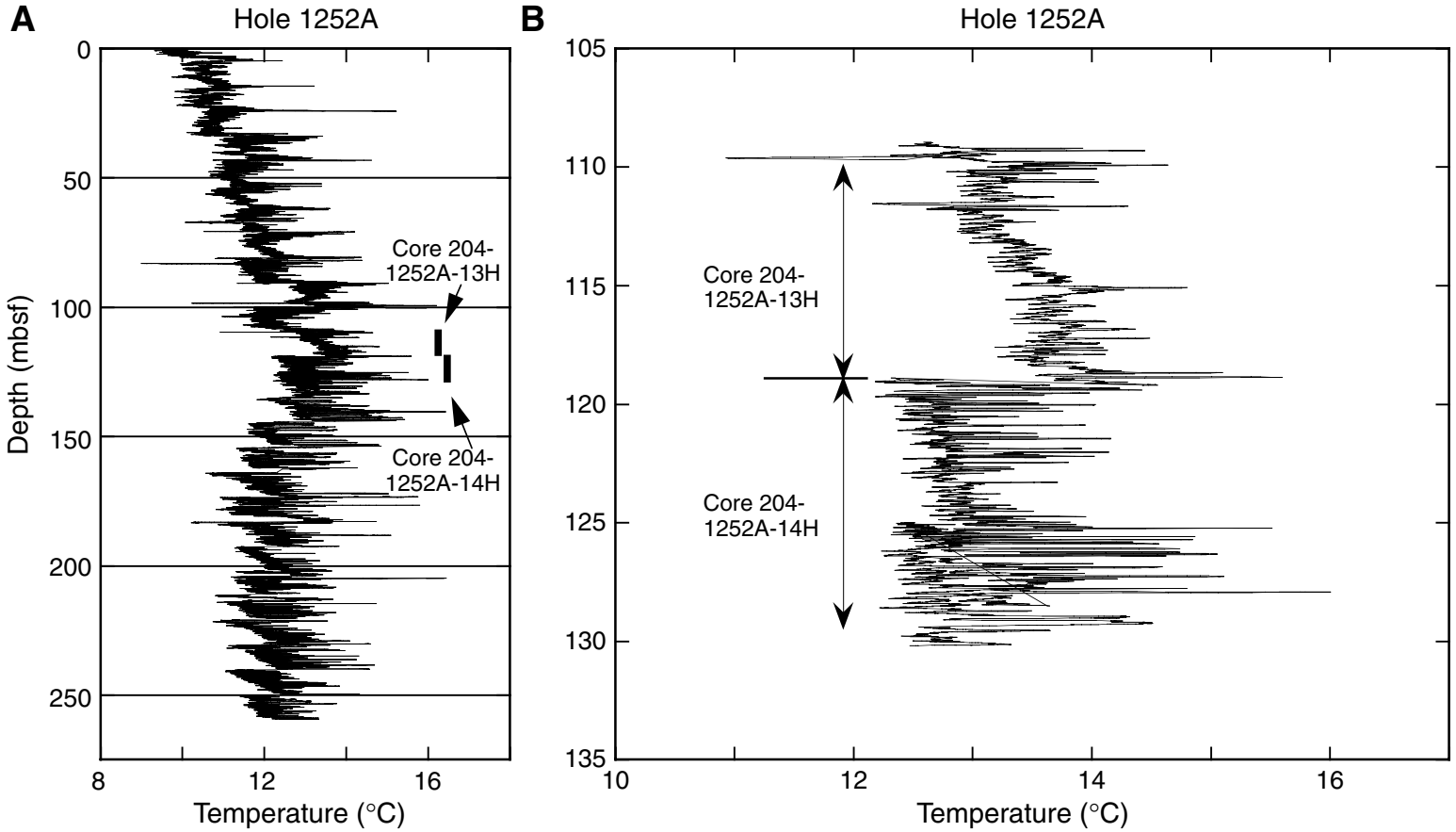

**Figure F21.** IR temperature anomalies ($\Delta T$) vs. depth.

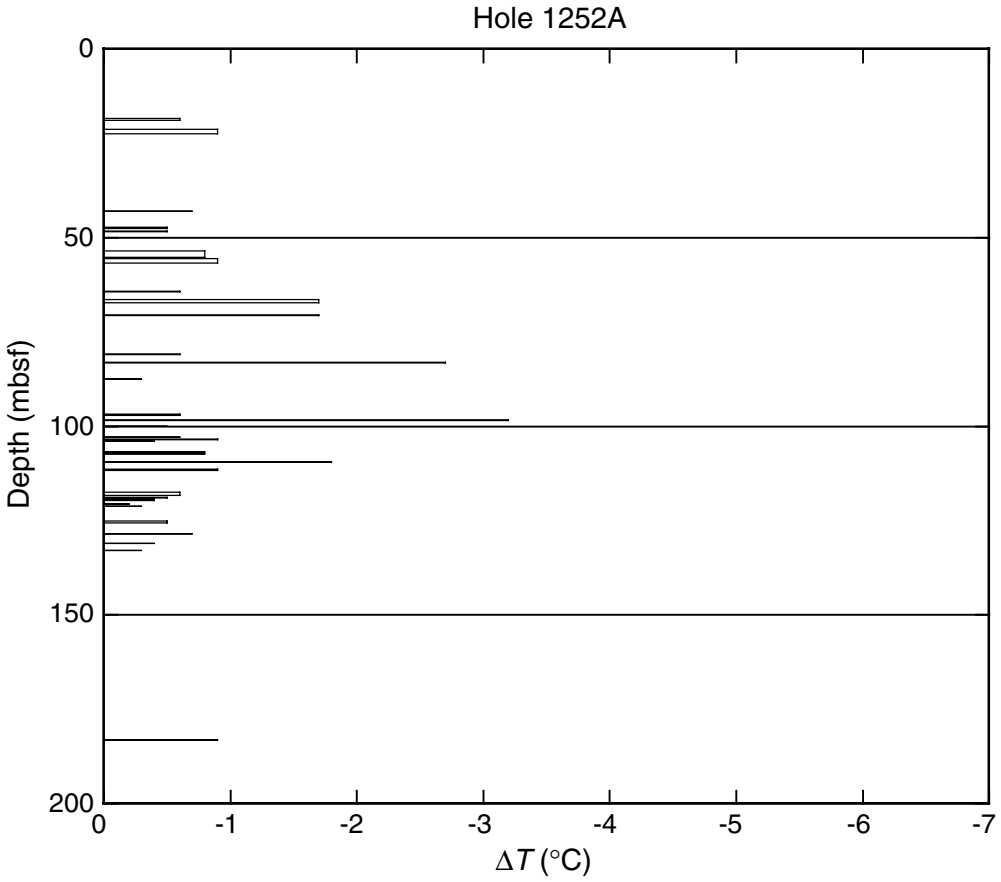

**Figure F22.** Overview of physical properties measured at Site 1252. GRA = gamma ray attenuation, MAD = moisture and density, GS = glauconite sand, CC = carbonate.

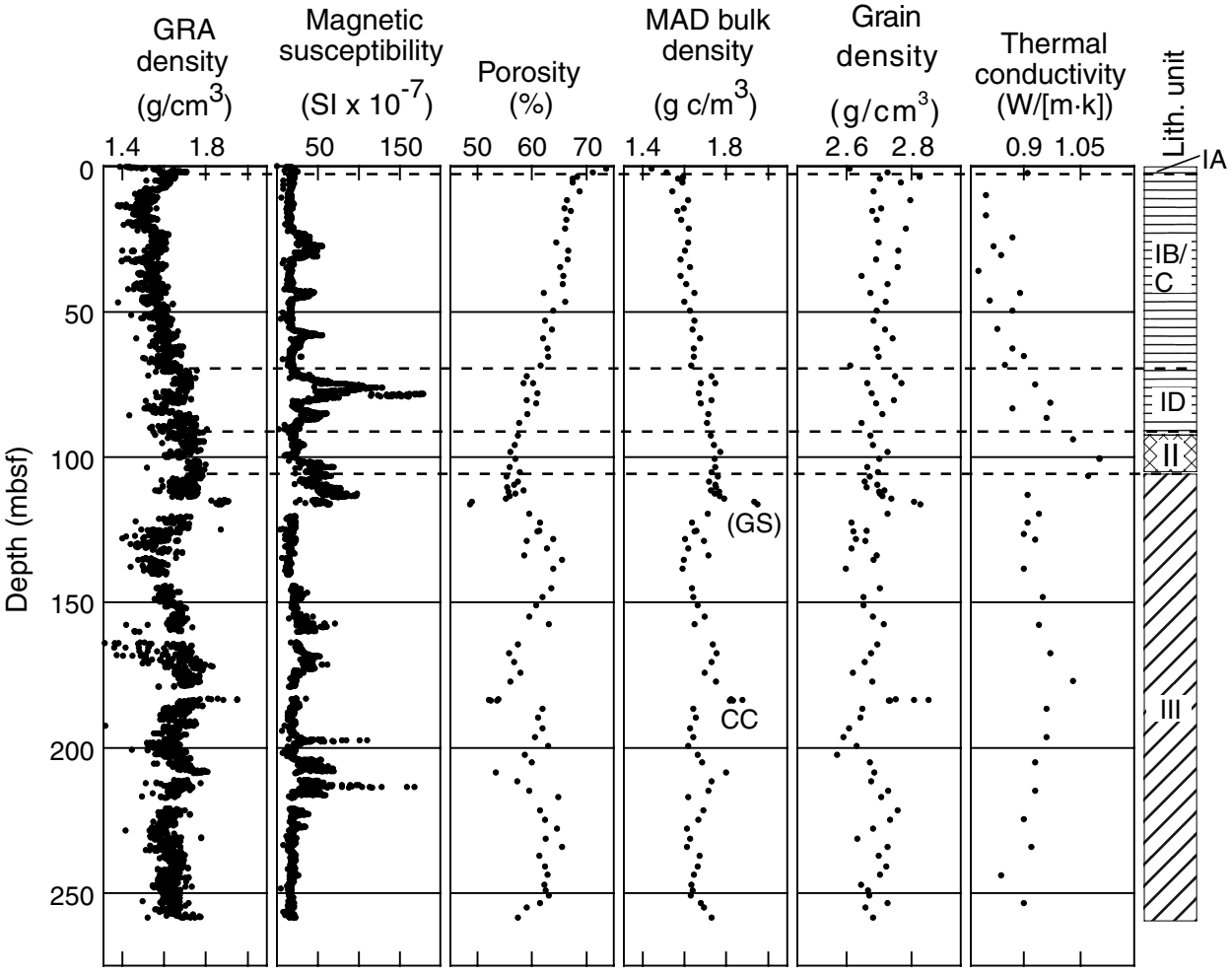

**Figure F23.** Comparison of physical properties with 3-D seismic data at Site 1252. GRA = gamma ray attenuation, MAD = moisture and density.

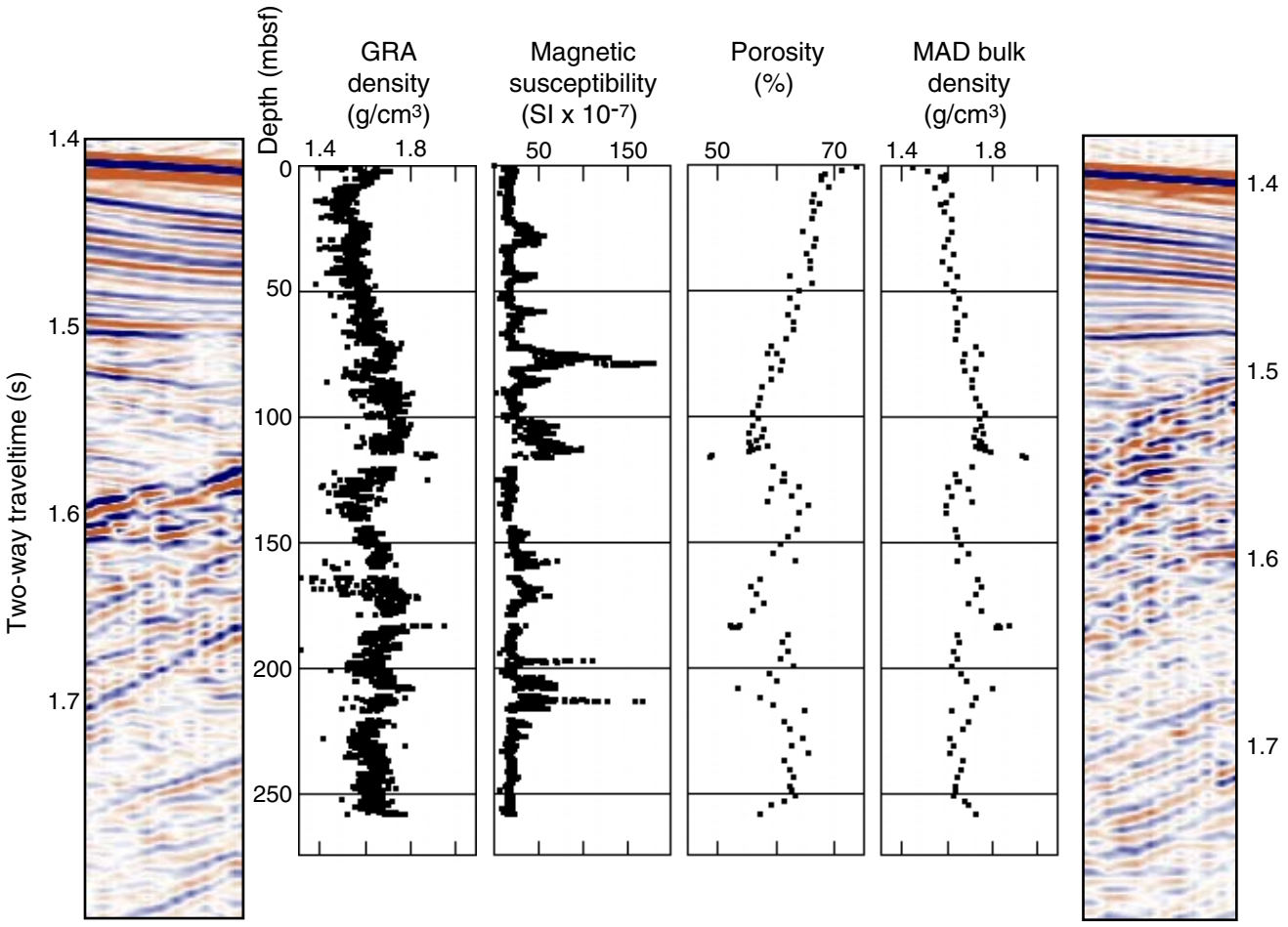

**Figure F24.** Temperature-time series recorded with the APCT tool at Site 1252.

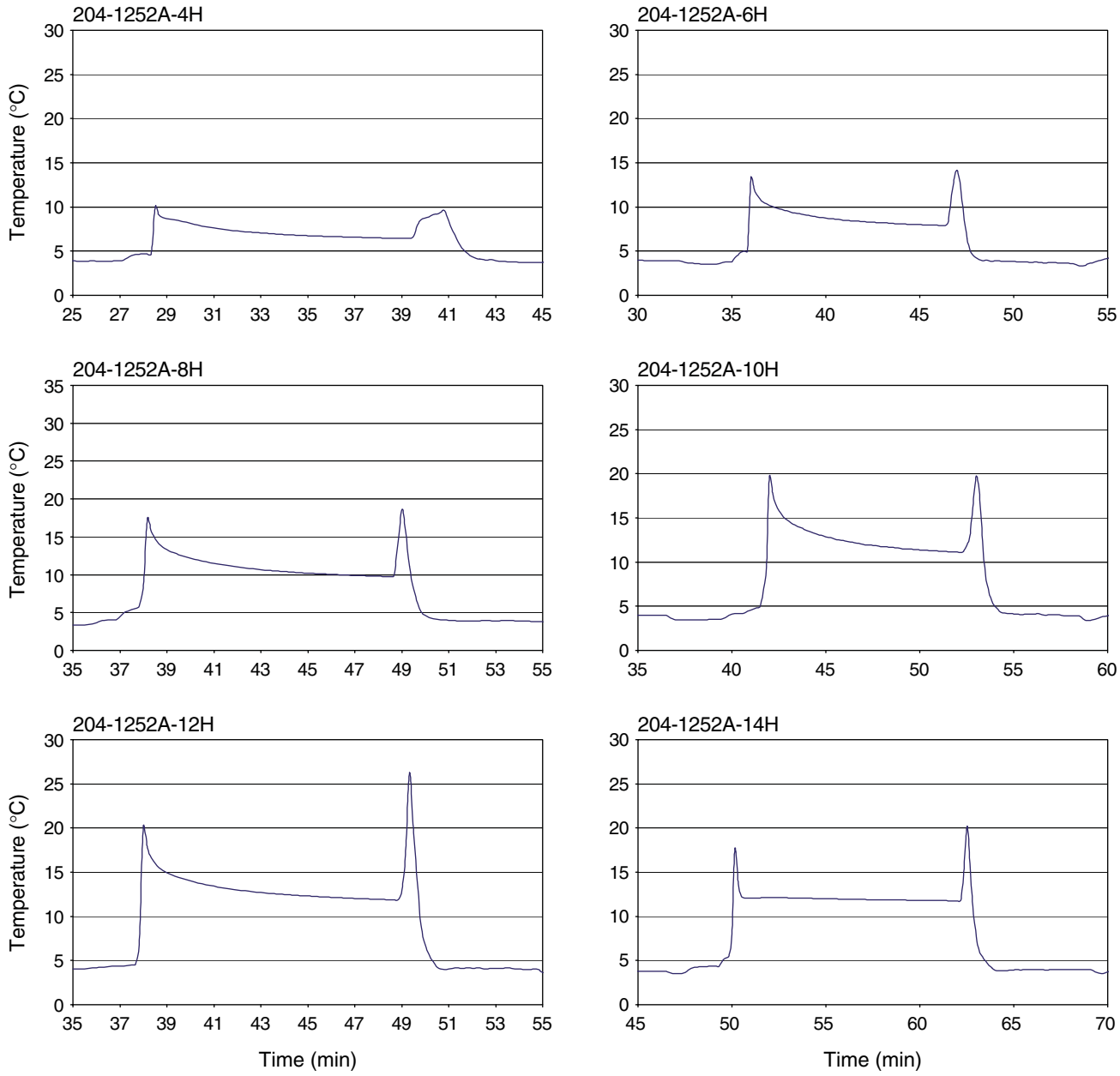

**Figure F25.** Estimated temperature as a function of depth at Site 1252.

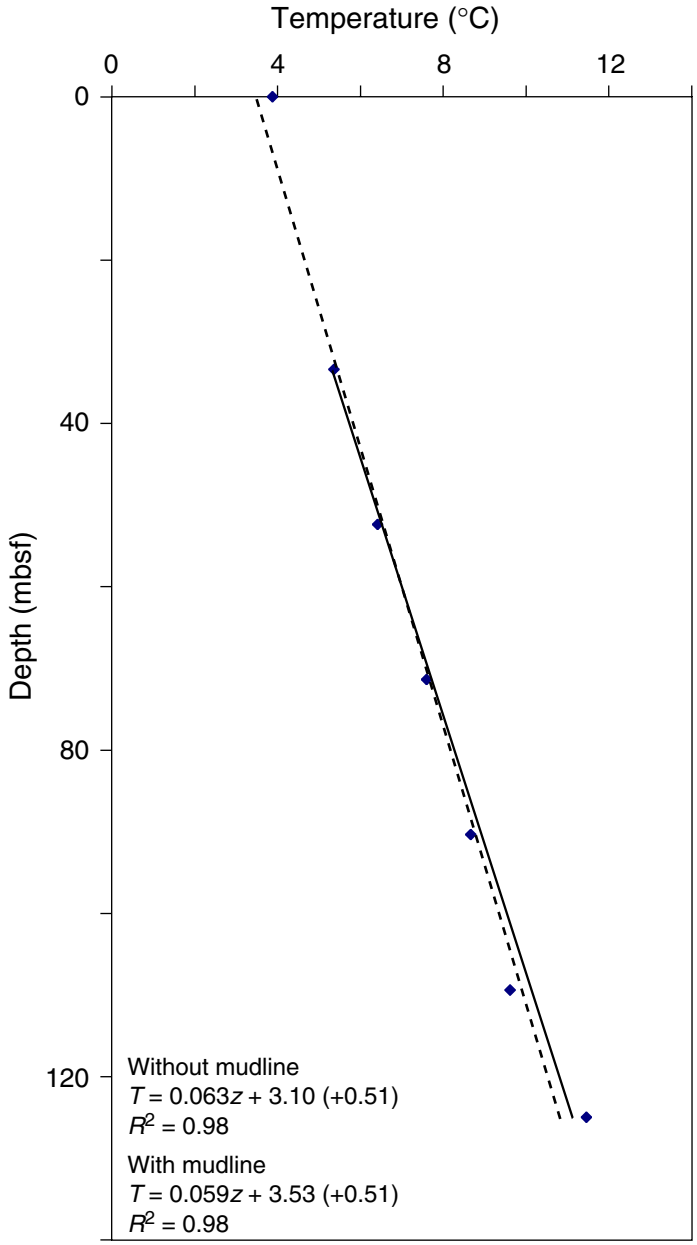

**Figure F26.** Summary of CWL data from Hole 1252A. gAPI = American Petroleum Institute gamma ray units, PEF = photoelectric effect factor, comp. = compressional.

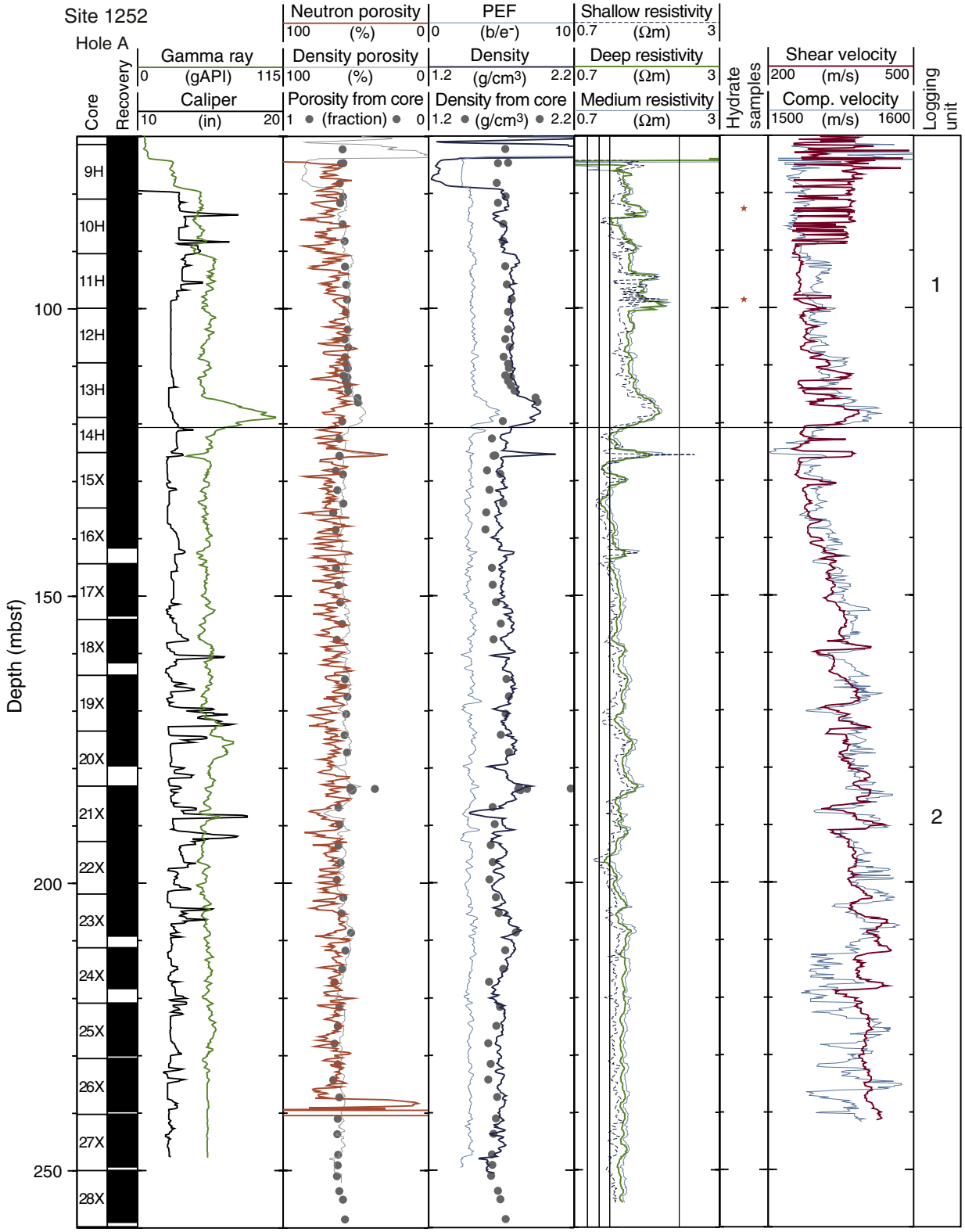

**Figure F27.** CWL gamma ray logging data from Hole 1252A. gAPI = American Petroleum Institute gamma ray units, FMS = Formation MicroScanner.

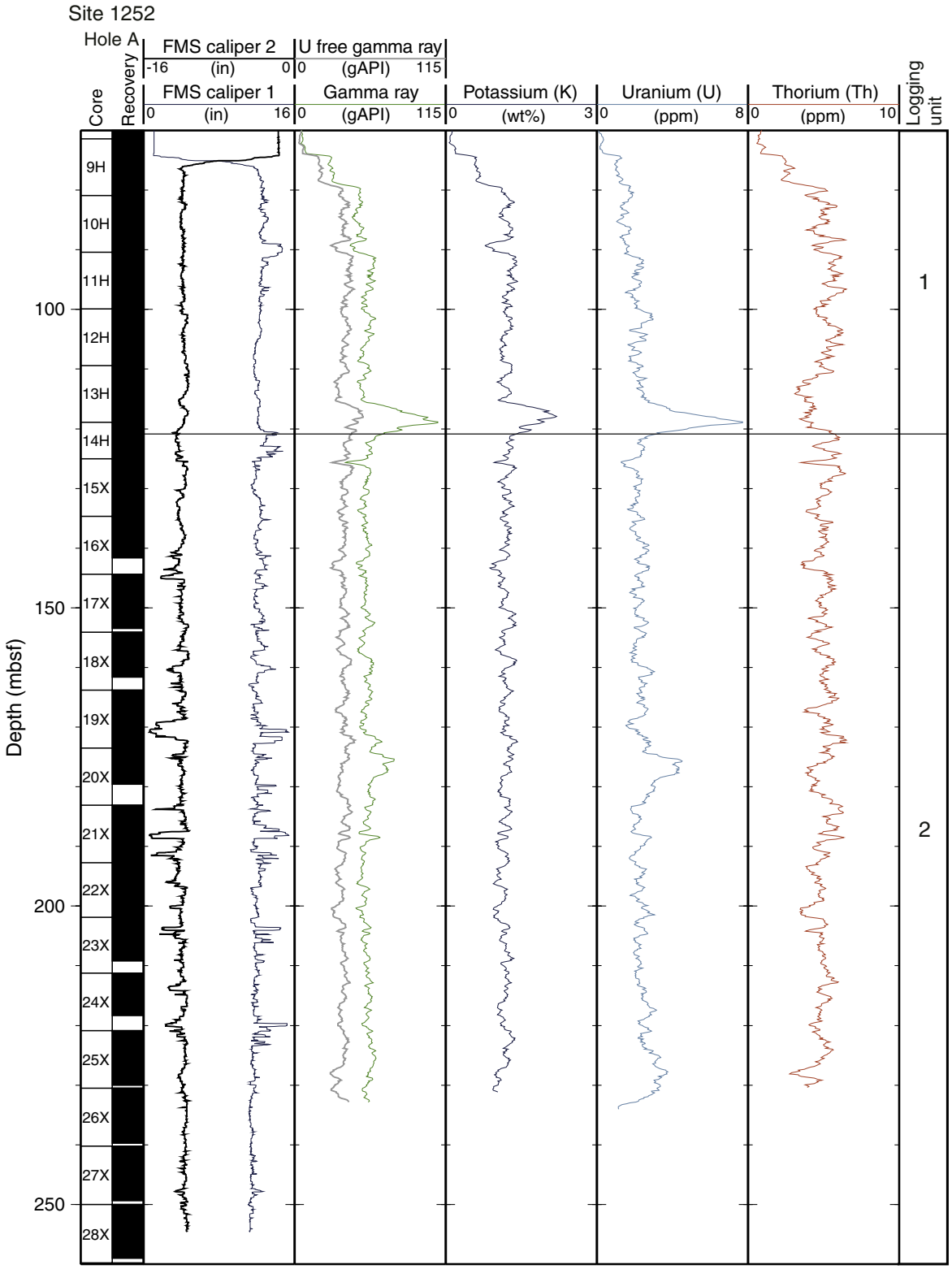

**Figure F28.** CWL acoustic logging data from Hole 1252A. The resistivity log is used as a reference indicator of the presence of gas hydrate. Low sonic waveform amplitudes are also possible indicators of gas hydrate. Sph. foc. res. = spherically focused resistivity.

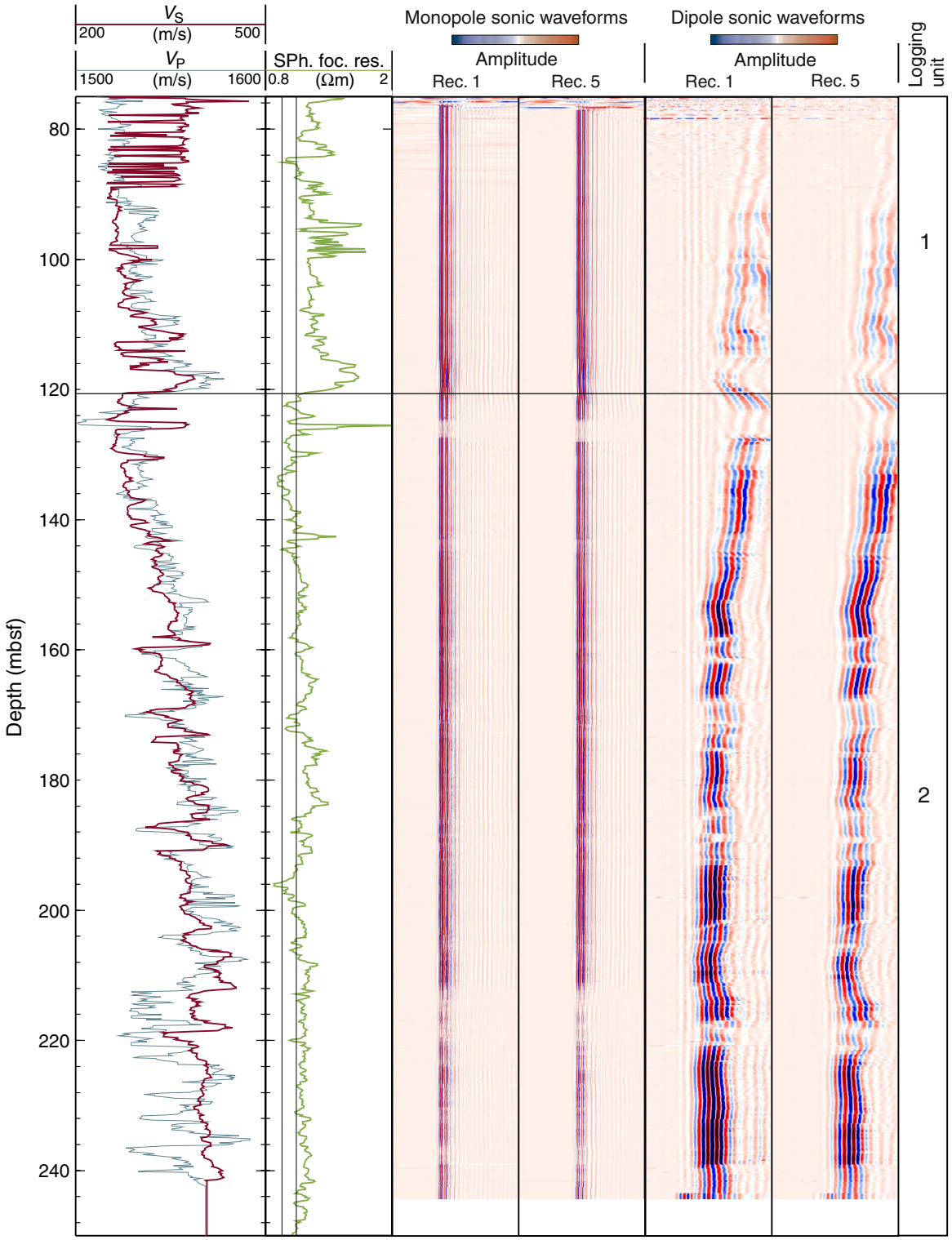

**Figure F29.** FMS image showing glauconite and carbonate horizons associated with the contact between logging Units 1 and 2 in Hole 1252A. gAPI = American Petroleum Institute gamma ray units, PEF = photoelectric effect factor, FMS = Formation MicroScanner.

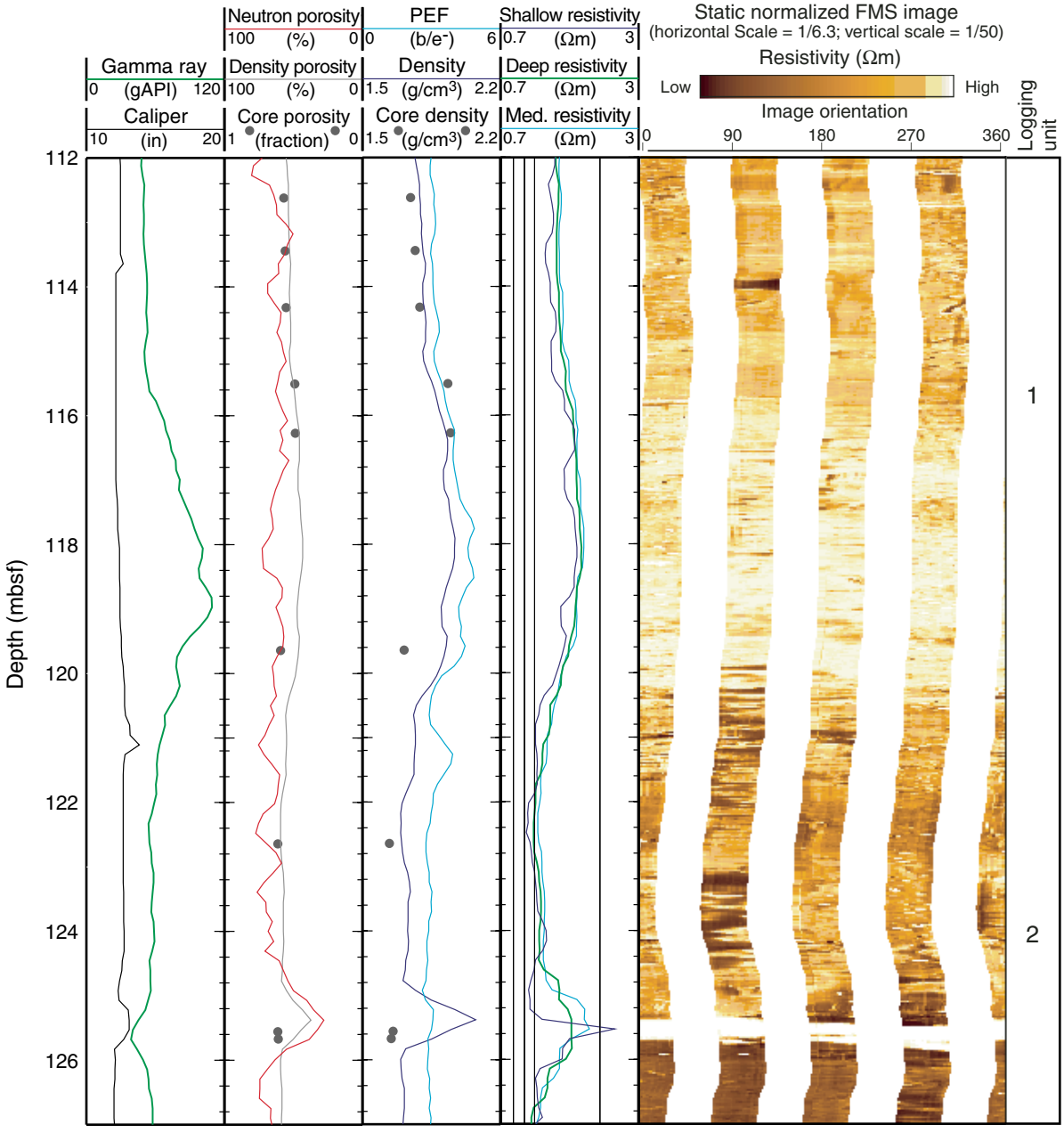

**Figure F30.** Borehole temperatures recorded with the TAP tool during the down and up pass of the three runs of the triple combo tool string in Hole 1252A.

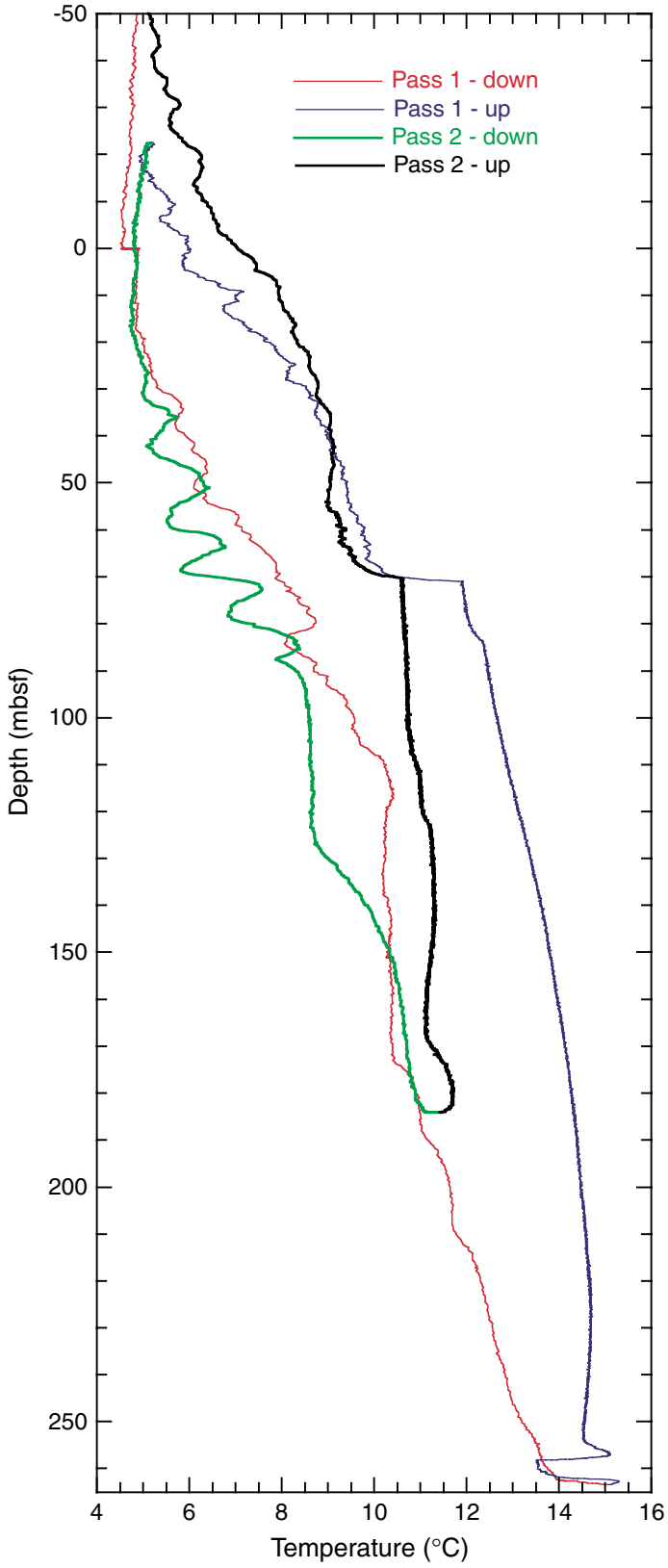

**Table T1.** Coring summary, Site 1252.

**Hole 1252A**
Latitude: 44°35.1671′N
Longitude: 125°5.5691′W
Time on site (hr): 51 (2100 hr, 29 Aug–0000 1 Sep 2002)
Time on hole (hr): 51 (2100 hr, 29 Aug–0000 1 Sep 2002)
Seafloor (drill pipe measurement from rig floor, mbrf): 1051
Distance between rig floor and sea level (m): 11.7
Water depth (drill pipe measurement from sea level, m): 1039.3
Total depth (drill pipe measurement from rig floor, mbrf): 1310.8
Total penetration (meters below seafloor, mbsf): 259.8
Total number of cores: 28
Total number of drilled intervals: 0
Total length of cored section (m): 259.8
Total core recovered (m): 253.79
Core recovery (%): 97.7

| Core | Date (Aug 2002) | Local time (hr) | Depth (mbsf) Top | Depth (mbsf) Bottom | Length (m) Cored | Length (m) Recovered | Recovery (%) |
|---|---|---|---|---|---|---|---|
| 204-1252A- | | | | | | | |
| 1H | 30 | 0340 | 0.0 | 4.9 | 4.9 | 4.94 | 100.8 |
| 2H | 30 | 0420 | 4.9 | 14.4 | 9.5 | 10.03 | 105.6 |
| 3H | 30 | 0455 | 14.4 | 23.9 | 9.5 | 9.50 | 100.0 |
| 4H | 30 | 0545 | 23.9 | 33.4 | 9.5 | 9.92 | 104.4 |
| 5H | 30 | 0610 | 33.4 | 42.9 | 9.5 | 10.10 | 106.3 |
| 6H | 30 | 0710 | 42.9 | 52.4 | 9.5 | 10.15 | 106.8 |
| 7H | 30 | 0745 | 52.4 | 61.9 | 9.5 | 9.38 | 98.7 |
| 8H | 30 | 0835 | 61.9 | 71.4 | 9.5 | 9.57 | 100.7 |
| 9H | 30 | 0905 | 71.4 | 80.9 | 9.5 | 9.93 | 104.5 |
| 10H | 30 | 1000 | 80.9 | 90.4 | 9.5 | 9.95 | 104.7 |
| 11H | 30 | 1035 | 90.4 | 99.9 | 9.5 | 10.24 | 107.8 |
| 12H | 30 | 1125 | 99.9 | 109.4 | 9.5 | 10.21 | 107.5 |
| 13H | 30 | 1200 | 109.4 | 118.9 | 9.5 | 10.21 | 107.5 |
| 14H | 30 | 1300 | 118.9 | 125.0 | 6.1 | 9.87 | 161.8 |
| 15X | 30 | 1430 | 125.0 | 134.7 | 9.7 | 9.70 | 100.0 |
| 16X | 30 | 1520 | 134.7 | 144.4 | 9.7 | 6.92 | 71.3 |
| 17X | 30 | 1620 | 144.4 | 154.1 | 9.7 | 9.06 | 93.4 |
| 18X | 30 | 1725 | 154.1 | 163.8 | 9.7 | 7.53 | 77.6 |
| 19X | 30 | 1820 | 163.8 | 173.5 | 9.7 | 9.64 | 99.4 |
| 20X | 30 | 1920 | 173.5 | 183.1 | 9.6 | 6.09 | 63.4 |
| 21X | 30 | 2000 | 183.1 | 192.7 | 9.6 | 9.92 | 103.3 |
| 22X | 30 | 2040 | 192.7 | 201.9 | 9.2 | 9.89 | 107.5 |
| 23X | 30 | 2130 | 201.9 | 211.2 | 9.3 | 7.27 | 78.2 |
| 24X | 30 | 2215 | 211.2 | 220.9 | 9.7 | 7.12 | 73.4 |
| 25X | 30 | 2305 | 220.9 | 230.5 | 9.6 | 9.15 | 95.3 |
| 26X | 30 | 2350 | 230.5 | 240.2 | 9.7 | 9.20 | 94.8 |
| 27X | 31 | 0040 | 240.2 | 250.0 | 9.8 | 9.19 | 93.8 |
| 28X | 31 | 0140 | 250.0 | 259.8 | 9.8 | 9.01 | 91.9 |
| | | | | Cored totals: | 259.8 | 253.69 | 97.7 |
| | | | | Drilled total: | 0.0 | | |
| | | | | Total: | 259.8 | | |

**Table T2.** Bioevents, Hole 1252A.

| Age (Ma) | Bioevent | Top | | Bottom | | Average depth (mbsf) | Event number* | Comment |
|---|---|---|---|---|---|---|---|---|
| | | Core, section | Depth (mbsf) | Core, section | Depth (mbsf) | | | |
| | | 204-1252A- | | 204-1252A- | | | | |
| 0.09 | FO *Emiliania huxleyi* Acme | 2H-CC | 14.88 | 3H-CC | 23.84 | 19.36 | 1 | Nannofossil |
| 0.27 | FO *Emiliania huxleyi* | 8H-CC | 71.42 | 9H-CC | 81.28 | 76.35 | 2 | Nannofossil |
| 0.30 | LO *Proboscia curvirostris* | 9H-CC | 81.28 | 10H-CC | 90.80 | 86.04 | 3 | Diatom |
| 0.46 | LO *Pseudoemiliania lacunosa* | 10H-CC | 90.80 | 11H-CC | 100.59 | 95.70 | 4 | Nannofossil |
| 1.0 | LO *Actinocyclus oculatus* | 12H-CC | 110.04 | 14H-CC | 128.72 | 119.38 | 5 | Diatom |
| 1.59 | FO *Calcydiscus macintyrei* | 16X-CC | 141.57 | 17X-CC | 153.30 | 147.44 | 6 | Nannofossil |
| 1.6 | FO *Proboscia curvirostris* | 19X-CC | 173.39 | 20X-CC | 179.54 | 176.47 | 7 | Diatom |
| 1.67 | FO *Gephyrocapsa lumina* | 23X-CC | 209.12 | 24X-CC | 218.32 | 213.72 | 8 | Nannofossil |
| 2.0 | LO *Neodenticula koizumii* | 27X-CC | 249.34 | 28X-CC | 258.96 | 254.15 | 9 | Diatom |

Notes: * = number in Figure F12, p. 34. FO = first occurrence, LO = last occurrence.

**Table T3.** Interstitial water data, Site 1252.

| Core, section, interval (cm) | Depth (mbsf) | pH | Alkalinity (mM) | Salinity (g/kg) | Cl (mM) | $SO_4$ (mM) | $NH_4$ (mM) | $PO_4$ (µM) | DOC (mM) |
|---|---|---|---|---|---|---|---|---|---|
| 204-1252A- | | | | | | | | | |
| 1H-1, 135–150 | 1.35 | 7.41 | 7.60 | 34 | 546 | 29.8 | 0.5 | 37 | 1.38 |
| 1H-2, 135–150 | 2.85 | 7.35 | 12.91 | 34 | 551 | 16.9 | 1.5 | 74 | — |
| 1H-3, 85–100 | 3.85 | 7.39 | 39.98 | 35 | 552 | 7.5 | 2.2 | 204 | — |
| 2H-1, 135–150 | 6.25 | 7.46 | 57.84 | 35 | 554 | 0.4 | 3.7 | 206 | — |
| 2H-2, 135–150 | 7.75 | 7.43 | 55.57 | 35 | 551 | 0.4 | 4.4 | 264 | 8.93 |
| 2H-3, 135–150 | 9.25 | 7.25 | 59.62 | 35 | 549 | 0.3 | 5.2 | 288 | — |
| 2H-4, 135–150 | 10.75 | 7.30 | 65.07 | 35 | — | 0.5 | 5.6 | 303 | — |
| 2H-5, 135–150 | 12.25 | 7.28 | 68.01 | 35 | 548 | 0.9 | 6.4 | 306 | — |
| 2H-6, 135–150 | 13.75 | 7.38 | 71.93 | 36 | 548 | 0.5 | 6.7 | 294 | — |
| 3H-2, 135–150 | 16.00 | 7.14 | 82.09 | 36 | 547 | 1.1 | 7.8 | 318 | 12.31 |
| 3H-5, 135–150 | 20.50 | 7.51 | 90.61 | 37 | 545 | 0.9 | 8.9 | 263 | — |
| 4H-2, 135–150 | 26.75 | 7.35 | 98.65 | 37 | 545 | 0.7 | 10.6 | 151 | 14.54 |
| 4H-5, 135–150 | 31.13 | 7.06 | 103.95 | 37 | 543 | 0.2 | 11.4 | 306 | — |
| 5H-2, 135–150 | 35.34 | 7.37 | 105.55 | 37 | 541 | 0.0 | 11.9 | 299 | 14.21 |
| 5H-5, 135–150 | 39.84 | 7.23 | 108.21 | 38 | 538 | 0.0 | 12.3 | 326 | — |
| 6H-2, 135–150 | 45.75 | 7.31 | 108.24 | 37 | 537 | 0.3 | 12.3 | 340 | 12.53 |
| 6H-5, 135–150 | 50.25 | 7.16 | 107.90 | 37 | 531 | 0.4 | 12.8 | 392 | — |
| 7H-2, 135–150 | 55.25 | 7.36 | 105.45 | 37 | 531 | 0.4 | 13.0 | 252 | 14.73 |
| 7H-5, 135–150 | 59.75 | 7.26 | 102.71 | 36 | 530 | — | 13.3 | 215 | — |
| 8H-2, 135–150 | 64.75 | 7.71 | 95.21 | 36 | 526 | 0.8 | 12.1 | 297 | 13.51 |
| 8H-5, 135–150 | 69.25 | 7.59 | 91.12 | 36 | 527 | 1.2 | 12.5 | 300 | — |
| 9H-2, 135–150 | 74.25 | 7.21 | 84.35 | 35 | 520 | 0.4 | 11.1 | 241 | 11.25 |
| 9H-5, 135–150 | 78.75 | 7.22 | 80.37 | 35 | 521 | 0.4 | 11.0 | 135 | — |
| 10H-2, 45–60 | 82.85 | 7.22 | 74.03 | 34 | 518 | 0.9 | 10.0 | 147 | 10.31 |
| 10H-5, 135–150 | 87.35 | 7.07 | 72.30 | 34 | 515 | 0.0 | 10.6 | 164 | — |
| 11H-2, 135–150 | 93.25 | 7.51 | 64.53 | 34 | 513 | 0.1 | 9.9 | 150 | 11.29 |
| 11H-6, 80–95 | 98.70 | 7.67 | 54.61 | 32 | 512 | 0.7 | 10.1 | 133 | — |
| 12H-2, 135–150 | 102.75 | 7.26 | 51.14 | 32 | 511 | 0.0 | 8.9 | 130 | 9.70 |
| 12H-5, 135–150 | 107.15 | 7.40 | 48.81 | 32 | 511 | 0.7 | 8.9 | 73 | — |
| 13H-2, 135–150 | 112.25 | 7.40 | 42.34 | 32 | 508 | 0.9 | 7.9 | 88 | — |
| 13H-4, 67–87 | 114.57 | 7.72 | 35.61 | 31 | 505 | 1.2 | 8.7 | 48 | — |
| 14H-2, 135–150 | 121.75 | 7.69 | 33.81 | 30 | 504 | 1.3 | 7.5 | 81 | 7.13 |
| 14H-5, 102–127 | 125.84 | 7.17 | 30.04 | 30 | 502 | 0.4 | 7.3 | 128 | — |
| 15X-2, 135–150 | 127.85 | 7.06 | 29.69 | 30 | 503 | 0.3 | 6.7 | 82 | 4.76 |
| 15X-5, 130–150 | 132.18 | 7.41 | 28.26 | 30 | 502 | 0.5 | 6.9 | 79 | — |
| 16X-2, 130–150 | 137.50 | 6.95 | 30.97 | 30 | 501 | 1.1 | 6.7 | 90 | 4.62 |
| 16X-4, 130–150 | 140.50 | 7.22 | 32.12 | 30 | 500 | 0.6 | 6.7 | 158 | — |
| 17X-2, 130–150 | 147.20 | 7.29 | 39.69 | 31 | 500 | 0.6 | 7.3 | 187 | 6.52 |
| 17X-5, 120–140 | 151.60 | 7.70 | 42.23 | 30 | 499 | 0.3 | 7.5 | 19 | — |
| 18X-2, 130–150 | 156.90 | 7.34 | 45.88 | 32 | 500 | 0.7 | 7.6 | 135 | 6.25 |
| 18X-4, 130–150 | 159.90 | 7.25 | 38.19 | 30 | 499 | 1.6 | 7.7 | 117 | — |
| 19X-2, 130–150 | 166.60 | 7.25 | 47.66 | 31 | 496 | 0.8 | 8.0 | 164 | — |
| 19X-5, 130–150 | 171.10 | 7.25 | 46.94 | 30 | 493 | 1.1 | 8.4 | 174 | — |
| 20X-2, 130–150 | 176.30 | 7.12 | 47.18 | 30 | 493 | 1.9 | 7.6 | 107 | 7.56 |
| 20X-3, 130–150 | 177.80 | 7.35 | 48.80 | 30 | 493 | 0.0 | 8.7 | 84 | — |
| 21X-2, 130–150 | 185.90 | 7.14 | 49.99 | 30 | 490 | 0.5 | 9.7 | 119 | — |
| 21X-5, 130–150 | 190.36 | 7.12 | 49.69 | 30 | 488 | 1.1 | 9.8 | 108 | — |
| 22X-3, 130–150 | 197.00 | 7.71 | 46.68 | 30 | 489 | 1.4 | 10.3 | 92 | 6.62 |
| 23X-3, 130–150 | 205.78 | 7.30 | 47.24 | 30 | 486 | 1.0 | 10.6 | 88 | — |
| 24X-3, 130–150 | 215.50 | 7.24 | 45.96 | 30 | 481 | 1.7 | 10.4 | 100 | 6.65 |
| 25X-3, 130–150 | 225.20 | 7.02 | 48.21 | 30 | 482 | 1.0 | 11.4 | 86 | — |
| 26X-3, 130–150 | 234.80 | 7.12 | 46.81 | 30 | 482 | 2.0 | 11.3 | 57 | 5.51 |
| 27X-3, 130–150 | 244.50 | 7.24 | 44.45 | 30 | 480 | 0.6 | 11.4 | 46 | — |
| 28X-3, 130–150 | 254.14 | 7.16 | 43.45 | 30 | 479 | 0.1 | 12.0 | 15 | 5.49 |

Notes: DOC = dissolved organic carbon. — = no sample was available.

**Table T4.** Concentrations of methane, ethane, ethylene, propane, and propylene in headspace gas, Hole 1252A.

| Core, section, interval (cm) | Depth (mbsf) | $C_1$ (ppmv) | $C_2$ (ppmv) | $C_{2=}$ (ppmv) | $C_3$ (ppmv) | $C_{3=}$ (ppmv) | $C_1/C_2$ |
|---|---|---|---|---|---|---|---|
| 204-1252A- | | | | | | | |
| 1H-1, 0–5 | 0.00 | 2 | | | | | |
| 1H-1, 130–135 | 1.30 | 7 | | | | | |
| 1H-3, 0–5 | 3.00 | 116 | | | | | |
| 1H-4, 0–5 | 4.00 | 261 | | | | | |
| 2H-2, 0–5 | 6.40 | 10,165 | | | | | |
| 2H-3, 0–5 | 7.90 | 23,550 | | | | | |
| 2H-4, 0–5 | 9.40 | 42,152 | 1.1 | | | | 36,975 |
| 2H-5, 0–5 | 10.90 | 50,479 | 1.6 | | | | 30,780 |
| 2H-5, 0–5 | 10.90 | 36,197 | 1.1 | | | 1.0 | 34,473 |
| 2H-6, 0–5 | 12.40 | 24,932 | 1.1 | | | | 23,085 |
| 2H-7, 0–5 | 13.90 | 14,001 | | | | | 30,000 |
| 3H-3, 0–5 | 16.15 | 48,679 | 1.5 | | | | 32,238 |
| 4H-2, 0–5 | 25.40 | 17,277 | 1.1 | | | | 16,454 |
| 5H-3, 0–5 | 35.49 | 14,353 | 0.9 | | | | 15,433 |
| 6H-3, 0–5 | 45.90 | 18,386 | 1.1 | | | | 17,510 |
| 7H-3, 0–5 | 55.40 | 15,865 | 1.2 | | | | 13,560 |
| 8H-2, 0–5 | 63.40 | 12,149 | 1.2 | | | | 10,124 |
| 9H-3, 0–5 | 74.40 | 15,206 | 2.7 | | 2.8 | | 5,653 |
| 9H-6, 0–5 | 78.90 | 21,190 | 2.7 | | 1.6 | | 7,819 |
| 10H-3, 0–5 | 83.00 | 8,384 | 2.6 | | | | 3,275 |
| 10H-6, 0–5 | 87.50 | 20,198 | 3.7 | | | | 5,401 |
| 11H-3, 0–5 | 93.40 | 12,890 | 4.0 | 0.8 | | 0.8 | 3,223 |
| 11H-6, 0–5 | 97.90 | 19,779 | 6.1 | | | | 3,248 |
| 12H-3, 0–5 | 102.90 | 16,531 | 5.0 | | 0.6 | | 3,326 |
| 12H-6, 0–5 | 107.30 | 19,912 | 7.1 | 0.7 | | | 2,805 |
| 13H-3, 0–5 | 112.40 | 15,506 | 6.1 | | | | 2,530 |
| 14H-3, 0–5 | 121.90 | 12,473 | 6.8 | | | | 1,837 |
| 14H-6, 0–5 | 126.09 | 13,646 | 7.7 | | | | 1,775 |
| 15H-3, 0–5 | 128.00 | 13,221 | 4.1 | | | | 3,209 |
| 15H-6, 0–5 | 132.38 | 12,521 | 6.7 | | | | 1,872 |
| 16H-3, 0–5 | 137.70 | 13291 | 5.3 | | | | 2,489 |
| 16H-4, 0–5 | 139.20 | 11,151 | 7.2 | | 2.7 | | 1,553 |
| 17H-3, 0–5 | 147.40 | 2,041 | 1.3 | | | | 1,607 |
| 17H-6, 0–5 | 151.80 | 11,161 | 8.8 | | | | 1,264 |
| 18H-3, 0–5 | 157.10 | 7,973 | 5.6 | | | | 1,434 |
| 18H-4, 0–5 | 158.60 | 5,311 | 6.0 | 0.7 | | | 888 |
| 19H-3, 0–5 | 166.80 | 7,231 | 5.6 | | 2.4 | 2.1 | 1,294 |
| 19H-6, 0–5 | 171.30 | 6,643 | 8.1 | | | | 816 |
| 20H-3, 0–5 | 176.50 | 4,497 | 4.6 | | 3.3 | 2.8 | 978 |
| 20H-4, 0–5 | 178.00 | 7,264 | 6.7 | | 1.5 | | 1,079 |
| 21H-3, 0–5 | 186.10 | 3,168 | 4.9 | | | | 651 |
| 21H-6, 0–5 | 190.56 | 8,290 | 10.3 | | 2.8 | 1.0 | 802 |
| 22H-4, 0–5 | 197.20 | 7,342 | 8.7 | | | | 842 |
| 23H-4, 0–5 | 205.98 | 5,736 | 8.8 | | | | 650 |
| 24H-4, 0–5 | 215.70 | 3,966 | 7.2 | | | | 549 |
| 25H-4, 0–5 | 225.40 | 12,775 | 25.8 | | 1.0 | | 496 |
| 26X-4, 0–5 | 235.00 | 11,397 | 24.1 | | | | 473 |
| 27X-4, 0–5 | 244.70 | 14,892 | 36.9 | | 1.7 | | 403 |
| 28X-4, 0–5 | 254.34 | 14,095 | 28.5 | | | | 495 |

Note: $C_1$ = methane, $C_2$ = ethane, $C_{2=}$ = ethylene, $C_3$ = propane, $C_{3=}$ = propylene.

**Table T5.** Concentration of light hydrocarbon and nonhydrocarbon gases in VAC samples of core gas voids, Hole 1252A.

| Core, section, interval (cm) | Depth (mbsf) | $C_1$ (ppmv) | $C_2$ (ppmv) | $C_3$ (ppmv) | *i*-$C_4$ (ppmv) | *n*-$C_4$ (ppmv) | $CO_2$ (ppmv) | $O_2$ (ppmv) | $N_2$ (ppmv) | $C_1/C_2$ |
|---|---|---|---|---|---|---|---|---|---|---|
| 204-1252A- | | | | | | | | | | |
| 2H-7, 63 | 14.53 | 19,067 | | | | | | | 819,926 | |
| 3H-2, 98 | 15.63 | 2,028 | | | | | | | 832,425 | |
| 3H-3, 13 | 16.28 | 900,674 | 45.0 | | | | 25,572 | 1,337 | 16,648 | 20,024 |
| 3H-3, 31 | 16.46 | 917,435 | 7.1 | | | | 20,815 | 817 | 6,433 | 128,853 |
| 3H-6, 82 | 21.47 | 912,403 | 7.4 | | | | 27,472 | 984 | 4,600 | 124,136 |
| 4H-1, 121 | 25.11 | 874,133 | 6.0 | | | | 25,292 | 6,384 | 47,945 | 146,421 |
| 4H-2, 25 | 25.65 | 914,670 | 11.3 | | | | 20,670 | 756 | 14,198 | 81,088 |
| 4H-6, 123 | 32.51 | 924,764 | 7.3 | | | | 25,583 | 547 | 1,138 | 127,554 |
| 5H-2, 74 | 34.73 | 648,783 | 9.4 | | | | 29,358 | | | 69,019 |
| 5H-3, 37 | 35.86 | 920,889 | 7.7 | | | | 24,483 | 37,746 | 146,321 | 119,907 |
| 5H-5, 90 | 39.39 | 934,808 | 6.8 | | | | 18,839 | 549 | 1,029 | 138,490 |
| 5H-6, 70 | 40.69 | 9,128 | | | | | 186,282 | 728,168 | | |
| 6H-1, 40 | 43.30 | 2,696 | | | | | | | | |
| 6H-2, 57 | 44.97 | 902,781 | 7.0 | | | | 17,193 | 387 | 46,559 | 129,338 |
| 6H-4, 88 | 48.28 | 921,897 | 10.2 | | | | 11,143 | 224 | 37,168 | 90,205 |
| 6H-7, 13 | 52.03 | 918,156 | 8.2 | | | | 34,438 | 198 | 8,825 | 112,381 |
| 7H-2, 19 | 54.09 | 932,670 | 9.3 | | | | 21,603 | 186 | 10,333 | 99,858 |
| 7H-6, 44 | 60.34 | 933,935 | 9.5 | | | | 21,197 | 158 | 7,693 | 98,206 |
| 8H-1, 98 | 62.88 | 913,106 | 19.5 | 11.8 | | | 19,875 | 260 | 31,980 | 46,874 |
| 8H-3, 123 | 66.13 | 607,083 | 23.2 | | | | 7,011 | 64,746 | 319,301 | 26,190 |
| 9H-2, 64 | 73.54 | 933,852 | 16.1 | | | | 14,084 | 266 | 17,653 | 58,112 |
| 9H-7, 14 | 80.38 | 931,280 | 20.6 | | | | 20,188 | 242 | 8,144 | 45,274 |
| 10H-3, 115 | 84.15 | 966,802 | 41.8 | 12.2 | | | 8,803 | 29,939 | 116,426 | 23,146 |
| 10H-3, 115 | 84.15 | 944,856 | 26.6 | | | | 8,774 | 193 | 8,109 | 35,481 |
| 10H-5, 0 | 86.00 | 945,805 | 23.2 | | | | 7,548 | 173 | 12,593 | 40,785 |
| 10H-7, 34 | 89.34 | 947,965 | 34.9 | | | | 8,760 | 190 | 5,527 | 27,186 |
| 11H-1, 126 | 91.66 | 938,123 | 32.8 | | | | 16,017 | 236 | 11,717 | 28,645 |
| 11H-3, 0 | 93.40 | 945,540 | 32.8 | | | | 10,930 | 184 | 6,932 | 28,792 |
| 11H-7, 0 | 98.85 | 951,298 | 159 | 4.4 | | | 3,937 | 293 | 7,312 | 5,973 |
| 12H-1, 106 | 100.96 | 898,967 | 57.0 | 18.1 | | | 12,099 | 445 | 53,906 | 15,766 |
| 12H-3, 78 | 103.68 | 949,109 | 125 | | | | 4,319 | 257 | 11,687 | 7,580 |
| 12H-6, 116 | 108.46 | 945,806 | 59.9 | | | | 5,007 | 232 | 11,173 | 15,795 |
| 13H-1, 130 | 110.70 | 948,618 | 157 | 18.1 | | | 8,605 | 235 | 6,665 | 6,061 |
| 14H-1, 70 | 119.60 | 949,706 | 74.7 | | | | 7,073 | 210 | 7,506 | 12,719 |
| 14H-3, 60 | 122.50 | 952,980 | 81.5 | | | | 4,367 | 204 | 6,401 | 11,694 |
| 14H-6, 0 | 126.09 | 960,873 | 123 | 9.1 | | | | | | 7,844 |
| 15X-4, 72 | 130.10 | 943,733 | 76.5 | | | | 7,692 | 194 | 6,118 | 12,341 |
| 15X-5, 54 | 131.42 | 946,017 | 80.3 | | | | 6,459 | 182 | 5,157 | 11,777 |
| 16X-2, 0 | 136.20 | 935,023 | 105 | | | | 16,682 | 263 | 8,885 | 8,912 |
| 16X-3, 115 | 138.85 | 550,157 | 63.0 | | | | 5,629 | 79,145 | 363,463 | 8,731 |
| 16X-4, 45 | 139.65 | 948,048 | 95.9 | | | | 6,961 | 282 | 10,477 | 9,888 |
| 17X-2, 0 | 145.90 | 946,698 | 97.7 | 16.7 | | | 8,850 | 197 | 7,365 | 9,692 |
| 17X-4, 16 | 149.06 | 947,754 | 104 | | | | 10,265 | 205 | 6,870 | 9,108 |
| 17X-5, 0 | 150.40 | 947,553 | 101 | | | | 8,449 | 154 | 6,099 | 9,397 |
| 18X-2, 0 | 155.60 | 948,061 | 96.8 | | | | 7,271 | 252 | 10,083 | 9,794 |
| 18X-2, 116 | 156.76 | 953,756 | 95.1 | | | | 4,790 | 241 | 9,032 | 10,033 |
| 18X-4, 0 | 158.60 | 950,008 | 106 | | | | 8,137 | 169 | 5,679 | 8,977 |
| 20X-2, 47 | 175.47 | 938,237 | 120 | 18.2 | | | 5,497 | 449 | 18,551 | 7,806 |
| 20X-4, 53 | 178.53 | 934,677 | 156 | | | | 15,957 | 312 | 11,206 | 6,011 |
| 21X-4, 64 | 188.20 | 921,252 | 260 | 20.8 | | | 28,805 | 351 | 12,275 | 3,547 |
| 22X-4, 0 | 197.20 | 899,890 | 211 | | | | 11,050 | 1,019 | 43,685 | 4,264 |
| 22X-6, 133 | 201.53 | 895,186 | 192 | | | | 6,293 | 1,286 | 55,370 | 4,656 |
| 23X-2, 78 | 203.76 | 798,300 | 214 | | | | 6,225 | 21,201 | 141,088 | 3,726 |
| 23X-3, 130 | 205.78 | 953,276 | 242 | | | | 7,689 | 200 | 6,041 | 3,942 |
| 23X-4, 20 | 206.18 | 849,971 | 296 | | | | 26,539 | 3,444 | 75,598 | 2,870 |
| 24X-3, 114 | 215.34 | 381,182 | 99.7 | | | | 3,590 | 446,933 | | 3,824 |
| 25X-6, 15 | 228.55 | 934,184 | 313 | 18.3 | | | 12,443 | 338 | 13,564 | 2,982 |
| 26X-2, 42 | 232.42 | 932,142 | 357 | | | | 23,561 | 223 | 6,802 | 2,615 |
| 26X-4, 30 | 235.30 | 961,459 | 406 | 10.2 | | | | | | 2,371 |
| 26X-6, 119 | 239.19 | 783,652 | 309 | | | | 25,532 | 19,615 | 134,907 | 2,538 |
| 27X-2, 1 | 241.71 | 944,808 | 333 | | | | 13,451 | 240 | 8,837 | 2,840 |
| 27X-3, 110 | 244.30 | 917,583 | 302 | | | | 8,102 | 767 | 31,883 | 3,038 |
| 27X-5, 25 | 246.42 | 953,196 | 289 | | | | 6,739 | 95 | 1,382 | 3,298 |
| 28X-3, 3 | 252.87 | 903,756 | 420 | 10.5 | | | | | | 2,152 |
| 28X-6, 2 | 257.36 | 949,190 | 286 | | | | 9,490 | 160 | 2,950 | 3,319 |

Note: $C_1$ = methane, $C_2$ = ethane, $C_3$ = propane, *i*-$C_4$ = isobutane, *n*-$C_4$ = normal butane, $CO_2$ = carbon dioxide, $O_2$ = oxygen, $N_2$ = nitrogen.

**Table T6.** Presence of gas hydrate based on infrared images of cores in liner, Site 1252.

| Core, section | $\Delta T$ (°C) | Gas hydrate texture* | Depth interval (mbsf)† Top | Depth interval (mbsf)† Bottom | Anomaly‡ designation | Hydrate sample Top (cm) | Hydrate sample Bottom (cm) | Hydrate sample Depth (mbsf) |
|---|---|---|---|---|---|---|---|---|
| 204-1252A- | | | | | | | | |
| 3H | –0.6 | Disseminated; questionable | 18.50 | 19.00 | IR540 | | | |
| 3H | –0.9 | Disseminated; questionable | 21.40 | 22.50 | IR541 | | | |
| 6H | –0.7 | Disseminated; vein | 43.00 | 43.09 | IR542 | | | |
| 6H | –0.5 | Disseminated | 47.40 | 47.61 | IR543 | | | |
| 6H | –0.5 | Nodular; disseminated | 48.42 | 48.50 | IR544 | | | |
| 7H | –0.8 | Disseminated | 53.70 | 55.35 | IR545 | | | |
| 7H | –0.9 | Disseminated | 55.70 | 56.80 | IR546 | | | |
| 8H | –0.6 | Disseminated | 64.20 | 64.50 | IR547 | | | |
| 8H | –1.7 | Disseminated; around central vein | 66.50 | 67.32 | IR548 | | | |
| 8H | –1.7 | Nodular; disseminated | 70.64 | 70.71 | IR549 | | | |
| 10H | –0.6 | Disseminated | 81.00 | 81.11 | IR550 | | | |
| 10H-2 | –2.7 | Nodular; vein | 83.06 | 83.25 | IR551 | 35 | 45 | 82.75 |
| 10H | –0.3 | Disseminated | 87.47 | 87.56 | IR552 | | | |
| 11H | –0.6 | Disseminated | 97.10 | 96.83 | IR553 | | | |
| 11H-6 | –3.2 | Vein; parallel to bedding | 98.45 | 98.50 | IR554 | 70 | 80 | 98.60 |
| 12H | –0.5 | Disseminated | 100.08 | 100.12 | IR555 | | | |
| 12H | –0.6 | Disseminated | 102.90 | 102.94 | IR556 | | | |
| 12H | –0.9 | Disseminated; vein | 103.43 | 103.64 | IR557 | | | |
| 12H | –0.4 | Disseminated | 103.89 | 103.90 | IR558 | | | |
| 12H | –0.8 | Vein; disseminated; split by gas | 106.80 | 106.86 | IR559 | | | |
| 12H | –0.8 | Nodular | 107.39 | 107.42 | IR560 | | | |
| 12H | –1.8 | Vein; disseminated | 109.48 | 109.65 | IR561 | | | |
| 13H | –0.9 | Vein; slight dip; disseminated | 111.50 | 111.85 | IR562 | | | |
| 13H | –0.6 | Disseminated; variable $\Delta T$ | 117.50 | 118.40 | IR563 | | | |
| 14H | –0.5 | Disseminated; questionable | 118.90 | 119.10 | IR564 | | | |
| 14H | –0.4 | Disseminated; periodic spacing | 119.40 | 119.75 | IR565 | | | |
| 14H | –0.2 | Disseminated | 120.60 | 120.67 | IR566 | | | |
| 14H | –0.3 | Disseminated; periodic spacing | 121.20 | 121.25 | IR567 | | | |
| 14H | –0.5 | Disseminated; cracking | 125.25 | 125.70 | IR568 | | | |
| 15X | –0.7 | Disseminated | 128.55 | 128.62 | IR569 | | | |
| 15X | –0.4 | Disseminated | 131.05 | 131.14 | IR570 | | | |
| 15X | –0.3 | Disseminated | 132.88 | 132.94 | IR571 | | | |
| 21X | –0.9 | Vein; disseminated; cold core top? | 183.15 | 183.22 | IR572 | | | |

Notes: * = from anomaly characteristics and core description, if available. † = from uncut core liner. ‡ = used for reference to specific anomalies in text and figures. The difference between these depth intervals and the equivalent curated section depth intervals is typically <1 m.

**Table T7.** Moisture and density, Hole 1252A.

| Core, section, interval (cm) | Depth (mbsf) | Density (g/cm³) Bulk | Density (g/cm³) Grain | Porosity (%) |
|---|---|---|---|---|
| 204-1252A- | | | | |
| 1H-1, 76–78 | 0.76 | 1.443 | 2.610 | 73.6 |
| 1H-2, 74–76 | 2.24 | 1.515 | 2.726 | 71.2 |
| 1H-3, 74–76 | 3.74 | 1.595 | 2.825 | 68.3 |
| 1H-4, 34–36 | 4.34 | 1.570 | 2.704 | 67.5 |
| 2H-1, 74–76 | 5.64 | 1.590 | 2.767 | 67.5 |
| 2H-3, 74–76 | 8.64 | 1.542 | 2.685 | 68.8 |
| 2H-5, 74–76 | 11.64 | 1.619 | 2.797 | 66.4 |
| 2H-7, 54–56 | 14.44 | 1.596 | 2.708 | 66.0 |
| 3H-2, 74–76 | 15.39 | 1.567 | 2.681 | 67.2 |
| 3H-4, 74–76 | 18.39 | 1.586 | 2.694 | 66.3 |
| 3H-6, 74–76 | 21.39 | 1.621 | 2.783 | 66.1 |
| 4H-2, 82–84 | 26.22 | 1.618 | 2.699 | 64.5 |
| 4H-4, 74–76 | 29.02 | 1.603 | 2.760 | 66.7 |
| 4H-6, 74–76 | 32.02 | 1.583 | 2.692 | 66.5 |
| 5H-2, 74–76 | 34.73 | 1.627 | 2.757 | 65.2 |
| 5H-4, 74–76 | 37.73 | 1.581 | 2.647 | 65.7 |
| 5H-6, 71–73 | 40.70 | 1.610 | 2.727 | 65.6 |
| 6H-1, 74–76 | 43.64 | 1.648 | 2.675 | 62.2 |
| 6H-3, 74–76 | 46.64 | 1.599 | 2.722 | 66.1 |
| 6H-5, 74–76 | 49.64 | 1.627 | 2.694 | 63.9 |
| 7H-1, 70–72 | 53.10 | 1.649 | 2.685 | 62.4 |
| 7H-3, 74–76 | 56.14 | 1.640 | 2.720 | 63.7 |
| 7H-5, 74–76 | 59.14 | 1.675 | 2.742 | 62.1 |
| 8H-1, 74–76 | 62.64 | 1.644 | 2.694 | 62.9 |
| 8H-3, 74–76 | 65.64 | 1.644 | 2.699 | 63.0 |
| 8H-5, 74–76 | 68.64 | 1.634 | 2.612 | 61.6 |
| 9H-1, 84–86 | 72.24 | 1.729 | 2.750 | 59.1 |
| 9H-3, 24–26 | 74.64 | 1.748 | 2.770 | 58.5 |
| 9H-3, 34–36 | 74.74 | 1.677 | 2.665 | 60.2 |
| 9H-5, 74–76 | 78.14 | 1.670 | 2.679 | 61.0 |
| 9H-7, 26–28 | 80.50 | 1.730 | 2.747 | 59.0 |
| 10H-1, 74–76 | 81.64 | 1.678 | 2.692 | 60.8 |
| 10H-4, 74–76 | 85.24 | 1.713 | 2.712 | 59.2 |
| 10H-6, 74–76 | 88.24 | 1.710 | 2.647 | 57.7 |
| 11H-2, 74–76 | 92.64 | 1.727 | 2.674 | 57.4 |
| 11H-4, 96–98 | 95.86 | 1.740 | 2.682 | 56.8 |
| 11H-6, 51–53 | 98.41 | 1.772 | 2.727 | 56.1 |
| 12H-1, 74–76 | 100.64 | 1.746 | 2.702 | 57.0 |
| 12H-3, 74–76 | 103.64 | 1.748 | 2.665 | 55.9 |
| 12H-4, 104–106 | 105.34 | 1.729 | 2.697 | 57.8 |
| 12H-5, 96–98 | 106.76 | 1.759 | 2.672 | 55.4 |
| 12H-6, 112–114 | 108.42 | 1.718 | 2.658 | 57.5 |
| 12H-7, 82–84 | 109.62 | 1.747 | 2.695 | 56.7 |
| 13H-1, 102–104 | 110.42 | 1.752 | 2.662 | 55.5 |
| 13H-2, 74–76 | 111.64 | 1.727 | 2.718 | 58.5 |
| 13H-2, 103–105 | 111.93 | 1.767 | 2.701 | 55.7 |
| 13H-3, 22–24 | 112.62 | 1.746 | 2.703 | 57.0 |
| 13H-3, 104–106 | 113.44 | 1.768 | 2.711 | 55.9 |
| 13H-4, 42–44 | 114.32 | 1.791 | 2.738 | 55.3 |
| 13H-5, 74–76 | 115.51 | 1.935 | 2.808 | 49.0 |
| 13H-6, 50–52 | 116.27 | 1.949 | 2.827 | 48.7 |
| 14H-1, 74–76 | 119.64 | 1.712 | 2.726 | 59.5 |
| 14H-3, 74–76 | 122.64 | 1.637 | 2.616 | 61.5 |
| 14H-5, 74–76 | 125.56 | 1.657 | 2.662 | 61.4 |
| 14H-7, 58–60 | 128.17 | 1.604 | 2.629 | 63.9 |
| 15X-1, 67–69 | 125.67 | 1.647 | 2.623 | 61.0 |
| 15X-3, 85–87 | 128.85 | 1.694 | 2.659 | 59.0 |
| 15X-5, 66–68 | 131.54 | 1.619 | 2.617 | 62.7 |
| 15X-7, 74–76 | 133.93 | 1.714 | 2.693 | 58.6 |
| 16X-1, 81–83 | 135.51 | 1.597 | 2.685 | 65.5 |
| 16X-3, 74–76 | 138.44 | 1.592 | 2.598 | 63.9 |
| 17X-1, 74–76 | 145.14 | 1.637 | 2.704 | 63.5 |
| 17X-3, 74–76 | 148.14 | 1.642 | 2.653 | 62.0 |
| 17X-5, 74–76 | 151.14 | 1.663 | 2.654 | 60.8 |
| 18X-1, 74–76 | 154.84 | 1.696 | 2.683 | 59.5 |
| 18X-3, 50–52 | 157.60 | 1.648 | 2.716 | 63.1 |
| 19X-1, 74–76 | 164.54 | 1.736 | 2.696 | 57.4 |
| 19X-3, 74–76 | 167.54 | 1.754 | 2.676 | 55.8 |
| 19X-5, 74–76 | 170.54 | 1.731 | 2.657 | 56.7 |
| 20X-1, 74–76 | 174.24 | 1.696 | 2.621 | 57.9 |
| 20X-3, 74–76 | 177.24 | 1.752 | 2.681 | 56.1 |
| 21X-1, 25–27 | 183.35 | 1.822 | 2.752 | 53.8 |
| 21X-1, 47–49 | 183.57 | 2.177 | 2.853 | 36.9 |
| 21X-1, 52–54 | 183.62 | 1.878 | 2.807 | 52.1 |
| 21X-1, 64–66 | 183.74 | 1.818 | 2.734 | 53.6 |
| 21X-1, 74–76 | 183.84 | 1.834 | 2.730 | 52.5 |
| 21X-3, 70–72 | 186.80 | 1.642 | 2.650 | 62.0 |
| 21X-5, 74–76 | 189.80 | 1.655 | 2.644 | 61.1 |
| 22X-1, 74–76 | 193.44 | 1.627 | 2.608 | 61.9 |
| 22X-3, 71–73 | 196.41 | 1.641 | 2.591 | 60.6 |
| 22X-5, 74–76 | 199.44 | 1.619 | 2.631 | 63.0 |
| 23X-1, 61–63 | 202.51 | 1.663 | 2.571 | 58.7 |
| 23X-3, 76–78 | 205.24 | 1.684 | 2.672 | 60.0 |
| 23X-5, 113–115 | 208.61 | 1.799 | 2.687 | 53.4 |
| 24X-1, 53–55 | 211.73 | 1.729 | 2.676 | 57.3 |
| 24X-3, 77–79 | 214.97 | 1.713 | 2.728 | 59.5 |
| 24X-5, 48–50 | 217.18 | 1.618 | 2.708 | 64.8 |
| 25X-1, 70–72 | 221.60 | 1.691 | 2.758 | 61.5 |
| 25X-3, 97–99 | 224.87 | 1.667 | 2.735 | 62.4 |
| 25X-5, 101–103 | 227.91 | 1.611 | 2.683 | 64.6 |
| 26X-1, 100–102 | 231.50 | 1.628 | 2.634 | 62.5 |
| 26X-3, 71–73 | 234.21 | 1.611 | 2.727 | 65.5 |
| 26X-5, 78–80 | 237.28 | 1.671 | 2.700 | 61.4 |
| 27X-1, 80–82 | 241.00 | 1.664 | 2.724 | 62.4 |
| 27X-3, 48–50 | 243.68 | 1.646 | 2.704 | 62.9 |
| 27X-5, 111–113 | 247.28 | 1.635 | 2.646 | 62.3 |
| 27X-7, 42–44 | 249.09 | 1.640 | 2.666 | 62.5 |
| 28X-1, 96–98 | 250.96 | 1.631 | 2.670 | 63.1 |
| 28X-3, 77–79 | 253.61 | 1.679 | 2.726 | 61.5 |
| 28X-4, 72–74 | 255.06 | 1.694 | 2.659 | 59.0 |
| 28X-6, 120–122 | 258.54 | 1.731 | 2.683 | 57.4 |

**Table T8.** Thermal conductivity, Hole 1252A.

| Core, section, interval (cm) | Depth (mbsf) | Thermal conductivity (W/[m·K]) | Individual measurements (W/[m·K]) | | |
|---|---|---|---|---|---|
| 204-1252A- | | | | | |
| 1H-2, 80 | 2.30 | 0.905 | 0.918 | 0.911 | 0.887 |
| 4H-1, 65 | 24.55 | 0.874 | 0.886 | 0.866 | 0.870 |
| 4H-3, 75 | 27.65 | 0.818 | 0.817 | 0.809 | 0.829 |
| 4H-5, 75 | 30.53 | 0.840 | 0.828 | 0.839 | 0.854 |
| 5H-3, 45 | 35.94 | 0.781 | 0.820 | 0.744 | 0.780 |
| 6H-1, 76 | 43.66 | 0.885 | 0.915 | 0.872 | 0.867 |
| 6H-3, 34 | 46.24 | 0.812 | 0.827 | 0.801 | 0.809 |
| 6H-5, 77 | 49.67 | 0.871 | 0.867 | 0.869 | 0.878 |
| 7H-3, 57 | 55.97 | 0.831 | 0.843 | 0.816 | 0.835 |
| 8H-1, 83 | 62.73 | 0.871 | 0.864 | 0.874 | 0.875 |
| 8H-3, 48 | 65.38 | 0.904 | 0.913 | 0.899 | 0.899 |
| 8H-5, 54 | 68.44 | 0.846 | 0.839 | 0.843 | 0.857 |
| 9H-3, 75 | 75.15 | 0.932 | 0.916 | 0.939 | 0.942 |
| 10H-1, 45 | 81.35 | 0.970 | 0.951 | 0.977 | 0.982 |
| 10H-3, 31 | 83.31 | 0.867 | 0.867 | 0.866 | 0.867 |
| 10H-5, 65 | 86.65 | 0.960 | 0.953 | 0.967 | 0.959 |
| 11H-3, 66 | 94.06 | 1.034 | 1.036 | 1.021 | 1.045 |
| 12H-1, 63 | 100.53 | 1.095 | 1.087 | 1.114 | 1.083 |
| 12H-3, 68 | 103.58 | 1.100 | 1.123 | 1.100 | 1.078 |
| 12H-5, 70 | 106.50 | 1.073 | 1.064 | 1.095 | 1.061 |
| 13H-3, 68 | 113.08 | 0.905 | 0.918 | 0.899 | 0.899 |
| 14H-1, 75 | 119.65 | 0.940 | 0.956 | 0.930 | 0.934 |
| 14H-3, 68 | 122.58 | 0.912 | 0.916 | 0.922 | 0.899 |
| 14H-6, 40 | 126.49 | 0.899 | 0.909 | 0.896 | 0.892 |
| 15X-3, 55 | 128.55 | 0.933 | 0.922 | 0.934 | 0.942 |
| 16X-3, 75 | 138.45 | 0.900 | 0.915 | 0.886 | 0.900 |
| 17X-3, 75 | 148.15 | 0.953 | 0.954 | 0.956 | 0.948 |
| 18X-3, 62 | 157.72 | 0.938 | 0.94 | 0.937 | 0.938 |
| 19X-3, 76 | 167.56 | 0.965 | 0.938 | 0.976 | 0.980 |
| 20X-3, 59 | 177.09 | 1.033 | 1.016 | 1.047 | 1.037 |
| 21X-3, 67 | 186.77 | 0.960 | 0.973 | 0.953 | 0.954 |
| 22X-3, 75 | 196.45 | 0.963 | 0.952 | 0.965 | 0.973 |
| 23X-3, 59 | 205.07 | 0.931 | 0.931 | 0.937 | 0.924 |
| 24X-3, 71 | 214.91 | 0.931 | 0.935 | 0.928 | 0.930 |
| 25X-3, 75 | 224.65 | 0.900 | 0.901 | 0.897 | 0.902 |
| 26X-3, 70 | 234.20 | 0.918 | 0.917 | 0.914 | 0.923 |
| 27X-3, 82 | 244.02 | 0.836 | 0.838 | 0.843 | 0.828 |
| 28X-3, 82 | 253.66 | 0.904 | 0.908 | 0.898 | 0.906 |

**Table T9.** Temperature measurements, Hole 1252A.

| Core | Depth (mbsf) | Temperature (°C) | Thermal conductivity (W/[m·K]) | Tool ID |
|---|---|---|---|---|
| 204-1252A- | | | | |
| 1H | 00.0 | 3.85 | — | APCT 11 |
| 4H | 33.4 | 5.35 | 0.84 | APCT 11 |
| 6H | 52.4 | 6.41 | 0.87 | APCT 11 |
| 8H | 71.4 | 7.59 | 0.85 | APCT 11 |
| 10H | 90.4 | 8.66 | 0.96 | APCT 11 |
| 12H | 109.4 | 9.61 | 1.08 | APCT 11 |
| 14H | 125.0 | 11.46 | 0.90 | APCT 11 |

Notes: ID = identification. APCT = advanced piston corer temperature tool. No DVTPP measurements were made at this site.

**Table T10.** Conventional wireline logging operations summary, Hole 1252A.

| Date (Aug 2002) | Local time (hr) | Tool depth (mbsf) | Remarks |
|---|---|---|---|
| 31 | 0140 | | Last core on deck |
| 31 | 0145–0215 | | Circulated hole bottoms up with 50 bbl of a sepiolite mud |
| 31 | 0215–0230 | | Hole displaced with sepiolite mud |
| 31 | 0230–0350 | | Set back top drive; bottom of pipe put at 90 mbsf |
| 31 | 0350 | | Start logging rig-up |
| 31 | 0600 | | Start going down with triple combination (TAP/DIT/HLDT/APS/HNGS) tool string |
| 31 | 0640 | 0 | Stop 5 min at mudline for temperature calibration |
| 31 | 0700 | 262 | Tool at TD; start logging-up pass at 900 ft/hr |
| 31 | 0745 | 75 | Tool back into pipe; speed up to 1500 ft/hr to log mudline |
| 31 | 0755 | 0 | End of pass 1 |
| 31 | 0805 | 184 | Tool at TD; start logging-up pass 2 at 900 ft/hr |
| 31 | 0835 | 75 | Tool back in pipe; end of pass 2 |
| 31 | 0915 | | Tool back on rig floor |
| 31 | 1010 | | Finish rig-down |
| 31 | 1045 | | Start logging rig-up |
| 31 | 1210 | | Start going down with FMS-sonic (FMS/DSI/SGT) tool |
| 31 | 1310 | 262 | Tool at TD; start logging-up pass at 900 ft/hr |
| 31 | 1345 | 75 | Tool back into pipe; end of pass 1 |
| 31 | 1400 | 262 | Tool at TD; start logging-up pass 2 at 900 ft/hr |
| 31 | 1445 | 75 | Tool back in pipe; end of pass 2 |
| 31 | 1530 | | Tool back on rig floor |
| 31 | 1630 | | Finish rig-down |

Notes: TD = total depth. See Table **T8,** p. 102, in the "Explanatory Notes" chapter for definitions of acronyms.